Distribution Agreement

In presenting this thesis or dissertation as a partial fulfillment of the requirements for an advanced degree from Emory University, I hereby grant to Emory University and its agents the non-exclusive license to archive, make accessible, and display my thesis or dissertation in whole or in part in all forms of media, now or hereafter known, including display on the world wide web. I understand that I may select some access restrictions as part of the online submission of this thesis or dissertation. I retain all ownership rights to the copyright of the thesis or dissertation. I also retain the right to use in future works (such as articles or books) all or part of this thesis or dissertation.

Signature:

_____   _____

Troy von Beck   Date

Discovery of SARS-CoV-2 Antivirals from Zoonotic Peptides and Repurposed Drugs

By

Troy von Beck
Doctor of Philosophy

Graduate Division of Biological and Biomedical Science
Immunology and Molecular Pathogenesis

_____
Joshy Jacob, PhD
Advisor

_____
Arash Grakoui, PhD
Committee Member

_____
Eliver E. B. Ghosn, PhD
Committee Member

_____
F. Eun-Hyung Lee, PhD
Committee Member

_____
Jeremy M. Boss, PhD
Committee Member

Accepted:

_____
Kimberly Jacob Arriola, Ph.D, MPH
Dean of the James T. Laney School of Graduate Studies Date

_____
Date

Discovery of SARS-CoV-2 Antivirals from Zoonotic Peptides and Repurposed Drugs

By

Troy von Beck
B.S., Georgia Institute of Technology, 2016

Advisor: Joshy Jacob, PhD

An abstract of
A dissertation submitted to the Faculty of the
James T. Laney School of Graduate Studies of Emory University
in partial fulfillment of the requirements for the degree of
Doctor of Philosophy
in Graduate Division of Biological and Biomedical Science
Immunology and Molecular Pathogenesis
2023

Abstract

Discovery of SARS-CoV-2 Antivirals from Zoonotic Peptides and Repurposed Drugs

By Troy Alexander von Beck

SARS-CoV-2, the causative viral agent behind the COVID-19 pandemic and a disease whose notoriety is on par with the black plague and the Spanish flu, has driven unprecedented research and discovery from the medical and scientific fields. Since its emergence in late 2019, global efforts to identify novel antivirals and vaccines for this devastating disease have yielded innovative solutions in the development of mRNA vaccines, coronavirus protease inhibitors, and broad-spectrum inhibitors of RNA-dependent RNA polymerases. These medical advances not only exist to limit the morbidity and mortality of SARS-CoV-2 but exist as safeguards against the future zoonotic spillover of other coronavirus and closely related arterivirus species. Development of successful and lasting SARS-CoV-2 antivirals is critically dependent on the targeting of highly conserved viral structures. This definition inherently excludes the spike protein which readily evolves with each new variant, instead shifting the focus towards other viral determinants necessary for viral replication and constrained by interactions with invariant nucleic acid, protein, and lipid substrates.

Here, we employ in silico, in vitro, and in vivo techniques to explore and characterize latent anti-SARS-CoV-2 activity in zoonotic cathelicidins and existing therapeutics which can serendipitously inhibit the viral endoribonuclease encoded by nsp15. In our first experimental aims, we identified a boar cathelicidin derivative termed "Yongshi," which exhibits consistent, albeit modest, inhibition of SARS-CoV-2 and its many variants of concern in cell culture. Through careful time of addition and protein dynamics studies, we posit a theoretical inhibitory mechanism requiring direct interaction between Yongshi and SARS-CoV-2 and potentially involving specific interactions with the conserved heptad repeat domains. In our second set of studies, we employ newly developed in silico screening techniques to first identify human-approved drugs with probable binding to the SARS-CoV-2 nsp15 protein, and then validate them via enzymatic assays with recombinant nsp15. This yielded two previously unknown inhibitors of nsp15, pibrentasvir and atovaquone which were active against both SARS-CoV-2 and the related HCoV-OC43 virus. These findings expand our understanding of cathelicidins in antiviral immunity and identify the first SARS-CoV-2 nsp15 inhibitor active at human bioavailable concentrations in cell culture.

Discovery of SARS-CoV-2 Antivirals from Zoonotic Peptides and Repurposed Drugs

By

Troy von Beck
B.S., Georgia Institute of Technology, 2016

Advisor: Joshy Jacob, PhD

A dissertation submitted to the Faculty of the
James T. Laney School of Graduate Studies of Emory University
in partial fulfillment of the requirements for the degree of
Doctor of Philosophy
in Graduate Division of Biological and Biomedical Science
Immunology and Molecular Pathogenesis
2023

Table of Contents

Chapter 1: Introduction

Origins of the COVID-19 Pandemic

First appearance and description of SARS-CoV-2

The first cases of SARS-CoV-2 were documented in early December of 2019 in the Chinese city of

Wuhan, where reports of an unknown illness causing severe pneumonia first called the attention of

public health experts. The clustering of patients and spread between close contacts was suggestive of an

infectious disease, and the inability of antibiotics to quell the disease was suggestive of a viral agent.

Patient symptoms included fever, muscle aches, headache, and most notably, a dry cough that could

worsen to a state of pneumonia or acute respiratory distress syndrome (ARDS), eventually leading to

death. The disease presentation and appearance in individuals associated with a live animal "wet"

market were unnervingly similar to the original reports for SARS-CoV-1[1].

Indeed, in early-January of 2020 the first genomic sequences of SARS-CoV-2 (denoted at the

time as 2019-nCoV) were produced by the Wuhan Institute of Virology (WIV) from a set of 7 patient

isolates collected at the beginning of the outbreak. The full-length genome was 29,891 base pairs in

length and bore a 79.6% sequence identity to the original SARS-CoV-1 virus and a 96.2% sequence

identity to a known bat coronavirus (BatCoV RaTG13)[1]. It is unclear if SARS-CoV-2 directly jumped from

bats to humans or passed through an intermediate host, but the current consensus is that SARS-CoV-2 is

derived from multiple recombination events between related coronaviruses, making it unlikely we will

ever identify a singular zoonotic ancestor[2]. In addition to the genomic sequence, the WIV also captured

the first electron microscopy images of SARS-CoV-2 showing the typical "crown" like appearance of the

virus and determined a means to propagate the virus in Vero E6 and Huh-7 cell lines. This means of

propagation was then used to determine that SARS-CoV-2 used the same entry receptor as SARS-CoV-1, angiotensin converting enzyme II (ACE2), and that SARS-CoV-2 could be neutralized both by SARS-CoV-2 serum and cross-reactive SARS-CoV-1 serum[1].

Pandemic spread and public health measures

Coinciding with the publication of SARS-CoV-2 as a novel coronavirus on January 23rd, 2019, the ruling government of China enacted lockdowns in Wuhan as well as 15 other cities in the Huibei province in an attempt to restrict viral spread[3]. By this point in time, the epidemic still *appeared* containable, with 2,761 confirmed cases of the novel coronavirus within China and a handful of confirmed cases in Thailand, Japan, the Republic of Korea, and the United States of America[1,4]. However, the public health authorities at the time were unaware of the insidious nature of SARS-CoV-2 relating to its inordinately long incubation period and proclivity for asymptomatic transmission. Within a week it would be apparent the virus was spreading rapidly under the radar, as the first U.S. domestic cases of SARS-CoV-2 were identified in individuals without recent travel. By mid-March of 2020, the virus had been confirmed in over 100,000 cases in 114 countries and was officially labeled a pandemic by the World Health Organization (WHO)[4].

In the following year, governments and public health organizations around the world would devise and enact a number of public health measures to help limit the spread of SARS-CoV-2. These would include lockdowns, contact tracing, mandatory quarantine periods, mask mandates, social-distancing, asymptomatic testing, and the closure of schools and workplaces. The implementation of these practices varied greatly across jurisdictions, and was often met with resistance, but they were largely effective in reducing viral transmission[5]. At this point the goal of public health measures had shifted away from containing the outbreak and towards preventing local healthcare providers from

being overwhelmed by the surge in cases. These measures also bought precious time for medical

scientists to devise better testing, standards of care, and new medicines for patients.

The development and deployment of SARS-CoV-2 therapeutics and vaccines

In the early phases of the pandemic, improvements in COVID-19 treatment relied on factors

shown to be effective in previous coronavirus outbreaks and on the management of the severe

inflammation driven by SARS-CoV-2. Among the first therapies to be employed was the use of

convalescent plasma from COVID-19 recovered individuals to bolster the immunity of severely diseased

patients. However, convalescent plasma is not only difficult to source and produce, particularly as SARS-

CoV-2 titers wane overtime, but its effectiveness in preventing disease progression is modest at best[6,7].

An improvement to this line of therapy arrived in the form of monoclonal antibodies targeting

neutralizing epitopes on the viral spike protein. These antibodies may lack the breadth of a polyclonal

response provided by convalescent plasma but can be administered at a higher titer without the

problem of donor-to-donor variance. The list of anti-SARS-CoV-2 monoclonal antibodies developed and

approved for use in the U.S. included 8 entries: sotrovimab, casirivimab and imdevimab (REGEN-COV),

bebtelovimab, bamlanivimab and etesevimab (Co-administered), and tixagevimab and cilgavimab

(Evusheld). Outside of the U.S., 4 additional monoclonals: regdanvimab, amubarvimab, romlusevimab,

and DXP-604 were used clinically. As expected, viral evolution and escape from neutralizing antibody

responses eventually eroded the protection offered by all of the aforementioned antibodies, leading to

discontinuation of their use within the United States[8,9].

Beyond antibody-based therapeutics, a number of small molecule antiviral drugs were

investigated and developed for use against SARS-CoV-2. In the immediate early phase of the pandemic,

these included many drugs known to have broad antiviral activities such as hydroxychloroquine,

chloroquine, and azithromycin as well as drugs with demonstrated efficacy against earlier coronaviruses such as remdesivir and lopinavir/ritonavir[10-12]. Of these early interventions, most would be found wanting for actual clinical efficacy, except remdesivir, which is able to drive premature termination of RNA transcription in SARS-CoV-2[13]. This translated to reduced disease progression and hospitalization in both mild and severe cases of COVID-19[14,15]. 2 years after the emergence of SARS-CoV-2, the first novel inhibitors of SARS-CoV-2 would receive FDA approval to treat COVID-19. These included PAXLOVID (ritonavir boosted nirmatrelvir), an inhibitor of the SARS-CoV-2 3CL protease, and molnupiravir, a ribonucleoside analog that becomes incorporated in viral RNA by the virus encoded polymerase and results in a catastrophic number of mutations to the viral genome[16,17].

Alongside antiviral treatments, the patient standard of care would also improve with the identification of immune modulators better able to limit organ damage from the intense inflammation and cytokine storm observed in severe SARS-CoV-2 infection. Here the first line of defense is dexamethasone, a broadly acting corticosteroid that suppresses vasodilation, leukocyte chemotaxis, and cytokine production[18,19]. Patients whose respiratory function continues to deteriorate may also receive either of the Janus kinase (JAK) inhibitors baricitinib or tofacitinib which block the phosphorylation of STAT transcription factors downstream of cytokine receptors and thereby prevent additional inflammatory gene transcription[20-23]. Some patients may also receive IL-6 receptor blocking monoclonal antibodies sarilumab or tociluzumab to combat the high levels of IL-6 production, however the beneficial effect of this therapy is modest at best[24-27]. Lastly, COVID-19 is characterized by hypercoagulability and thrombotic events driven by the inflammatory response and endothelial damage. This is commonly treated via the administration of low molecular weight heparin, however the results from several clinical trials suggest the benefit of prophylactic heparin in COVID-19 is modest and decreases with increasing severity of disease[28,29].

Despite the many improvements in supportive care for COVID-19 patients, it is without a doubt that the most valuable asset against SARS-CoV-2 has been the development of SARS-CoV-2 vaccines and public health initiatives to achieve herd immunity. Within the U.S., 4 vaccines against SARS-CoV-2 received approval based on 3 separate vaccine platforms. The first two and arguably most successful candidates, Pfizer-Biontech's BNT162b2 (Cominarty) and Moderna's mRNA-1273 (Spikevax) completed their phase III clinical trials in late 2020, just under a year from the start of the SARS-CoV-2 pandemic.

Viral evolution and appearance of major variants of concern

Following the emergence of SARS-CoV-2, random mutagenesis and purifying selection during human-to-human spread gradually began to evolve highly transmissible strains of the ancestral virus. The first variation of significance was simple substitution in the spike gene, D614G, which stabilized the pre-fusion form, preventing early release of the S1 subunit[30]. The appearance of this mutation soon after emergence marked a period of relative quiescence which lasted until the explosion of the alpha, beta, and gamma variants in the Fall of 2020. These variants featured large numbers of mutations and surprised the global community with their high level of divergence from known viral isolates. The sudden appearance of highly mutated variants lacking a clear evolutionary relationship to the ancestral strain remains a matter of scientific discussion. Several theories suggest the viruses either evolved in chronically infected individuals, from spillover events into wildlife and subsequent spillback into humans, or merely from sustained circulation in poorly surveilled populations[31]. Regardless of the evolutionary background, each variant presented significant gains in transmissibility due to common mutations such as N501Y and Δ69/70[32,33]. These were further supplemented by additional mutations such as E484K, which reduced the efficacy of some neutralizing antibodies, and likely reflect adaptation to an increasingly convalescent population[34]. The alpha, beta, and gamma variants rose to dominance for several months before being replaced by the more transmissible delta variant in 2021.

Until this point, the waxing and waning of each variant occurred in the setting of global social distancing campaigns and relative low abundance of immune hosts. However, the implementation of vaccination programs combined with the significant number of convalescent patients began to reach the predicted levels of heard immunity for developed countries in 2021. This posed a significant transmission bottleneck for all existing variants of SARS-CoV-2, and cases declined globally in Fall of 2021. This marked a drastic change in the evolution of SARS-CoV-2, where selection for immune escape variants would be a dominating factor. Indeed, the appearance of the omicron variant BA.1 in late 2021 proved this true, as the new variant possessed an unprecedented capacity for breakthrough infections and ever-increasing transmissibility refined by the sub-lineage variants[35-38]. The continued appearance of new variants and breakthrough infections in a highly vaccinated global population suggests that SARS-CoV-2 has entered a period of permanent endemicity and will continue to evolve and be a nuisance to human health for the foreseeable future.

Lifecycle of SARS-CoV-2 in the host

The lifecycle of SARS-CoV-2 is comprised of highly coordinated events which permit the stepwise processes of cellular entry, genome replication, organelle remodeling, immune suppression, and finally viral egress (See overview in Figure 1). In the following sections we examine the pivotal roles of each virally encoded non-structural protein (nsp), structural protein, and ORF protein in the context of these processes.

Cellular Entry
Entry of SARS-CoV-2 into host cells is classically mediated by interaction with its receptor, angiotensin-converting enzyme 2 (ACE2), and follows class I viral fusion protein mechanism[1]. Like HIV, influenza, and countless other viruses, the spike protein of SARS-CoV-2 is composed of a homotrimer

which undergoes a conformational change upon recognition of its cognate receptor to induce fusion of host the host cell and viral membrane[39].

Structurally, the SARS-CoV-2 spike protein can be divided into two subunits, S1 and S2, separated by a furin cleavage site. Furin cleavage occurs during the maturation of viral progeny in infected host cells, meaning that the S1 and S2 trimers are not covalently linked on mature virions[40]. Each subunit is further divided up into several domains and functional regions. On S1, these regions include the N-terminal domain (NTD), the receptor binding domain (RBD), and two C-terminal domains (CTD1 and CTD2). On S2, these regions include the S2' cleavage site, the fusion peptide (FP), heptad repeats 1 and 2 (HR1 and HR2) separated by the central helix, and finally the transmembrane domain and cytoplasmic tail[41].

Functionally the S1 subunit is responsible for recognition of the ACE2 receptor which induces conformational changes to expose the fusion machinery in S2. Recognition of ACE2 is principally determined by the receptor binding domain, which contains the receptor binding motif (RBM) that makes all direct contacts with the ACE2 receptor[42]. This results in the RBD being both highly conserved, and the most significant target of neutralizing antibodies elicited by either vaccination or natural infection[43]. Notably, the RBM is not always in an accessible state as the individual monomers of the S1 homotrimer fluctuate between a receptor-accessible 'up' conformation and a receptor-inaccessible 'down' conformation. Stability of the S1 subunit seems to favor a 1 'up' and 2 'down' conformation[44]. Compared to the RBD, the function of the NTD is less apparent and seems to involve binding to host sugar-moieties to further increase virion binding to cellular membranes. This appears particularly significant as mutations selected for in new SARS-CoV-2 variants modify the sugar-binding pockets and correlate with increased transmissibility of the new VOCs[45]. The CTD1 and CTD2 regions form several β-structures which support the NTD and RBD domains while also maintaining non-covalent associations

with the S2 subunit. Mutations accrued within the CTDs modulate both the stability of the S trimer as a whole and the transition of spike between the 'up' and 'down' conformations[41].

The S2 subunit contains all the structures necessary to complete fusion once the viral and host membranes are brought into proximity by the S1/ACE2 interaction. This includes an N-terminal serine cleavage site termed S2' that can be cleaved either by membrane bound TMPRSS2 for cell surface entry or by Cathepsin B/L during endosomal entry[46]. In either case, cleavage at this site exposes the fusion peptide, a highly hydrophobic region that can directly insert into the host membrane. The HR1 and HR2 domains function as molecular "ratchet," inducing a conformational change that draws together the viral and host membranes[47].

Cellular entry is therefore a multistep process that begins with low affinity interactions between the NTD and sugar-moieties on the host cell. This loosely attaches virions to host cells and permits time for the stronger RBD/ACE2 bond to form. This bond induces conformational changes in the S1 subunit which exposes the S2' cleavage site. Here the S2' site is cleaved by TMPRSS2, resulting in additional conformational changes that drive insertion of the fusion peptide into the host membrane. In the absence of TMPRSS2, cross-linking of multiple ACE2 receptors by viral spike protein can induce clathrin-mediated endocytosis, leading to viral internalization[48]. In this alternate path, Cathepsin L acts to cleave the S2' site, triggering fusion peptide insertion into the endosomal membrane. Successful entry depends on the insertion of multiple fusion peptides into the cellular membrane, whereby the concerted conformational changes driven by HR1 and HR2 helical bundles force together both membranes until fusion occurs[49]. This action releases the viral RNA into the cytoplasm, completing the infection process.

Replication

Once inside the host cell, the full-length genomic RNA of SARS-CoV-2 is transcribed by host ribosomes to generate two large polyproteins pp1a and pp1ab from the partially overlapping, open reading frames 1 and 1b (ORF1a and ORF1b). Translation of these proteins initiates a cascade of events to form the viral replication and transcription complex (RTC).

The two ORFs encode 16 non-structural proteins (nsp1-16), where pp1a encodes nsp1-11 and pp1ab also encodes nsp1-10 as well as 12-16 due to a -1 frameshift at a programmed frame shift element (PFSE) near the ORF1a terminus[50,51]. Each non-structural protein is separated by a cleavage site for either the virally encoded papain-like protease (PL[pro]) encoded by nsp3 or the chymotrypsin-like protease encoded by nsp5. Nsp5 is often referred to by either the name 3CL[pro], referencing its similarity to picornavirus 3C protease, or M[pro], denoting its significance as the main protease responsible for processing most of the polyprotein cleavage sites. Specifically, PL[pro] is responsible for cleaving after nsp1, nsp2, and nsp3, whereas M[pro] cleaves at all remaining sites to release nsp4-16[52,53].

Due to the size of the coronavirus genome, there is a pressing need to shield double-stranded RNA replication intermediates from host dsRNA sensors. This is achieved by sequestering viral RNA within double-membraned vesicles (DMVs). Experiments in both MERS-CoV and SARS-CoV-1 have demonstrated nsp3 and nsp4 to drive DMV formation[54]. The formation of DMVs is additionally supported by homodimeric nsp6, which remodels the ER to form physical connectors to the DMVs[55]. Inside the DMV, synthesis of genomic and sub-genomic viral RNAs is executed by the RNA-dependent RNA polymerase (RdRp) encoded by nsp12 with its two cofactors nsp7 and nsp8[56]. While nsp12 possesses minimal RNA-synthesizing activity in isolation, it is the association with both nsp7 and nsp8 that permits efficient replication of RNA genome *in vivo*[57]. In addition to acting as a cofactor, nsp8 is also independently responsible for the addition of 3' poly(A) tracts via polyadenylyltransferase and primase activity[58]. Nsp7 and nsp8 are also hypothesized to act as a hexadecameric primase complex that then

transitions to the nsp12-7-8 polymerase complex, however this primase activity is only observed in some experimental systems and may not exist *in vivo*[59]. Further, nsp14 in complex with its cofactor nsp10 can associate with the nsp12-7-8 triad to add proofreading capability via 3'-5' exoribonuclease activity[57]. Following RNA synthesis, nsp13 uses its helicase activity to unzip the dsRNA to provide new single-stranded RNA templates[60].

To enable efficient transcription and evade innate immune sensors, the RdRp synthesized transcripts must receive a 5' cap. This cap is formed via several enzyme catalyzed reactions, beginning with removal of the 5'-triphoshate by nsp13[61]. The second step then sees nsp12 add a single GTP nucleotide to the 5' terminus via 5' to 5' triphosphate linkage[62]. The capping process is continued by the nsp14/nsp10 complex, which acts as an N7-guanine methyltransferase[57,63]. The formation of the 5' cap is completed by the methylation of the first ribonucleotide in the RNA by the nsp16/nsp10 complex acting as a 2'O methyltransferase[64].

These non-structural proteins therefore form the core components of the SARS-CoV-2 replisome but are further supported by nsp9 and nsp15. Although the exact function of nsp9 remains unknown, current evidence suggests it may aid in replication via binding to single-stranded RNA[65]. Nsp15 by comparison has no role in the production of new viral RNA, but functions as an endonuclease with the ability to digest viral RNA and regulate the production of specific RNA species[66].

It should be noted that all the above proteins are translated directly from the positive sense, full-length SARS-CoV-2 genomic RNA via ORF1a and ORF1ab. However, there are additional ORFs occurring after the end of ORF1b that are only accessible via the discontinuous transcription of sub-genomic mRNAs. The production of sub-genomic mRNAs is determined by the presence of transcription regulatory sequences (TRS) located just after the 5' leader sequence and just before each ORF (excluding ORF1a). During synthesis of the negative strand, the RTC may stall at any TRS and then re-initiate at the

leader sequence TRS to synthesize sub-genomic mRNAs bearing the same leader sequence as the full-length RNA[67]. Transcription of the positive strand from the negative sense sub-genomic RNAs thereby produces mRNAs encoding the remaining ORFs. These ORFs generally encode structural proteins and accessory proteins unrelated to replication of the viral genome and whose function is described in greater detail in the following sections.

Evasion of immune defenses

As viruses have been a threat to host survival long before the appearance of the first vertebrates, it is no surprise that humans and other species have evolved a number of defense mechanisms to restrict viral propagation in the event of cellular infection. Engagement of these defenses largely relies on the detection of pathogen associated molecular patterns (PAMPs) to initiate an antiviral state in infected cells. In the case of SARS-CoV-2, this is largely dependent on the activation of the cytoplasmic dsRNA sensors oligoadenylate synthase (OAS), protein kinase R (PKR), and the RIG-I like receptors (RLRs) known as RIG-I and MDA5, as well as the surface or endosomal membrane bound Toll-like receptors (TLRs) 3, 7, and 8. Activation of these signaling pathways also induces the production of interferons (IFNs), cytokines, and chemokines which can make neighboring cells resistant to infection and recruit other immune cells to the site of infection. Therefore, productive infection of a host cell requires not only successful receptor mediated entry, but also evasion of the innate immune system.

Principally, the major PAMP of SARS-CoV-2 is its double-stranded RNA (dsRNA) replication intermediates and immature single-stranded RNA (ssRNA) transcripts. Already we have discussed several aspects of SARS-CoV-2 immune evasion in the previous section. This includes the formation of DMVs by nsp3, nsp4, and nsp6 to physically isolate dsRNA replication intermediates from host cytoplasmic sensors as well as the capping of ssRNA transcripts by nsp10, nsp12, nsp14, and nsp16 to

prevent the detection of uncapped 5' triphosphate ssRNA by RIG-I. The coating of cytoplasmic RNA by N

protein also sterically prevents recognition by host sensors. Further, the ribonuclease activity of nsp15

also functions to limit the accumulation of viral dsRNA, particularly "free" dsRNA that has escaped from

the DMVs[68]. As the discovery of nsp15 inhibitors is a major focus of this dissertation, an exhaustive

review of nsp15 form and function is presented later in this chapter.

In addition to the processes used to sequester and disguise viral RNA, SARS-CoV-2 also employs

multiple antagonists of the host cellular machinery and immune signaling pathways. Many of the viral

structural and non-structural proteins involved in replication are reported to have secondary activities

related to immune function, however this is perhaps better attributed to a "global" disruption of cellular

function that happens to include altered innate immunity. Therefore, the discussion here will focus on

proteins whose primary purpose is the disruption of the host cell function. Perhaps the most significant

factor in this category is nsp1, which has the express purpose of halting the translation of host mRNA.

Nsp1 achieves this via binding to the mRNA groove of the ribosomal 40S subunit, thus preventing

translation initiation. At first it would appear this type of global translation suppression would also

inhibit the virus, but elements contained within the 5' leader sequence of SARS-CoV-2 appear to permit

the translation of viral mRNAs[69]. One analysis suggests that an interaction between the first stem-loop

structure of the 5'UTR and nsp1 bound to the 40S subunit allows the formation of a functional ribosome

complex without nsp1 ever disassociating from the complex[70]. Similarly, nsp2 is able to suppress host

mRNA translation by co-opting the GIGYF2/4EHP pathway to inhibit *ifnb1* mRNA translation[71]. In

addition to the ribosomal antagonism by nsp1 and nsp2, ORF6 is known to bind the IFN-inducible

nucleoporins Nup98 and Rae1, thereby inhibiting the nuclear translocation of transcription factors such

as IRF3 and the nuclear export of mRNAs encoding antiviral ISGs[72,73].

Several of the viral accessory proteins possess a more targeted means to impair the early innate immune signaling pathways. Compared to its longer counterpart in SARS-CoV, the ORF3b in SARS-CoV-2 has acquired multiple premature stop codons which limit it to a small 22 amino acid protein. Despite this, the ORF3b protein appears to retain some IFN-I inhibiting activity, which is dependent upon localization to the cytosol[74]. Similarly, the ORF3c protein also inhibits IFN-β induction via localization to mitochondria and promoting cleavage of the MAVS signaling protein downstream of RIG-I and MDA5[75].

In addition to effects on innate immunity, SARS-CoV-2 can modulate the presentation of antigen to cytotoxic T cells via ORF8. This protein is not membrane bound like its ORF8a counterpart in SARS-CoV-1, but instead is found in the lumen of the ERGIC and secreted into cell medium or the tissue fluids of patients. Immunoprecipitation analysis determined that ORF8 forms direct interactions with both MHC-I and Beclin-1, an autophagosome initiator. This results in the lysosomal degradation of MHC-I, thereby preventing the recognition of SARS-CoV-2 infected cells by cognate cytotoxic T cells[76].

Shedding of progeny

The key factor governing the production of viral progeny is the transcription of the positive sense sub-genomic mRNAs encoding the structural proteins of SARS-CoV-2. These of course include the spike (S), envelope (E), membrane (M), and nucleocapsid (N) proteins which govern the packaging and assembly of newly synthesized genomic RNA into progeny virions.

Following viral infection, N protein is the first of structural components to be expressed, appearing within 5 hours of infection, and followed shortly thereafter by S, E, and M[77]. N protein strongly colocalizes with the endoplasmic reticulum, particularly with DMVs containing viral replication complexes[77]. N combines with newly synthesized positive sense viral genomic RNA to form the

ribonucleoprotein (RNP) complex otherwise known as the capsid. This complex is helical in nature and tightly associated with the interior face of virions in connection with the M protein[78,79].

M protein functions as the major driver of new virion formation. By concentration it is the largest constituent of the SARS-CoV-2 virion and the only necessary factor required for virus-like particle formation[80]. The addition of N, S, or E proteins further augments the formation of VLPs[80,81]. In the ERGIC membrane, M protein self-associates to form dimeric complexes. These complexes have been observed in two conformations, a long and a short form dictated by movement about the hinge region. This movement results in an expansion of the intravirion side and shrinkage of the extravirion side of the M protein dimer in the short form and vice-a-versa in the long form[82]. These two forms are noted to have distinct impacts on the viral envelope, with the long isoform associated with spike protein clustering, membrane rigidity, and a narrow curvature of the membrane[83]. The ability to dynamically shift between the two isoforms likely contributes to invagination of the ERGIC membrane, the budding of virions, and determination of the stoichiometry of the S, M, and N proteins in each virion.

In coronaviruses, the E protein assembles into homopentameric structures in the ER-Golgi intermediate compartment (ERGIC) and thus forms transmembrane cationic ion channels[84]. Surprisingly, experiments conducted with an infections cDNA clone of SARS-CoV-1 revealed that E protein is not an obligate requirement for SARS-CoV-1 replication either in cell culture or a Golden Syrian hamster infection model, but that viral titers are reduced greater than 100-fold[85]. Electron microscopy of cells infected with the ΔE variant showed a reduction in mature virions in the ERGIC and the presence of dense, granular material theorized to represent aborted virions, further, purified virions had an increased tendency to aggregate and form amorphous structures[85]. Curiously, the defect in virion formation is only partially related to the ion channel activity, as mutant viruses containing functionally inactive E protein did not suffer the same replication defect as viruses bearing no E protein. However, E

mutant viruses typically developed compensatory mutations to restore the IC channel activity and were

slowly outcompeted by wild-type or reverted virus in competitive cell culture[84]. In addition to its

function in viral morphogenesis, E protein may also promote edema and the development of ARDS, but

here the specific effect of E protein is difficult to disentangle from the general effects of reduced viral

fitness[84]. Aside from the E protein, SARS-CoV-2 encodes one additional ion channel in ORF3a that plays a

distinct role. While E protein predominantly localizes to the ERGIC compartment, ORF3a appears to

localize to a separate perinuclear space, as well as both early and late endosomes. The deletion of

ORF3a has only a modest effect on SARS-CoV-2 replication *in vitro*, but drastically reduces virulence in a

murine infection model. Surprisingly this activity was dependent on neither ion channel activity nor the

PDZ-binding motif at the C-terminus[86]. Prior experiments from SARS-CoV show that ORF3a alters the

Golgi morphology and promotes apoptosis and cell death, which like the E protein may promote

ARDS[87,88].

During the budding process, the virion incorporates a relatively small number of spike trimers

into its surface, ranging between just 15 to 33 trimers per virion[89]. While we have already extensively

discussed the structure and function of the spike protein, one important modification does take place

during the Golgi transit. This is the furin cleavage site between the S1 and S2 subunits that is cleaved by

host derived furin or furin-like proteases. Notably this furin cleavage site is not conserved in SARS-CoV-1

and has been stabilized by the D614G mutation in later SARS-CoV-2 variants to prevent premature

release of the S1 subunit[40,90]. Of the trimers incorporated on the surface, approximately 73% of them

appear in the cleaved form[89].

Although less well characterized, ORF7a may play a role in the selection of host proteins and

lipids that become incorporated into SARS-CoV-2 virions. So far, this activity has been characterized for

the antiviral protein SERINC5, which is shown to be excluded from virions in ORF7a competent SARS-CoV-2 but not ORF7a deficient variants[91].

To summarize, translation of the viral transmembrane proteins S, M, and E generates localized regions of the ERGIC that are conducive to virion formation. M proteins act as the principal coordinator by associating with S and E proteins in the membrane and recruiting RNP complexes via their cytoplasmic tails. Binding of RNP to M protein induces invagination of the ERGIC membrane and budding of new virions into the ERGIC lumen. Once there, virions transit the Golgi apparatus to the secretory vesicle compartments, where they are finally secreted by exocytosis from the host cell.

Small molecule inhibitors of Nsp15

As I have described in earlier sections, SARS-CoV-2 contains multiple proteins with the express purpose of antagonizing the interferon response. Among these antagonists is nsp15, which attracted our interest because of its well characterized function and disappointing lack of therapeutic inhibitors.

Nsp15 structure and function

Nsp15 is a nidoviral, endoribonuclease specific to uridylate (NendoU) with cleavage activity against both dsRNA and ssRNA templates. Structurally, nsp15 is composed of three domains: an N-terminal oligomerization domain, a middle domain, and a C-terminal endonuclease domain. It is expressed as part of the viral replicase polyprotein 1ab where it is cleaved at the N and C termini by the 3CL protease to separate it from the preceding nsp14 and succeeding nsp16. Once free of the polyprotein, nsp15 self-assembles with other nsp15 monomers to form a trimeric nsp15 intermediate which can further assemble into the catalytically active nsp15 homo-hexamer (dimer of trimers).

The hexameric structure of nsp15 is a critical determinant of its catalytic activity. In recombinant expression models, nsp15 primarily exists in the monomeric and hexameric states, with proportionally little of the trimeric intermediate[92]. A crystal structure of the SARS-CoV-1 nsp15 lacking the first 28 residues of the oligomerization domain reveals a misfolded catalytic site present in nsp15 monomers[93]. Further, purified fractions of SARS-CoV-2 nsp15 corresponding to the monomeric, trimeric, and hexameric states demonstrate exponential increases in substrate RNA cleavage with increasing oligomerization[92]. These observations are further complemented by single-point mutations in the three domains of MHV (T98M), MERS-CoV (N38A, Y58A, N157A), SARS-CoV-1 (E3A, D39A, R90A, N163A, E266A), and SARS-CoV-2 (K13N, G18E, L163F ,N164A), which reduce both oligomerization and catalytic activity[68,92,94-97]. Curiously, the catalytic site of the N164 variant remains dysfunctional even in the small fraction of active hexamers, suggesting that the nsp15 catalytic site is also influenced by misfolding in the middle domain[92]. These results suggest that nsp15 is subject to allosteric regulation, with the concentration of nsp15 directly impacting its nuclease activity. This regulation may be indicative of a differential need for nsp15 during the replication of coronaviruses. Low nuclease activity may be beneficial during the early phase of replication when viral RNA is limited but grow in significance as the load of viral RNA increases with each replication cycle.

In addition to the self-assembly of homohexamers, nsp15 must also make direct contact with other viral proteins. An engineered variant of MHV bearing an HA tagged nsp15 reveals distinct punctate staining of nsp15 protein in the perinuclear space and colocalizing with other members of the replication/transcription complex (RTC). Co-immunoprecipitation confirmed direct interactions between nsp8, nsp12, and nsp15 that were not simply mediated by binding to the same RNA substrate[98]. Interestingly, the localization of nsp15 within the cell is partially independent of RTC formation and differs between coronaviruses. Transfection experiments with EGFP tagged nsp15 constructs revealed

perinuclear puncta for MHV nsp15 but not for either SARS-CoV-1 or TGEV, which diffused throughout

the cytoplasm. These patterns were proven to be dependent upon enhancing and suppressive domains

in the nsp15 of each virus. Although no biochemical evidence is provided to show the proper assembly

of EGFP tagged nsp15 hexamers, it is probable that they are functional since trans-complementation of

EGFP-MHV-nsp15 drastically enhanced viral protein production in MHV infected cells[99].

Nsp15 exhibits potent nuclease activity against uridine containing RNA substrates which can be

modulated by mutations within the catalytic site and the sequence of the RNA substrate. Early

experiments performed by Bhardwaj et al determined many of the enzymatic characteristics of the

SARS-CoV-1 nsp15, which have been extrapolated to other members of Nidovirales. Those experiments

determined that nsp15 predominantly cleaves 3' of target uridylates with cleavage 3' of cytidylate only

observed in specific substrate sequences. Cleavage activity is predominantly influenced by the base 3' of

the target uridylate, with adenylate and cytidylate enhancing uridylate cleavage activity. The enzyme

also preferentially cleaves at unpaired uridylate bases in larger RNA molecules with stable secondary

structures and requires direct recognition of several moieties in the uracil base. Finally, Bhardwaj et al

determined that Mn^{2+} ions function to enhance binding between nsp15 and substrate RNA, but do not

participate in the catalysis reaction[100].

Later nsp15 mutational screens would further characterize key residues in the endonuclease

domain. The most studied residues are the catalytic triad formed by H235, H250, and K290 in SARS-CoV-

2. These residues share the general acid-base catalysis reaction and formation of a 2',3'-cyclic

phosphodiester observed in RNase A. This reaction is enabled by analogous histidine residues H12 and

H119 in RNase A, albeit without an analogous lysine residue. Notably, RNase A cleaves efficiently at both

uridylate and cytidylate, supporting the notion that K290 and perhaps other residues in the nsp15

endonuclease domain function to discriminate the two[101]. Indeed, a 2022 publication identified that

mutations in the substrate binding groove at conserved residues H235, H250, K290, S294, T341, and Y343 greatly reduced catalytic activity, with H235 being the most significant residue. Mutations H250A, K290A, S294A, and Y343A retained some cleavage activity, however they also produced cleavage products from non-uridylate bases, indicating their importance in substrate discrimination[92]. Similar descriptions of catalytic site mutations altering nuclease activity and specificity exist for the MHV-A59 virus[66].

Nsp15 and its role in the viral lifecycle

As described previously, coronaviruses possess the largest genome of known RNA viruses, a feat which requires fine-tuned mechanisms to avoid the early activation of innate immune sensors. Nsp15 helps to maintain low levels of immune activation by selectively degrading both viral dsRNA intermediates and host derived RNA (Figure 2). The studies of nsp15 function are further supplemented by the characterization of the functionally equivalent but structurally divergent nsp11 in arteriviruses.

The importance of nsp15 to viral fitness is readily apparent in nsp15 deficient coronaviruses which display severe attenuation of infection. Notably, an infectious cDNA clone of HCoV-229E bearing the inactivating nsp15 D298A mutation could not produce viral RNA following transfection into BHK-21 cells[102]. This finding was later reproduced in both MHV-A59, equine arterivirus (EAV), and porcine reproductive and respiratory syndrome virus (PRRSV) reverse genetics systems, where the respective D324A, D176A, and D180A endonuclease mutations (nsp11 in EAV and PRRSV) also could not produce viable progeny[66,103,104]. However, less severe nsp15 mutations in MHV, HCoV-229E, EAV, and PRRSV can produce viable progeny, albeit with lower titers and increased IFN-I production[66,68,104,105]. Although nsp15 is implicated in the regulation of viral genomic and sub-genomic RNAs, it remains unclear how significant this effect is on viral fitness. In EAV, nsp11 mutations create a significant block in the

production of sub-genomic mRNA compared to genomic RNA, while in MHV there is a consistent

reduction of all viral RNA[66,103].

In the context of MHV, it has been shown that nsp15 deficient virus performs similarly to wild-

type virus in cell culture systems yet is unable to establish infection in C57BL/6 mice. This loss of

infective capability could be partially restored in IFNAR knockout animals, but not double knockouts

lacking both MDA5 and TLR7[68,105]. Further, this effect appears to be largely IFNβ dependent, as MDA5^{-/-}

macrophages infected with wild-type or mutant MHV have identical IFNα production[68]. This would

suggest that nsp15 antagonizes additional intracellular pattern recognition receptors (PRRs) upstream of

IFNβ induction. Additional *in vitro* experiments found that replication of nsp15 deficient MHV could not

be restored in either MDA5^{-/-}, MAVS^{-/-}, or even IRF3/5/7 triple knockout macrophages. Interferon

induction was similar in all three models, with the least difference in infectivity present in IRF3/5/7

knockout cells, however this still amounted to a 5-fold reduction in viral titers of nsp15 deficient virus. It

was also found that nsp15 deficient virus activated antiviral pathways beyond IFN-I induction, including

the OAS/RNaseL pathway for RNA degradation and the PKR pathway for translation inhibition and

caspase-3/7 activation[68,105].

The activation of multiple pathways downstream of dsRNA sensing suggests an accumulation of

dsRNA intermediates in cells infected with mutant virus. Several experiments with both the K1 and J2

anti-dsRNA monoclonal antibodies have now demonstrated that MHV dsRNA is increased in nsp15

deficient viruses 8-12 hours post infection of bone marrow derived macrophages and permissive cell

lines[68,105,106]. In both studies with the K1 antibody, the groups found altered localization of dsRNA foci,

with an increase in "free" dsRNA not associated with replication complexes[68,106]. Carefully executed

qPCR experiments also identified a relative increase in the length and frequency of polyU containing

negative sense RNA from nsp15 deficient MHV and PEDV. These same single stranded polyU containing

RNAs were demonstrated to be PAMPs recognized by the MDA5 dsRNA sensor[106]. Taken together, these studies suggest that viral dsRNA regulation is altered in the absence of nsp15, but that the exact characteristics of this effect are dependent on the experimental model.

Beyond the modulation of viral RNA species, nsp15 also appears to modulate host RNA species to favor an immunosuppressive environment. Using luciferase reporter assays, multiple groups have now shown that overexpression of nidoviral endonucleases inhibits the activation of innate responses in the absence of a NendoU cleavable PAMP. In PRRSV, nsp11 was found to suppress luciferase expression driven by the IFN-β promoter element in response to poly(I:C) stimulation. This inhibition was dependent on suppression of both the IRF3 and NF-κB binding regions within the IFN-β promoter element. Furthermore, nsp11 from both transfection and PRRSV infection mediated this suppression by the degradation of both RIG-I and MAVS mRNA, thereby preventing IRF3 and NF-κB activation and nuclear translocation. The global transcriptome effects of nsp11 were not evaluated, but nsp11 was not found to significantly modulate either p65 or IRF3 mRNA, indicating some degree of specificity in nsp11 activity[104].

As a final note on the function of nsp15, the name NendoU is a bit of a misnomer, as the viral endonuclease is not fully conserved within the order. Notable exceptions include: mesoniviridae, which infect mosquitos; abyssoviridae, which infect sea hares; and mononiviridae, which infect flatworms[107-109]. Each of these viruses possesses similarly large genomes comparable to either coronaviruses or arteriviruses and yet do not appear to be constrained by the lack of a virally encoded endonuclease. It is therefore an attractive hypothesis that nsp15 and all other nidoviral endonucleases evolved as an adaptation to specific dsRNA sensing pathways, such as the RIG-I helicases and MAVS, present in higher organisms.

Current state of Nsp15 inhibitor development

Based on the high level of conservation of nsp15 across coronaviruses and the clear attenuation

of viruses lacking nsp15 enzymatic activity, this protein seems like an ideal target for the development of

small molecule antiviral drugs. Efforts to identify such antivirals were first published in 2010, when Ortiz-

Alacantra et al. demonstrated that the nsp15 of SARS-CoV-1, MHV, and IBV could be inhibited by the

known RNase A inhibitor benzopurpurin B[110]. As discussed in earlier sections, this shared inhibition of

nsp15 and RNase A was mediated by the convergent evolution of the catalytic domain in both nsp15 and

RNase A despite their distinct macrostructure. Unfortunately, despite the low micromolar range for

nsp15 inhibition by benzopurpurin B, the *in vitro* efficacy against SARS-CoV-1 was less than 50% even at

100μM concentrations[110]. Therefore, the results from this early study identify both the feasibility of

inhibiting nsp15 and the hurdle of doing so in the context of cellular infection and low bioavailability.

Following the initial report of benzopurpurin B, the field of nsp15 inhibitor development saw

little progress until the appearance of SARS-CoV-2 created renewed interest in coronavirus antiviral

discovery. The renewed interest effectively sextupled the body of nsp15 antiviral literature, as 5 new

publications in 2021 presented a variety of unique nsp15 inhibitors with varied intracellular and pan-

coronaviral activity. The first of these publications identified the uracil derivative Tipiracil as a potent

inhibitor of the SARS-CoV-2 nsp15 with an IC50 of 7.5μM. As with the study of benzopurpurin B, Tipiracil

also poorly inhibited viral infection of A549-hACE2 cells, with a less than 50% reduction in S protein and

RNA expression at the highest concentration of 50μM. This study ultimately lacked further

characterization in the context of cellular infection, although they were able to validate the

nsp15/Tipiracil binding interaction by the generation of crystal structures[111]. In the months after, 3 other

publications performing large drug library screens would identify the compounds NSC95397, Exebryl-1,

and epigallocatechin gallate as nsp15 inhibitors active in the single to double-digit micromolar range.

However, similar to the results for Tipiracil, each compound would ultimately fail to translate to

substantial inhibition of cellular infection (we note that EGCG does have reported activity when pre-incubated with SARS-CoV-2, but that this model is inappropriate for dissecting the effects on a protein that is only expressed post-infection)[112-114].

The final study identified a betulonic acid derivative dubbed "5h" as a specific inhibitor of nsp15 in HCoV-229E more by chance than design. Unlike the previous studies, which first identified nsp15 inhibitors and then evaluated their antiviral capacity, the study published by Stevaert et al. began by screening newly synthesized betulonic acid derivatives for inhibition of the HCoV-229E coronavirus[115]. This approach identified 5h as a compound with antiviral activity in cell culture in the high nanomolar range, without a known mechanism of action. It was only after passaging experiments in the presence of 5h that resistant HCoV-229E isolates bearing mutations K60R and T66I in nsp15 were identified and later validated using a reverse genetics system. This system was also used to generate an nsp15 knock-out strain bearing the H250A mutation, which naturally had lower titers, but was also >100-fold less sensitive to 5h[115]. Despite the success of this study in identifying an nsp15 inhibitor with substantial antiviral activity, it was ultimately found that the druggable pocket bound by 5h in the NTD of nsp15 from HCoV-229E is not conserved in SARS-CoV-2. In line with this theory, 5h lacked any substantial inhibition of either SARS-CoV-2 in VeroE6 cells, MHV-A59 in murine L2 cells, or FIPV in Crandell-Rees Feline kidney cells[115].

Antimicrobial Peptides

While SARS-CoV-2 and many other emerging zoonotic viruses have the advantage of infecting a naïve population without immune memory, this is not the same as the host population being completely defenseless. Before the evolution of adaptive immunity, many layers of innate immunity first appeared to keep viral, bacterial, fungal, and parasitic infections in check. These include physical barriers, such as

the skin or granuloma formation; cellular defenders, such as phagocytes, granulocytes, and natural killer cells; and antimicrobial peptides (AMPs), such as lysozyme, defensins, and cathelicidins. These innate defenders have each evolved in response to highly conserved components of common pathogens, and therefore exhibit broad protection against a variety of threats. As such, they are the first barrier pathogens must cross to establish infection in a new host.

Because AMPs are typically small proteins which can be delivered by either direct application or *in situ* production, they are a potential source of new therapeutics in the treatment and prevention of viral disease. Indeed, already 195 naturally occurring peptides have been identified to exhibit antiviral activity as listed in the Antimicrobial Peptide Database on June 5th 2023 (APD3)[116]. These include the peptides Urumin and Yodha, which were previously discovered by our lab to contain anti-influenza and anti-dengue virus activity[117,118]. However, in the following sections we will limit our review to the category of AMPs known as cathelicidins, which we have further explored to identify novel antiviral peptides.

Cathelicidins as a source of highly diverse AMPs

The group of AMPs known as cathelicidins was first described in in 1988 and 1989, with the isolation of the bactenecins Dodecapeptide (also known as Bac-1 or CATHL1), Bac-5, and Bac-7 from bovine neutrophils[119,120]. Despite the divergent sequences of Bac-5 and Bac-7 from Dodecapeptide, cloning of each peptides' cDNA would reveal a highly conserved pro-region with substantial similarity to porcine cathelin. The discovery of this conserved pro-region would drive a metaphorical explosion in the identification of new cathelicidin genes as the pro-region was found to be conserved across mammalian species[121]. Surprisingly, later sequencing efforts would reveal this conservation of the pro-region was not unique to mammals and appeared to be a feature of all vertebrate immune systems. This is demonstrated by the identification of homologous cathelicidin peptides in hagfish, the most distantly related vertebrate from humans on the evolutionary tree of life[122].

Like many other secreted peptides, cathelicidins are produced as immature pre-propeptides which regulates the intracellular localization and functional activity by concerted cleavage events. Cathelicidins are composed of an N-terminal signal peptide which directs ribosomal synthesis into the ER lumen followed by a cleavage event to release the propeptide. The highly conserved cathelin-like domain then serves two purposes: to maintain the associated C-terminal peptide in an inactive state and to direct the propeptide to specific storage or secretory compartments in macrophages, granulocytes, and epithelial cells. These compartments lack the endopeptidases necessary for cleavage of the propeptide, and thus cathelicidins may be stored in their inactive state until vesicle fusion with a peptidase containing compartment or secretion into the extracellular space[123]. Typically, cathelicidins are proteolytically processed into their mature forms by elastase, but several other enzymes such proteinase 3 or pepsin C can also mediate this maturation[124,125]. The segregation of the antimicrobial and sub-cellular localization determinants of cathelicidins into defined regions has likely contributed to the divergence and speciation of their C-terminal regions, as mutations to this region allow the host to adapt to new pathogenic threats without altering the regulation of the resultant peptide.

The C-terminal region of each cathelicidin is unique, although the prototypical cathelicidin is between 10 and 80 amino acids and contains a mixture of cationic and hydrophobic residues, which fold into more complex amphipathic structures. The length and similarity in amino acid composition remains relatively consistent among tetrapods, with notable exceptions including the amphibian cathelicidin OA1 and the reptilian Cm-CATH4 which contain net neutral and net negative charges respectively. By comparison, cathelicidins derived from various species of fish tend to be longer in length, with a substantially lower composition of hydrophobic residues[126]. Overall, most cathelicidins can be labeled by one of four structural motifs: the α-helical peptides; the β-turn peptides stabilized by one or two disulfide bridges; the cyclic peptides stabilized by a disulfide bridge; and finally, several classes of linear

peptides enriched in specific amino acids[121]. The sequence and structural heterogeneity of cathelicidins, but conserved pattern of expression and regulation in response to injury and barrier integrity has therefore produced a unique repertoire of peptides that may be valuable as novel human therapeutics.

Mechanisms and Specificity of Cathelicidin Activity

Cathelicidins have long been appreciated for their capacity to inhibit a variety of bacterial and fungal pathogens, as well as a more recent emphasis on viral inhibition. In most cases, this broad-spectrum activity is mediated by direct disruption of microbial membranes by the insertion of the amphipathic cathelicidin peptide. However, the exact mechanism of this disruption and efficacy against distinct pathogens varies greatly between peptides. For example, the human cathelicidin LL-37, porcine cathelicidin PMAP-36, and chicken cathelicidin CATH-2 all adopt α-helical conformations with minimal bactericidal concentrations in the 2.5 to 10μM range. However, electron microscopy of *E. coli* treated with each peptide reveals distinct modes of membrane disruption. At bactericidal concentrations, LL-37 produced a complete loss of membrane integrity with high incorporation of a membrane excluded dye in the intracellular space and significant blebbing of the bacterial membrane. By comparison, PMAP-36 and CATH-2 did not fully disrupt the membrane, however the former caused significant vesicle shedding and the latter significant membrane wrinkling[127]. Electron micrographs of *B. pseudomallei* treated with the cyclic Dodecapeptide reveal similar patterns of membrane deformation and leakage of cytosolic contents as LL-37 treated *E. coli*[128]. Like the α-helical CATH-2, the β-turn containing protegrin-1 peptide also causes *E. coli* membrane wrinkling[129]. When these peptides do not drive overt membrane lysis, they often form pores resulting in disruption of membrane transport, energy metabolism, protein synthesis, and DNA replication as has been shown for the proline/arginine rich PR-39 and proline rich indolicidin[130,131]. In general, these mechanisms of membrane disruption are broadly classified under either the carpet, toroidal pore, or barrel-stave models of peptide insertion[132].

Notably, many of these peptides rely on the differential lipid compositions of host and pathogen membranes to achieve efficient discrimination of self from non-self. Detailed analysis of protegrin-1 insertion into monolayers of either predominantly eukaryotic or prokaryotic membrane lipids highlights the specificity of this interaction[129]. More frequently, the selectivity of various cathelicidins has been investigated by comparing the minimal inhibitory concentration of peptides against their hemolysis of red blood cells or inhibition of eukaryotic cellular metabolism. For example, another investigation of protegrin-1 revealed significant heterogeneity in the cytotoxicity against specific human cell lines. Some cells such as the retinal 661W cell line possessed 6-7-fold lower IC50 values compared to NIH-3T3, however, even 661W cells are 2 orders of magnitude more resistant to protegrin-1 than common bacterial and fungal pathogens[132,133]. As expected, this pattern of self and non-self-discrimination also varies significantly between cathelicidins with peptides such as PMAP-36 and LL-37 presenting bacterial inhibitory concentrations in the low micromolar range but cellular toxicity in only the 10s of micromolar range[127]. However, it should be noted that physiological concentrations of these peptides are typically low except at sites of active inflammation, and even then, rarely reach the concentrations reported as cytotoxic[134,135]. The activity of these peptides is further tempered under physiological conditions by the presence of divalent and monovalent cations alongside polyanionic sugars[136].

Beyond their direct killing mechanisms, cathelicidins can also drive a number of other pro-inflammatory and wound repair responses via cellular signaling. This is perhaps most evident for the amphibian cathelicidin OA1, which we have previously mentioned lacks the prototypical cationic charge and displays no hemolysis or microbicidal activity against bacterial or fungal pathogens even at 1mM concentrations. This peptide possesses antioxidant properties and further promotes keratinocyte wound healing by accelerating cellular proliferation and migration *in vitro*. Notably this effect is determined by structural interactions, as scrambled peptide variants did not improve wound healing compared to

controls. This peptide was also effective in an *in vivo* mouse model of wound repair, where its activity

correlated with increased macrophage recruitment and enhanced TNF-α and TGF-β1 production[137].

However, the exact cellular mechanism by which cathelicidin OA1 induces these effects is not currently

known but is likely a mixture of non-specific interactions with the host membrane and some receptor

specific binding. In this regard, LL-37 has received substantially greater characterization and has shown

similar effects of immune cell recruitment, cytokine augmentation, wound closure, and apoptosis

(excellently reviewed in [138]). Although less studied, similar augmentation of cytokine expression, reactive

oxygen species (ROS) production, and immune cell trafficking has been reported for the python

cathelicidin CATHPb1[139].

Despite decades of research into the antibacterial, antifungal, and immunomodulatory activities

of cathelicidins, relatively little is known about their antiviral activity (See overview in Figure 3).

Although enveloped viruses such as SARS-CoV-2 derive their membranes from host cells, their

membrane composition differs by selective incorporation of lipid species. This composition influences

both the curvature and fluidity of the daughter virions, and likely has a substantial impact on the

incorporation of viral membrane proteins and membrane fusion following receptor binding. For SARS-

CoV-2, the viral envelope is similar in the composition of phosphatidylcholine and

phosphatidylethanolamine to parent cells, but with much greater incorporation of phosphatidylinositol,

and little to no incorporation of phosphatidylserine, cholesterol, or sphingomyelin[140]. As discussed

previously, cathelicidins often rely on the membrane composition to efficiently target pathogens, and

therefore enveloped viruses may be susceptible to recognition by cathelicidin peptides. As proof of this

hypothesis, LL-37 has been shown to disrupt the membrane of respiratory syncytia virus (RSV) in the low

micromolar range and thereby reduce infectivity[141,142]. Similarly, LL-37 also disrupts the membranes of

influenza A viruses (IAV) and both LL-37, the murine CRAMP, and the chicken CATH-B1 cathelicidins

inhibit IAV infection *in vitro* and *in vivo*[143,144]. Curiously, the inhibition of IAV by LL-37 and CRAMP does not appear dependent on any stereo-isomer specific interactions, as the D-peptide variants of LL-37 and CRAMP also inhibited IAV[144].

Summary

It is with this knowledge of SARS-CoV-2 virology, the history of nsp15 inhibitor development, and the potential of broad-spectrum AMPs, that the work of this thesis begins. Over the next two chapters we pursue the discovery of novel SARS-CoV-2 antivirals using library screens of *in silico* predicted nsp15 binding drugs and a selection of mammalian and reptilian cathelicidin peptides. In both approaches we identify compounds with *in vitro* efficacy against SARS-CoV-2 and favorable toxicity profiles before tracing their mechanisms of action back to viral protein and lipid interactions. Further, we explore these compounds in preclinical models of murine SARS-CoV-2 infection. Though neither the nsp15 nor AMP based candidates reduced pathology in preclinical models, these experiments have highlighted further areas of research necessary to boost each candidate's activity *in vivo* via lowering the active concentration by chemical modifications and improving therapeutic delivery. Taken as a whole, the work of this thesis contributes new small molecule and peptide therapeutic candidates and the experimental tools and protocols necessary to identify improved derivatives of each in the future.

Figures
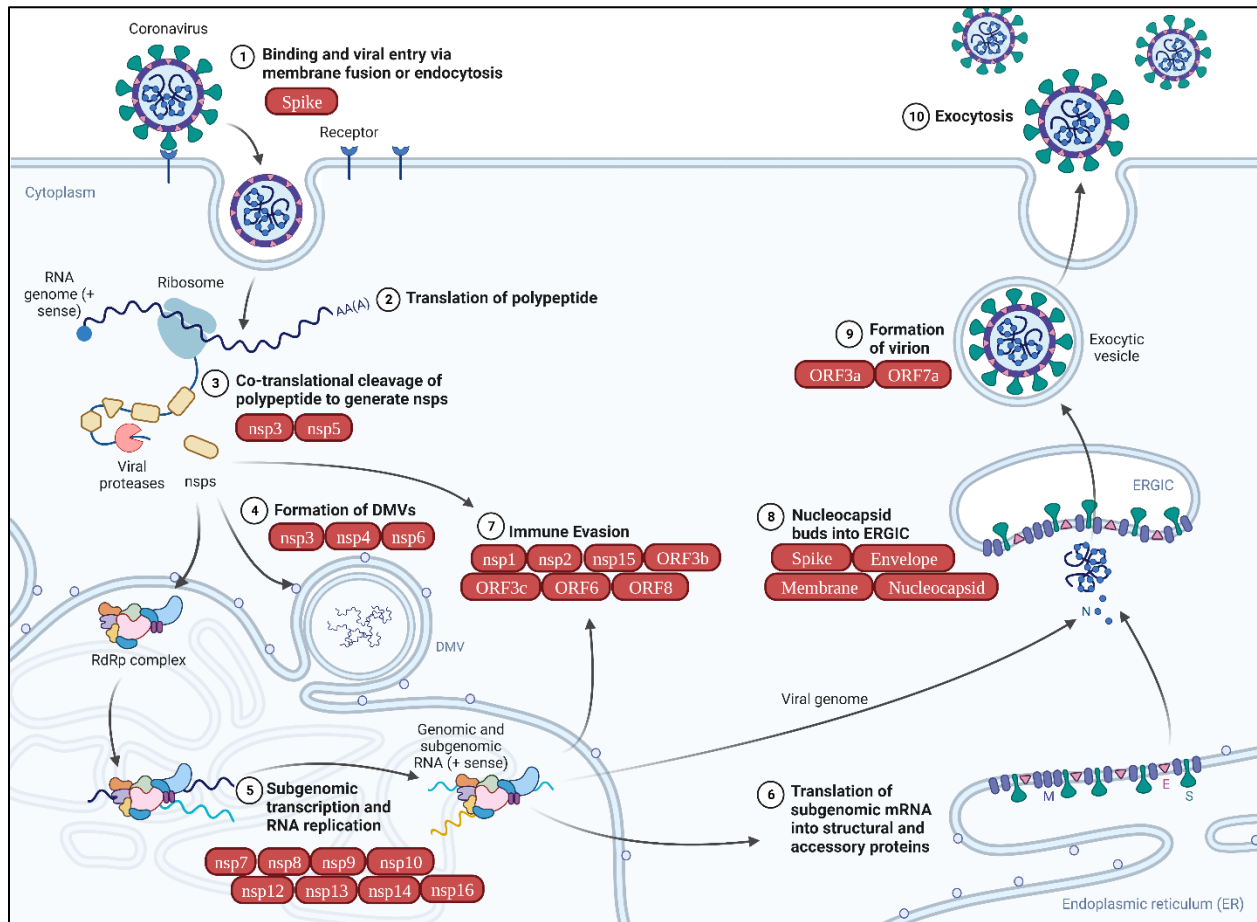
Figure 1. Overview of the SARS-CoV-2 Life cycle. Adapted from "Life Cycle of Coronavirus", by BioRender.com (2023). Retrieved from https://app.biorender.com/biorender-templates
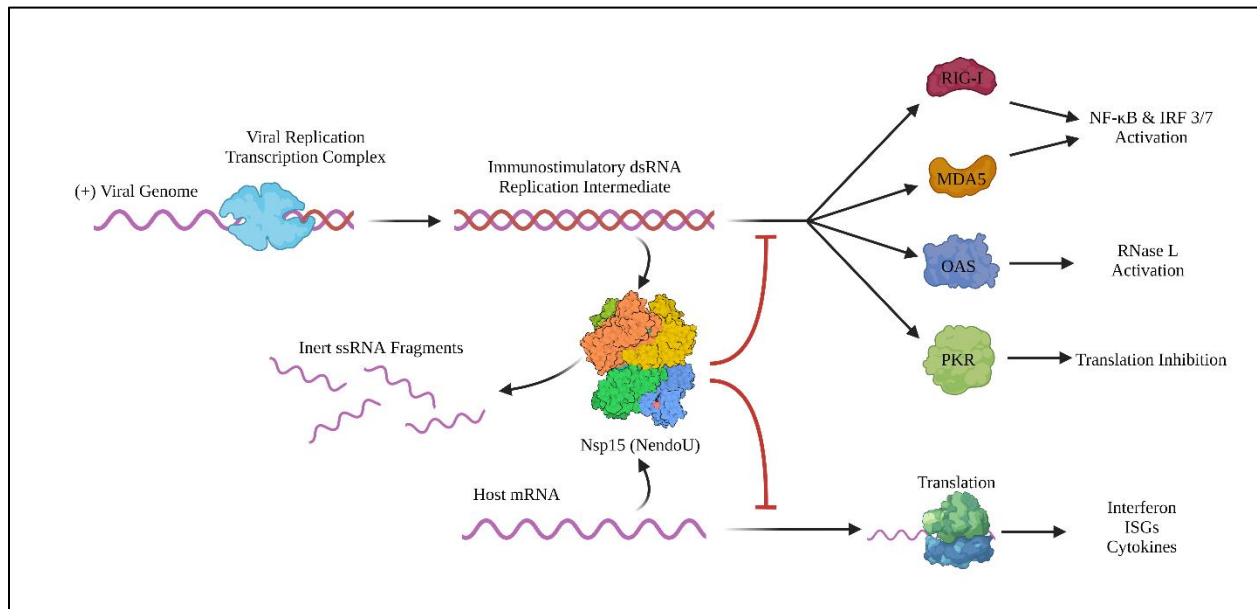
Figure 2. SARS-CoV-2 mechanism of innate immunity suppression by nsp15.
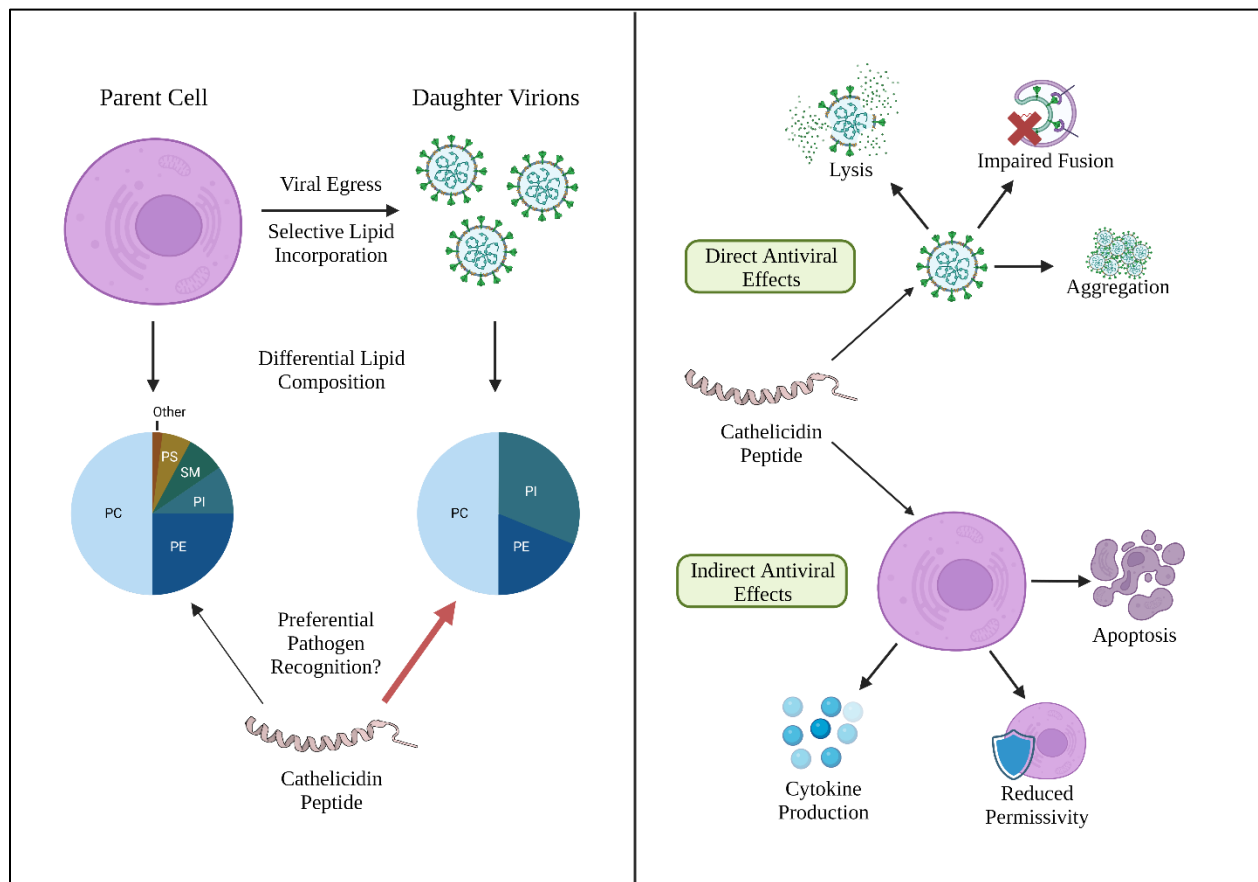
Figure 3. Mechanisms of virus recognition and neutralization by cathelicidins. **(Left)** Cathelicidin lipid targeting theory of direct virus recognition. **(Right)** Cathelicidin mediated direct and indirect mechanisms of viral inhibition. PC, phosphatidylcholine; PE, phosphatidylethanolamine; PI, phosphatidylinositol; PS, phosphatidylserine; SM, sphingomyelin.

Chapter 2: A wild boar cathelicidin peptide derivative inhibits severe acute respiratory syndrome coronavirus-2 and its drifted variants

Authors/Affiliations

Troy von Beck[1], Karla Navarrete[1], Nicholas A. Arce[2], Mu Gao[6], Gordon A. Dale[1], Meredith E. Davis-Gardner[1], Katharine Floyd[1], Luis Mena Hernandez[1], Nikita Mullick[1], Abigail Vanderheiden[1], Ioanna Skountzou[1], Suresh V. Kuchipudi[4], Rathi Saravanan[5], Renhao Li[2], Jeffrey Skolnick[6], Mehul S. Suthar[1,3], Joshy Jacob[1,7].

Author List Footnotes

[1] Emory Vaccine Center, Emory National Primate Research Center, Emory University, 954 Gatewood Road Atlanta, GA 30329, USA

[2] Aflac Cancer and Blood Disorders Center, Children's Healthcare of Atlanta, Department of Pediatrics, Emory University School of Medicine, Atlanta, GA 30322, USA

[3] Department of Pediatrics, Division of Infectious Diseases, Emory University School of Medicine, Atlanta, GA 30322, USA.

[4] Animal Diagnostic Laboratory, Department of Veterinary and Biomedical Sciences, The Center for Infectious Disease Dynamics, Pennsylvania State University, University Park, PA, 16802, USA.

[5] Lee Kong Chian School of Medicine, Nanyang Technological University Singapore, 59 Nanyang Drive, Singapore 636921, Singapore.

[6] Center for the Study of Systems Biology, School of Biological Sciences, Georgia Institute of Technology, 950 Atlantic Drive, NW, Atlanta, GA 30332, USA

Summary

The severe acute respiratory syndrome coronavirus 2 (SARS-CoV-2) poses a clear threat to humanity. It has infected over 200 million and killed 4 million people worldwide, and infections continue with no end in sight. To control the pandemic, multiple effective vaccines have been developed, and global vaccinations are in progress. However, the virus continues to mutate. Even when full vaccine coverage is achieved, vaccine-resistant mutants will likely emerge, thus requiring new annual vaccines against drifted variants analogous to influenza. A complimentary solution to this problem could be developing antiviral

drugs that inhibit SARS CoV-2 and its drifted variants. Host defense peptides represent a potential source for such an antiviral as they possess broad antimicrobial activity and significant diversity across species. We screened the cathelicidin family of peptides from 16 different species for antiviral activity and identified a wild boar peptide derivative that inhibits SARS CoV-2. This peptide, which we named Yongshi and means warrior in Mandarin, acts as a viral entry inhibitor. Following the binding of SARS-CoV-2 to its receptor, the spike protein is cleaved, and heptad repeats 1 and 2 multimerize to form the fusion complex that enables the virion to enter the cell. A deep learning-based protein sequence comparison algorithm and molecular modeling suggest that Yongshi acts as a mimetic to the heptad repeats of the virus, thereby disrupting the fusion process. Experimental data confirm the binding of Yongshi to the heptad repeat 1 with a 4-fold higher affinity than heptad repeat 2 of SARS-CoV-2. Yongshi also binds to the heptad repeat 1 of SARS-CoV-1 and MERS-CoV. Interestingly, it inhibits all drifted variants of SARS CoV-2 that we tested, including the alpha, beta, gamma, delta, kappa and omicron variants.

Introduction

Severe acute respiratory syndrome coronavirus 2 (SARS-CoV-2) is the newest member of the human Beta-coronavirus group and the causative agent of "coronavirus infectious disease 2019" (COVID-19), a disease characterized often by life-threatening viral pneumonia. SARS-CoV-2 shares over 96% genome sequence identity with a known bat coronavirus, suggesting a recent zoonotic transmission event [1]. Since first emerging in China, SARS-CoV-2 has spread globally and diverged into multiple variants with mutations permitting enhanced transmissibility and even escape from neutralizing antibodies generated by previous infection or vaccination with the original A.1 strain and A.1 spike-based vaccines [145]. The continued spread of SARS-CoV-2 and the potential emergence of highly transmissible variants of concern

and eventually a fully vaccine-resistant strain mandates the need for new therapeutic antivirals in addition to ongoing vaccine improvements.

Plants and insects lack an adaptive immune system, but they can effectively fight microbial invasion by producing host defense peptides. In 1981, Hans Boman and colleagues demonstrated that the silkworms survive bacterial infection because of a peptide in the worms' hemolymph. This was the first isolated host defense peptide, which they called cecropin [146]. Following this discovery, many other similar peptides that were discovered previously were identified as host defense peptides. Some of the most notable examples include human lysozyme discovered by Alexander Fleming in the 1920s, the peptide melittin isolated from bee venom, magainins isolated from the frog *Xenopus laevis,* as well as a family of peptides released from the granules of neutrophils that have broad-spectrum antimicrobial and antiviral capabilities called defensins [147-151]. In 1988 and 1989, the field of host defense peptides broadened with the elegant discovery of the antibacterial bactenecins Dodecapeptide, Bac-5, and Bac-7 in the cytoplasmic granules of bovine neutrophils [119,120]. Later efforts to capture the full-length cDNA of Bac-5 would serendipitously discover that Dodecapeptide, Bac-5, and Bac-7 all contained the same N-terminal pro-region with high sequence similarity to porcine cathelin [121,152].

Dodecapeptide, Bac-5, and Bac-7, along with many other examples from mammals, birds, and some fish belong to the family of host defense peptides called cathelicidins, which possess broad antimicrobial activity [153-155]. This class of peptide is characterized by its pre-pro peptide structure formed by an N-terminal signal peptide and C-terminal antimicrobial domain flanking a highly conserved cathelin-like domain. This organization permits the synthesis and storage of cathelicidins in an inert form until proteolytic processing during degranulation or phagocytosis releases the C-terminal antimicrobial domain (hereafter referred to as "cathelicidin peptide"). Most cathelicidin peptides are amphipathic and fall into

one of four structural classes: α-helical peptides, disulfide bridged β-hairpin containing peptides, disulfide bridged cyclic peptides, or linear peptides which are typically much longer than any of the afore-mentioned classes and enriched in proline, tryptophan, serine, or glycine residues [126].

Although many cathelicidin peptides have been previously described with anti-bacterial properties, relatively few have been investigated for their antiviral capabilities. Among these, only the human cathelicidin, LL-37, has received significant characterization of its antiviral activity and mechanism of action. Early experiments with LL-37 and murine CRAMP cathelicidin peptides observed inhibition of multiple influenza A virus strains both in cell culture and in murine infection experiments [144]. Later experiments with IAV, respiratory syncytia virus (RSV), and infectious bronchitis virus (IBV) indicated that LL-37 directly affects IAV, RSV, and IBV virions during cellular infection, as LL-37 added at the time of infection effectively inhibited either virus, but not when added to cells pre- or post-infection [142,143,156]. The lack of inhibition observed in pre-treated cells suggests that a minority of the inhibition is dependent on conditioning of host cells and that the majority of LL-37 is consumed within a few hours of addition. The exact mechanism of direct antiviral activity seems to be both virus and model dependent. In IAV and RSV, LL-37 produced notable disruption of virions under electron microscopy [141,143]. For IBV, no virion disruption was observed by EM and the inhibitory effect was cell-type specific, suggesting an effect on other components of viral entry, such as the viral spike or host entry receptor [156].

While cathelicidin peptides are classically depicted as relying on their amphipathicity to insert into and disrupt microbial membranes, they also stimulate an anti-microbial environment via host cell modulation and signaling. Exogenous LL-37 administration has been noted to modify the metabolic activity of host cells, their propensity for apoptosis, and their cytokine and cytokine receptor expression

[157-160]. Further, cathelicidin peptides may have augmented activity *in vivo* as they exert direct chemokine-like effects to recruit immune cells to the site of infection [161,162].

For all cathelicidins, the dichotomy of the highly conserved cathelin domain and the diverse antimicrobial domain facilitates the easy identification of putative cathelicidin peptides even from previously unexplored species. In the present study, we first identified and synthesized putative cathelicidin peptides from 16 diverse species, including bats, pangolins, humans, beluga whales, snakes, wild boar, cats, koalas, and wallabies. We then tested each of these peptides for their ability to prevent live SARS-CoV-2 from infecting permissive cells *in vitro*. Our screening identified a single cathelicidin peptide from the wild boar species, *Sus scrofa*, which possesses significant SARS-CoV-2 inhibitory activity *in vitro*. Mutational analysis and further screening of this peptide helped us create the lead-candidate peptide, Yongshi, which effectively discriminated host cells and viral particles while maintaining inhibitory activity across the alpha (B.1.1.7), beta (B.1.351), gamma (B.1.1.28.1/P.1), delta (B.1.617.2), kappa (B.1.617.1), and omicron (XBB.1.16) variants of SARS-CoV-2. We present additional *in silico* and *in vitro* binding studies that suggest Yongshi could act as a viral entry inhibitor by interfering with the SARS-CoV-2 spike protein heptad repeat 1 and 2 multimerization.

Methods

Identification of zoonotic cathelicidins

Cathelicidin peptide sequences were identified using the UniProt database and analogous peptide sequences were identified using the nBLAST databases. Sequences were analyzed for homology to the antimicrobial domain of Human Cathelicidin LL-37, as variation from LL-37 was preferred. Putative peptide

sequences were modeled using I-TASSER for antimicrobial peptide-like secondary structural features, analyzed for net charge, and then searched for preexisting characterization [163]. Sequences with 11 to 50 amino acids that were not previously described for antiviral activity were chosen as candidates.

Synthesis of cathelicidin peptides and SARS-CoV-2 peptides

Unlabeled and biotinylated zoonotic cathelicidin peptides and SARS-CoV-2 peptides were produced by standard Fmoc synthesis by Genemed Synthesis Incorporated. Peptides were purified to >95% purity by HPLC as confirmed by mass-spectroscopy. Recombinant human LL-37 was purchased from Anaspec (Catalog#: AS-61302). Recombinant OVA peptide was purchased from Invivogen (Catalog#: vac-sin). For viral inhibition and cell toxicity assays, lyophilized peptides were first reconstituted in DMSO to a concentration of 10mM before further dilution in DMEM or PBS.

Cell Lines and Growth Conditions

Vero E6 (ATCC CRL-1586) and HEK293T (ATCC CRL-1573) were purchased from ATCC. Cells were maintained at 5% CO_2 and 37°C in a humidity controlled incubator (Forma Series II model 3110) in Dulbecco's modified eagle medium (DMEM, Thermo Fisher Scientific, Catalog#: 12-614Q) supplemented with 10% heat inactivated fetal bovine serum (FBS, Rockland, Catalog#: FBS-02-500), 2mM L-glutamine (Quality Biological, Catalog#: 118-084-721) and 1X concentrations of penicillin, streptomycin, and amphotericin B (P/S/A, Quality Biological, Catalog#: 120-096-711).

SARS-CoV-2 strains and growth conditions

The following previously described isolates were used for each SARS-CoV-2 variant: A.1 (nCoV/USA_WA1/2020), B.1.1.7/Alpha (SARS-CoV-2/human/USA/CA_CDC_5574/2020), B.1.351/Beta (hCoV-19/South Africa/KRISP-k005325/2020), B.1.1.28/P.1/Gamma (hCoV-19/Japan/TY7-503/2021),

B.1.617.1/Kappa (hCoV-19/USA/CA-Stanford-15_S02/2021), B.1.617.2/Delta (hCoV-19/USA/PHC658/2021), XBB.1.16/Omicron (hCoV-19/USA/CA-Stanford-139_S23/2023) [164-166]. Viruses were passaged on Vero ACE-2 or Vero-TMPRSS2 cells and subjected to next-generation sequencing to confirm identity. Viral stocks were stored at -80°C and titered by focus forming assay on Vero E6 cells.

Data Visualization and Analysis

Data visualization and analysis for SARS-CoV-2 peptide inhibition, human RBC hemolysis toxicity, and cell viability assays was performed using GraphPad Prism 9.2.0. Outliers were defined as greater than 1.5 the interquartile range above or below the boundary of the interquartile range and excluded from analysis. Graphical axes are cut at 0% and 100%, data points beyond this range are not visualized but are included in the calculation of the mean and standard error. IC_{50} and TD_{50} values were calculated by S-curve regression of the plotted data.

SARS-CoV-2 Peptide Inhibition Assay

$2x10^4$ Vero E6 cells were seeded to each well of a poly-L lysine coated 96-well tissue culture plate (Corning, Catalog#: 354516) and allowed to adhere overnight. The following day, SARS-CoV-2 virus was diluted in DMEM without FBS or P/S/A such that 50μL contains 100 pfu of virus. 50μL of virus in DMEM was then combined with 50μL of peptide dilution in DMEM containing 2% FBS and 2X P/S/A and incubated at 37°C and 5% CO_2 for 1 hour. Media was then aspirated from Vero E6 cultures and replaced with 100μL of virus-containing media per well. Plates were then incubated at 37°C and 5% CO_2 for an additional 48 hours. Cells were fixed by removal of virus media and incubation with 2% paraformaldehyde in PBS. Cells were permeabilized by 1X PBS + 0.1% saponin (Sigma, Catalog#: 47036-50G-F) and 0.1% BSA (Sigma, Catalog#: A2153-500G). Cross-reactive SARS-CoV-1 clone CR3022 monoclonal antibody (Abcam, Catalog#: ab273073-200ug) was used to detect SARS-CoV-2 spike protein expression in combination with Goat anti-

human IgG-HRP secondary antibody (SouthernBiotech, Catalog#: 2045-05). Virus infected cells were visualized by adding TruBlue Peroxidase Substrate (SeraCare, Catalog#: 50-78-02) and the plates were scanned and the spots counted using a custom Matlab script we developed in house. All infection assays were executed in a BSL-3 lab environment following appropriate handling and disposal guidelines.

Hemolysis Toxicity Assay

Washed Red Blood Cells (RBCs) were purchased from (Innovative Research Inc, Catalog#: IWB3ALS40ML). 1 mL of RBCs was washed once in cold 1X PBS and then resuspended in 20mL of cold 1X PBS. In a 96-well format, 10μL of RBCs was added to each well containing 90μL of either peptide pre-diluted in 1X PBS, 1X PBS only, or 1X PBS + 0.1% Triton-X100 (Fisher Scientific, Catalog#: BP151-100). Cells were briefly mixed on an orbital shaker then incubated at 37°C for 1 hour with 5% CO_2. After incubation, cells were pelleted in a benchtop centrifuge at 500 rcf for 3 minutes and supernatants were collected for reading at 490nm on a Biotek Synergy 2 Multi-Mode Microplate Reader. The percentage of RBC lysis was calculated by linear regression using the PBS and PBS + 0.1% TritonX-100 as 0% and 100% lysis controls, respectively. Statistical significance was calculated by two-way ANOVA with Bonferroni's correction.

Cell Viability Assay

$2x10^4$ Vero E6 or HEK293T cells were seeded to each well of a 96-well tissue culture plate (CellTreat, Catalog#: 229197) and allowed to adhere overnight. 24 hours later, cell culture media was aspirated and replaced with 100μL peptide containing or control DMEM with 1% FBS and 1X P/S/A. Cells were then incubated at 37°C and 5% CO_2 for 48 hours. After incubation, 0% viability control wells received 1μL of NP-40 (Sigma-Aldrich, Catalog#: I3021-50ML). 5 minutes after the addition of NP-40, 20μL of CellTiter 96-Aqueous One (Promega, Catalog#: PAG3580) was added to each well and briefly mixed on an orbital shaker. Cells were incubated for 1 hour at 37°C and 5% CO_2. Plates were briefly shaken to mix

formazan products before the transfer of supernatants to a clear bottom 96-well assay plate (Costar, Catalog#: 3912). Formazan concentrations were measured at 490nm on a Biotek Synergy 2 Multi-Mode Microplate Reader. The percentage of viable cells was calculated by linear regression using DMEM-only and DMEM+1% NP-40 as 100% and 0% cell viability controls, respectively. Statistical significance was calculated by two-way ANOVA with Bonferroni's correction.

Modeling of Yongshi and SARS-CoV-2 Interactions

Initial complex models of HR1/Yongshi (2HR1/1Yongshi and 3HR1/3Yongshi) were built using SAdLSA sequence alignment and a crystal structure of HR1/HR2 complex (PDB 6LXT) as the template. Full atoms were modeled by Scwrl4 [167] and VMD [168]. Each structure was explicitly solvated in a water box, neutralized with additional ions, and minimized for 2000 conjugate gradient steps with NAMD version 2.14 [169] and CHARMM36 forcefields [170]. The 3HR/3Yongshi complex was further equilibrated by 100 ps equilibration under constant pressure and temperature conditions (NPT) and followed by 100ns equilibration under constant volume and temperature conditions (NVT). An integration time step of 2fs was employed. Full electrostatics were computed using the particle-mesh Ewald (PME) method [171]. The calculations were done on a workstation with 24 Intel Xeon Gold 6226 CPU cores and 4 Nvidia RTX6000. Run time is 62 hours for the MD simulation.

Biolayer Interferometry

Biotinylated HR1 peptides from SARS-CoV-1, SARS-CoV-2, and MERS-CoV were synthesized by Fmoc synthesis and reconstituted in 100% DMSO. SARS-CoV-2 HR2, Yongshi, and D-Yongshi were reconstituted to 1mM in DMSO. Bio-layer interferometry (BLI) experiments were performed on an Octet QK^e instrument at 25°C with plate mixing at 1000 rpm. Peptide solutions were prepared in black non-

binding plates (Greiner Bio-One, Monroe, NC) and binding responses to coated biosensors were recorded in manufacturer-supplied Data Acquisition software v11.1.1.19 (Sartorius).

All proteins were diluted in a running buffer of 20 mM HEPES, 150 mM NaCl, 0.02% Tween-20, pH 7.4. Biotinylated HR1 peptides were loaded to streptavidin sensors at 5 µg/mL to a threshold of 1.5 nm. After washing in the running buffer, the loaded sensors were moved to serial dilutions of SARS-CoV-2 HR2, Yongshi, or D-Yongshi for 100 s of association and 200 s of dissociation in running buffer. Sensors were depleted of remaining bound molecules by 3 rounds of 5s washings in 500mM NaCl followed by 5s washings in running buffer.

A heterogenous ligand binding model was fit to the collected data in Data Analysis HT software v11.1.1.39 (Sartorius). Raw data and fittings were exported to GraphPad Prism v9.1. Approximate steady state calculations were performed by plotting response at the end of association to the concentration of protein used and fit to a hyperbola.

Results

A cathelicidin peptide of Wild Boar origin inhibits SARS-CoV-2

To generate the cathelicidin peptide library, we first identified previously characterized cathelicidin genes from the genomes of other species listed on The Universal Protein Resource (UniProt) and then identified additional putative cathelicidins based on homology using BLAST (Supplementary Table 1) [172]. The cathelicidin peptide was isolated and produced by solid-phase synthesis as a pure peptide for each cathelicidin gene.

`For the initial library screening, we evaluated the inhibitory potential of each cathelicidin peptide at 50µM by an *in vitro* focus forming assay (Supplemental Figure 1) or virus infectivity assay on Vero E6

cells. Using a 50% inhibitory cutoff, our initial assay identified SARS-CoV-2 inhibitory activity in 9 out of 50 candidates in the cathelicidin peptide library including LL-37 and PMAP-36R. We then tested each 50% inhibitory candidate for activity at concentrations ranging from 50 µM to 0.78 µM using Vero E6 cells overexpressing human ACE2 (Vero hACE2) (Figure 1 and Supplemental Figure 2). Most candidates failed to achieve >50% inhibition below 50µM. Despite this trend, a candidate related to the wild boar PMAP-36 cathelicidin (PMAP-36R) maintained substantial activity even when diluted, with a calculated IC_{50} of 7.31 µM (Figure 1B).

Mutation analysis of PMAP-36R identifies key residues for SARS-CoV-2 inhibition.

To determine the critical residues in PMAP-36R responsible for its high anti-SARS-CoV-2 activity, we synthesized and tested truncated variants of the parent cathelicidin peptide lacking residues from the N or C termini, as well as a variant without the cysteine residue (Figure 1A). N-terminal truncates lacking 9, 12, or 14 residues (p9N, p12N, and p14N) displayed a progressive loss of anti-SARS-CoV-2 activity, with no inhibition present in p14N (Figure 1C). By comparison, the C-terminus was more sensitive to truncation, as loss of the last two residues in p2C immediately impaired function. At the same time, little inhibitory activity remained in p5C and none in p9C (Figure 1D). The activity of these mutants suggested that viral restriction depended on both N and C terminal amino acids (summarized in Table 1).

Interestingly, the final two residues of PMAP-36R on the C-terminus include a singular cysteine, which might be responsible for initiating covalent bonds with other PMAP-36R monomers or part of the SARS-CoV-2 virion. We also made an additional mutant of PMAP-36R by changing the penultimate cysteine to a structurally similar but non-reactive serine residue. The replacement of C36S in pSer had no significant effect on SARS-CoV-2 inhibition compared to PMAP-36R (Figure 1E).

pSer improves the viral specificity of PMAP-36R by reducing cytotoxicity.

Host defense peptides, while exhibiting antimicrobial activity, often exhibit toxicity to mammalian cells. To characterize the potential of PMAP-36R for therapeutic applications, we evaluated its toxicity toward mammalian cells via a hemolysis assay with human red blood cells (RBCs). Of the peptides we tested, LL-37 and PMAP-36R had considerable hemolytic activity. Interestingly, the C36S mutant pSer exhibited significantly reduced hemolytic activity, lysing less than 10% of human RBCs even at 50μM (Figure 2A).

In addition to the hemolysis assay, which evaluates the immediate lytic effects, each peptide was evaluated for cytotoxicity after 48 hours of cell culture. Cytotoxicity was tested against Vero hACE2 and HEK293T cells to identify general and cell line-specific sensitivities to cathelicidin peptide treatment. We quantified cell viability by a formazan formation assay. As in the hemolysis results, pSer exhibited decreased cytotoxicity compared to the parent PMAP-36R and LL-37 (Figure 2B, C). The toxicity from each peptide appeared independent of cell type, producing similar trends in all tested cell lines. In contrast to the hemolysis assay, PMAP-36R has greater toxicity than LL-37 when administered over 48 hours, suggesting that it may act via a slower mechanism than LL37 or differentially target the membranes of RBCs and adherent cell lines. As the toxicity of pSer did not reach saturation at 50μM, an additional assay was performed with Vero cells evaluated at a 24-hour timepoint. These conditions did not substantially alter the observed cytotoxicity compared to Vero cells evaluated at 48 hours. As expected, pSer reached saturation around 100μM with a calculated TD_{50} of 50.41μM (Table 1).

The therapeutic index (TI) is a measure of safety for therapeutic drugs and, in this context, is the ratio of a compound's IC_{50} to its TD_{50}. In this case, TI represents the capacity of a cathelicidin peptide to discriminate between SARS-CoV-2 virions and Vero-E6 cell membranes. LL-37 demonstrated no therapeutic potential, with a TI of <1, as neutralization consistently lagged toxicity. The TI was slightly

improved for PMAP-36R at 3.21, indicating a modest targeting of SARS-CoV-2 over Vero E6 cells. However,

pSer displayed heightened specificity for SARS-CoV-2 with a TI of 4.48. We named this peptide derivative

"Yongshi", after the Mandarin word for warrior.

Yongshi is active primarily during and after virus infection

To assess whether the inhibitory effects of Yongshi are mediated by cellular conditioning or

direct viral neutralization, we compared the efficacy of viral inhibition when Vero hACE2 cells were

treated with Yongshi 1-hour prior to, at the time of, or 1 hour after infection with SARS-CoV-2 and

compared these results against cells infected with SARS-CoV-2 that was pre-incubated with Yongshi for 1

hour (Figure 3). Pre-treatment of cells with Yongshi did not substantially inhibit SARS-CoV-2 infection at

any concentration, suggesting Yongshi does not induce a significant antiviral state in host cells as has

been described for LL-37[142]. By comparison, neither addition of Yongshi at the time of infection nor 1

hour following infection significantly altered viral inhibition compared to virus pre-incubated with

Yongshi. These results further suggest that the inhibition by Yongshi is not dependent on the extended

pre-incubation with virus but occurs rapidly at the time of infection.

Yongshi requires chirality for its virus-inhibitory activity.

Next, we tested whether peptide chirality had an impact on the effectiveness of Yongshi antiviral

activity. To do this, we synthesized a stereoisomer or mirror image variant of Yongshi using D rather than

L amino acids. The resulting peptide, D-Yongshi, has an identical sequence and amphipathicity but a

mirrored 3D conformation, permitting the dissection of Yongshi's inhibitory activity into sequence-based

and structure-based components. Compared to the L-Yongshi peptide, D-Yongshi possessed greatly

increased cytotoxicity (Figure 4A). Although we tested D-Yongshi against SARS-CoV-2, viral inhibition was only observed at concentrations that also induced substantial cell death (Figure 4B). The apparent inability of D-Yongshi to discriminate between SARS-CoV-2 and host cells supports the existence of specific interactions between L-Yongshi and Vero cells or SARS-CoV-2, dictated by secondary and tertiary structure.

Yongshi inhibits emerging SARS-CoV-2 variants of concern.

Since its emergence in late 2019, SARS-CoV-2 has continued to change: multiple new variants of concern have emerged, defined primarily by acquired mutations in the spike protein. Mutations to the receptor-binding domain, such as, L452R, E484K and N501Y have garnered particular concern as they threaten to erode the protection provided by the original A.1 isolate-based vaccines and monoclonal antibody therapies [173]. Since we identified Yongshi by screening peptides against the A.1 isolate of SARS-CoV-2, we sought to determine the extent to which Yongshi would inhibit drifted variants of SARS-CoV-2. We, therefore, tested Yongshi against five variants of concern: B.1.1.7 (alpha), B.1.351 (beta), B.1.1.28.1/P.1 (gamma), B.1.617.2 (delta), and one newly emergent variant of interest B.1.617.1 (kappa). The defining mutations of each variant are mostly concentrated in the spike S1 region responsible for ACE2 binding. The mutations in the spike protein for these variants are as follows. Alpha (69-70del, 144del, E484K, S494P, N501Y, A570D, D614G, P681H, T716I, S982A, D1118H), Beta (D80A, D215G, 241-243del, K417N, E484K, N501Y, D614G, A701V), Gamma (L18F, T20N, P26S, D138Y, R190S, K417T, E484K, N501Y, D614G, H655Y, T1027I), Kappa (T95I, G142D, E154K, L452R, E484Q, D614G, P681R, Q1071H), and Delta (T19R, V70F, T95I, G142D, E156-, F157-, R158G, A222V, W258L, K417N, L452R, T478K, D614G, P681R, D950N). Not surprisingly, the spike S2 region responsible for viral fusion is heavily conserved, especially regions corresponding to the fusion peptide and heptad repeats. The fusion peptide is conserved across

all five variants, and only the delta variant possesses a mutation in a heptad repeat (D950N) [174]. We tested Yongshi against these variant viruses and our data, shown in Fig. 5, demonstrate that as expected, Yongshi inhibited all the variants tested, albeit with reduced activity against the Alpha variant amounting to a less than 2-fold decrease in IC_{50} (Table 2). The varied sensitivity of each variant to Yongshi may reflect differences in the efficiency of membrane fusion. An increased propensity for variant fusion at the plasma membrane may underlie the observed reduction in viral inhibition.

Deep-learning sequence comparison and computational modeling predict mimicry of Yongshi to the spike HR1/HR2 regions.

What is the molecular mechanism of Yongshi's inhibition of the SARS-Cov-2 virus? A common mechanism of peptide inhibition is mimicry of functionally vital interactions. To find such a clue for Yongshi, we searched its sequence against a representative set of sequences whose structures (and some of their molecular interaction partners) have been determined in the Protein Data Bank (PDB) [175]. For this analysis, classic sequence search tools such as PSI-BLAST [176] and more sensitive HHsearch [177] yield a very small number of hits and do not find any hit related to the proteins of SARS-CoV-2. We then applied our recently developed algorithm SAdLSA [178], a deep-learning based sequence alignment method that shows significantly improved accuracy via learning the structural fold or motif representations encoded by protein sequences [179]. When applied to a recent PDB sequence library (~83,000 sequences, see Methods), among the top 1% sequences ranked in comparison to Yongshi, SAdLSA identified the Heptad Repeat 1 and 2 (HR1 and HR2) of SARS Spike protein in PDB entry 1ZV8, HR2 of SARS-Cov-2 in PDB entry 6LVN, as well as HR repeats in respiratory syncytial virus (PDB 3KPE) and Mumps virus (PDB 2FYZ). Figure 5A shows SAdLSA alignments between Yongshi and HR1/2 of SARS, SARS-CoV-2, and MERS, respectively. While the

HRs are disordered coiled coils in the pre-fusion stage of the coronaviruses, they form a 6-helix bundle serving as the "fusion core" as observed in the post-fusion conformation of the virus, whereby three HR1s form a central 3-helical bundle, and three HR2s bind to the central core forming the second layer of the complex [180,181]. SAdLSA alignments indicate that Yongshi could mimic either HR1 or HR2, with somewhat higher similarity to HR1 than HR2. The latter has disordered terminal regions that lead to a relatively lower similarity score to Yongshi. Most importantly, Yongshi also exhibits a single helical motif and displays a similar hydrophobic pattern, matching its counterpart in HR1 or HR2. Therefore, we hypothesized that Yongshi could inhibit the SARS-CoV-2 fusion machinery by disrupting the critical HR1/HR2 complex via binding to the HR1 domain. This hypothesis is supported by previous observations that a peptide mimetic of the HR2 of the SARS virus is effective in inhibiting the virus [182,183].

To evaluate the possibility that Yongshi might act as an HR1 or HR2 mimetic, we built respective structural models for both scenarios using the SAdLSA alignments (Figure 5A) and a crystal structure of HR1/2 complex of SARS-CoV-2 [181]. Figure 5B shows a structural model of two HR1s of SARS-CoV-2 complexed with one Yongshi peptide, replacing the third HR1 with the aligned Yongshi peptide. After energy minimization (see Methods), the complex is stabilized with Yongshi's hydrophobic residues fitting to the complementary hydrophobic core originally formed by HR1s. Eight positively charged lysines or arginines of Yongshi point outwards and form a charged surface patch, dramatically reducing the hydrophobic groove originally reserved for interacting with HR2s and potentially disrupts the HR1/HR2 interactions. Figure 5C shows the second structural model of three HR1s of SARS-CoV-2 in complex with three Yongshi peptides, by replacing three HR2s originally found in the template. Since there are several clashes between lysines and the hydrophobic core, we performed 100 ns molecular dynamics simulations to explore the stability of this putative complex. Figure 5C shows snapshots at the end of the MD simulation. The N-termini of the Yongshi peptides appear flexible and their movements eliminate the

originally unfavorable charged-hydrophobic interactions. In contrast, the hydrophobic interactions between the short helix of Yongshi and HR1s are well-maintained throughout the simulations with a root mean square deviation below 3Å. The modeling and MD simulation suggest that Yongshi could disrupt HR1 and HR2 interactions via two possible mechanisms by mimicking the HR1 helical core and/or competing for binding to HR1, both involving direct interactions with HR1s. We also note that the D950N mutation in the delta variant as well as the Q954H and N969K mutations in the omicron variant are unlikely to impede hypothetical interactions between Yongshi and HR1 since they occur outside the binding interface.

L-Yongshi but not D-Yongshi, binds heptad repeat 1 of SARS-CoV, MERS-CoV, and SARS-CoV-2

While computational projections are promising, experimental analysis is critical for confirmation. Using BLASTp, we identified 111 coronavirus spike protein HR1 sequences that share homology with the HR1 of SARS-CoV-2 (Fig. 6A) [172]. Out of these, we synthesized three biotinylated HR1 peptides (SARS-CoV-2 HR1, SARS-CoV-1 HR1 and MERS-CoV HR1) and tested their ability to bind SARS-CoV-2 HR2, L-Yongshi, and D-Yongshi peptides. We used bio-layer interferometry to measure the binding of immobilized HR1 peptides to serial dilutions (100 μM to 1.56 μM) of SARS-CoV-2 HR2, L-Yongshi, and D-Yongshi (Figure 6B). As expected, SARS-CoV-2 HR2 bound to the HR1 of both SARS-CoV-2 and SARS-CoV-1 with a moderate affinity of 96.7 μM and 59.5 μM respectively but showed no binding to MERS-CoV HR1. Interestingly, L-Yongshi showed dose-dependent binding to all three HR1 peptides tested (SARS-CoV-1, MERS-CoV, and SARS-CoV-2), suggesting that Yongshi could potentially act as a pan-coronavirus entry inhibitor. Among the three HR1 peptides, L-Yongshi bound with the strongest relative affinity to the HR1 of SARS-CoV-1 (23.55 μM). L-Yongshi bound to SARS-CoV-2 HR1 with an approximately 4-fold stronger affinity (24.1 μM) than SARS-CoV-2 HR2 (96.7 μM), indicating that it could potentially outcompete HR2 for binding to HR1.

As a control, we tested D-Yongshi for binding to all three HR1 peptides, and the D-enantiomer did not show binding to any HR1 peptides up to 100 µM. These binding experiments suggest that Yongshi can both specifically bind to the HR1 of coronaviruses and that it could outcompete HR2 for binding to HR1. The specificity of this interaction is dependent on some secondary structure as the chirality (L- vs. D-enantiomer) is critical for binding. Thus, we posit that Yongshi could act as a viral entry inhibitor by blocking the fusion machinery of coronaviruses.

Discussion

Here we identified a cathelicidin peptide of wild boar origin that inhibits SARS-CoV-2 and exhibits binding to the HR1 of SARS-CoV-2 spike protein. The specificity of this interaction is further supported by the inability of the mirror-image peptide, D-Yongshi to target SARS-CoV-2 or bind to the HR1 peptide. This interaction may contribute to the observed inhibition of SARS-CoV-2 but is likely only one of several mechanisms in addition to direct effects on the viral membrane or induction of an antiviral state in host cells. These results identify how Yongshi can act via both direct and indirect mechanisms, presenting multiple avenues for further engineering of peptide derivatives. Further, as SARS-CoV-2 has undergone significant evolution since our initial studies, we repeated our analysis with the recent XBB.1.16 variant and find that Yongshi continues to provide substantial virus inhibition on par with the original wild-type virus (Figure 9).

For millennia, host defense peptides have co-evolved with their hosts to best protect them against pathogens in their niche. Unlike antibodies or T cell receptors which are highly diverse, and which the individual host makes $>10^7$ specificities, host defense peptides are produced in very limited numbers; for instance, humans produce a single cathelicidin LL-37. Yet these host defense peptides work because they often target an Achilles' heel or a conserved motif that is crucial for microbial survival. These targeted

motifs are often common among multiple pathogens, even those that do not infect the given species. Because of this feature, if a pathogen contains the motif or element that the peptide acts upon, the host defense peptide can cross-neutralize that bacteria or virus, regardless of the species that encounter it. It is highly unlikely that Yongshi arose to combat SARS-CoV-2 as the virus only recently emerged, but instead Yongshi confers the wild boar protection against some related virus that bears a complementary HR1 peptide. In this context, Juergen Richt and colleagues have reported that five-week-old pigs are not susceptible to infection with SARS-CoV-2 infection. Briefly, they infected pigs with 10^6 TCID$_{50}$ dose of SARS-CoV-2 via oral, intranasal or intratracheal route and the virus did not replicate in pigs, and they did not produce antibodies against SARS-CoV-2 either [184]. Whether this protection is due to the Yongshi-related cathelicidin, PMAP-36 remains to be investigated.

Regarding the specific mechanism of HR2 mimicry, several other purpose-built HR2 mimetics have been previously described to inhibit SARS-CoV-2. Early HR2 mimetics designed against SARS-CoV-2 used the core HR2 region (amino acids 1163-1202) with additional amino acid substitutions or peptide modifications to achieve viral IC$_{50}$ values in the low micro-molar to high nano-molar range [47,181,185-187]. Recently, a crystal structure of an extended HR1HR2 6-helix bundle led to the design of an extended HR2 mimetic which achieves an impressive IC$_{50}$ of 1.5nM against SARS-CoV-2. This activity was dependent on the expression of TMPRSS2 for receptor mediated entry and was maintained against alpha, delta, and omicron variant viruses with similar active concentrations [188]. It is not surprising that HR2 derived peptides can vastly outcompete Yongshi in performance as an HR2 mimetic, however, it is curious that Yongshi achieves comparable inhibitory activity to the unmodified, core HR2 region which varies by model system and is reported between 0.98µM and 33.74µM [47,186,187]. Given that Yongshi also aligns closely with the heptad repeats of RSV and Mumps, we hypothesize that PMAP-36R may have evolved in response to multiple endemic porcine viruses to achieve broad heptad repeat compatibility. It is unclear whether

PAMP-36R is expressed at the level necessary to achieve this activity in nature, but LL-37 has been reported in humans at 20μg/mL (~4.5μM) in bronchoalveolar lavage fluid and up to 80μg/mL (~17.8μM) in nasal secretions. Notably these concentrations are attained in response to systemic and local inflammation, with healthy individuals producing significantly less peptide [134,135].

In searching for the previous characterization of the Yongshi sequence, we identified that the Yongshi peptide is two amino-acids longer than the mature PMAP-36 cathelicidin, which lacks the N-terminal valine and undergoes a C-terminal amidation reaction which removes the terminal glycine [189]. Although PMAP-36 has not been studied in the context of viral infection, multiple publications demonstrate a bacterial inhibition curve similar to the inhibition of SARS-CoV-2 by Yongshi. In the context of *E. coli*, Scheenstra and colleagues demonstrated a minimal bactericidal concentration for PMAP-36 in the range of 5 to 10 μM. Further, removing up to 11 N-terminal residues or mutation of cysteine to serine did not reduce *E. coli* killing potential but reduced cell toxicity as measured by both porcine RBC hemolysis and RAW264.7 cell mitochondrial activity in culture [127]. While our model describes a specific interaction between Yongshi and SARS-CoV-2, the parallel effects of mutagenesis against SARS-CoV-2 and *E. coli* suggest the mechanism of action has shared components whether the target is viral or bacterial. Alternatively, transmission electron micrographs of PMAP-36 treated *E. coli* document vesicle shedding, a bacterial stress response to lipid asymmetry [127,190]. Combined with our results, this observation may indicate that SARS-CoV-2 is susceptible to lipid asymmetries caused by Yongshi, but not the amphipathic mechanisms of other cathelicidins [191].

L-Yongshi, but not D-Yongshi, inhibits SARS-CoV-2 and its drifted variants. Amino acids can be produced as enantiomers, which are mirror images of each other. Of these two configurations, the L-enantiomer, in contrast to the D-enantiomer, is almost exclusively produced naturally. Because of this, host proteases, for the most part, only demonstrate enzymatic activity against the L-enantiomer of

peptides and proteins. In contrast, D-enantiomer peptides and proteins are not susceptible to this natural degradation. However, since only the L-Yongshi demonstrated antiviral activity, we must formulate L-Yongshi appropriately, for therapeutic or prophylactic evaluation *in vivo*. While Yongshi possesses some inhibitory activity, further modifications to the peptide are necessary to generate a therapeutically viable product. Given the existence of purpose built HR2 mimetics with much lower IC_{50} ranges than Yongshi, future designs should further explore the cellular effects of Yongshi or the ability to differentially disrupt viral and host membranes. Additionally, we note that administering Yongshi as a single bolus is sub-optimal in that it increases immediate cytotoxicity and has a short half-life for cellular protection. A better approach may be to design Yongshi as a synthetic cathelicidin to be delivered by an mRNA vector and thereby produced locally *in situ*.

Figures

A
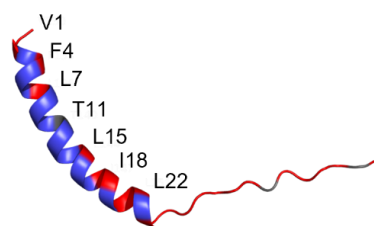
|	
PMAP-36R	NH$_2$-VGRFRRLRKKTRKRLKKIGKVLKWIPPIVGSIPLGCG-COOH
pSer	NH$_2$-VGRFRRLRKKTRKRLKKIGKVLKWIPPIVGSIPLG**S**G-COOH
p9N	NH$_2$-KTRKRLKKIGKVLKWIPPIVGSIPLGCG-COOH
p12N	NH$_2$-KRLKKIGKVLKWIPPIVGSIPLGCG-COOH
p14N	NH$_2$-LKKIGKVLKWIPPIVGSIPLGCG-COOH
p2C	NH$_2$-VGRFRRLRKKTRKRLKKIGKVLKWIPPIVGSIPLG-COOH
p5C	NH$_2$-VGRFRRLRKKTRKRLKKIGKVLKWIPPIVGSI-COOH
p9C	NH$_2$-VGRFRRLRKKTRKRLKKIGKVLKWIPPI-COOH
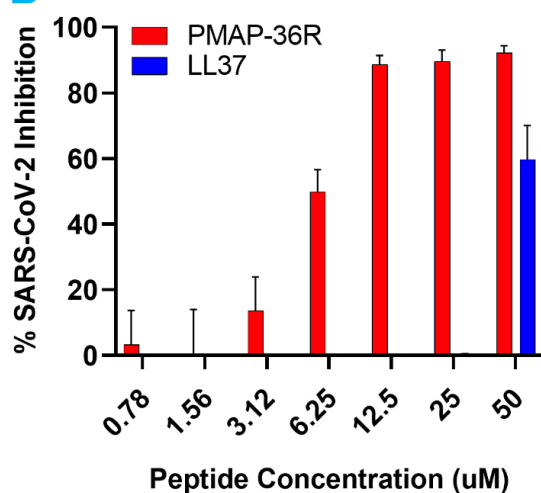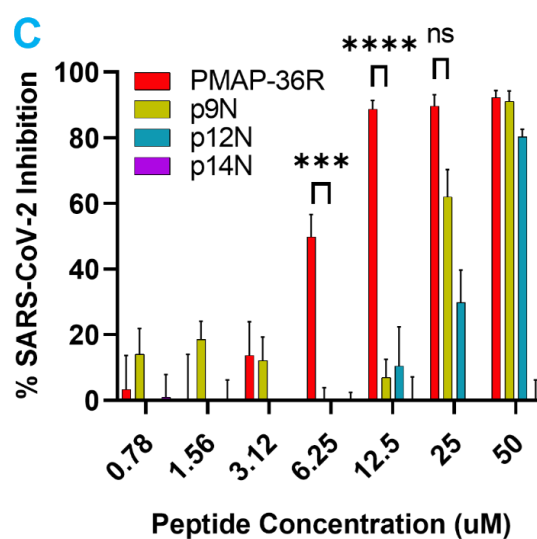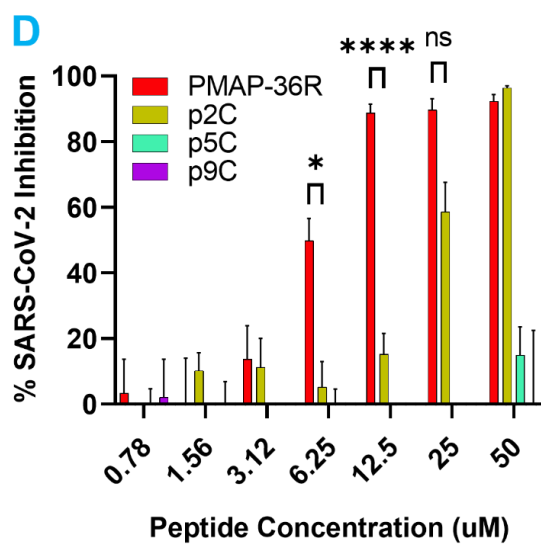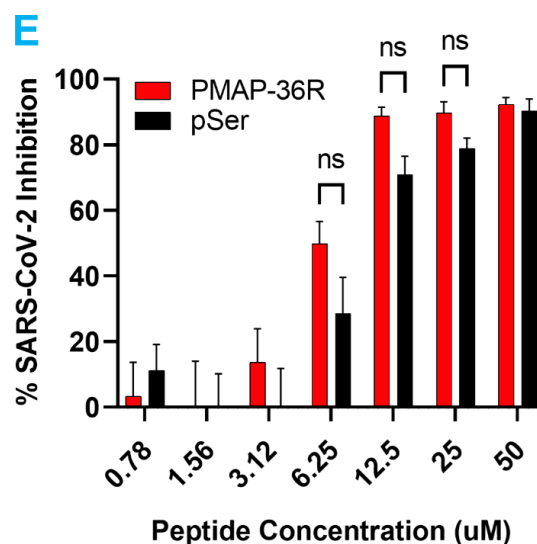
Figure 1. A wild boar cathelicidin PMAP-36R inhibits SARS-CoV-2 infection of Vero hACE2 cells. (A) 3-dimensional structure projection of PMAP-36R (left) and schematic of PMAP-36R variants (right). A 3D structure of PMAP-36R was determined by AlphaFold (P49931) and rendered in PyMOL [192,193]. Positively charged residues are depicted in blue while hydrophobic residues are depicted in red. Labeled residues along the N-terminal α-helix form a non-polar sector including the weakly hydrophilic threonine. (B-E) Inhibition of SARS-CoV-2 infection by PMAP-36R and its derivatives. PMAP-36R was compared against LL-37 (B), N-terminal truncations (C), C-terminal truncations (D), or a cysteine mutant (E) of PMAP-36R. Peptides at the labeled concentrations were pre-incubated with 100pfu of live SARS-CoV-2 virus (nCoV/USA_WA1/2020) for 1 hour at 37° C before addition to confluent Vero hACE2 cells in a 96-well plate. Infected cells were fixed and quantified by focus forming assay after 48 hours. Inhibition of viral infection was calculated based on the percent area of each well staining positively for viral spike protein compared to control wells without peptide inhibitor treatment. Results are representative of 3 independent experiments performed in triplicate. Significance calculated by two-way ANOVA with Bonferonni's correction comparing peptide derivatives against control PMAP-36R (*<.05, **<.01, **<.001, *<.0001).
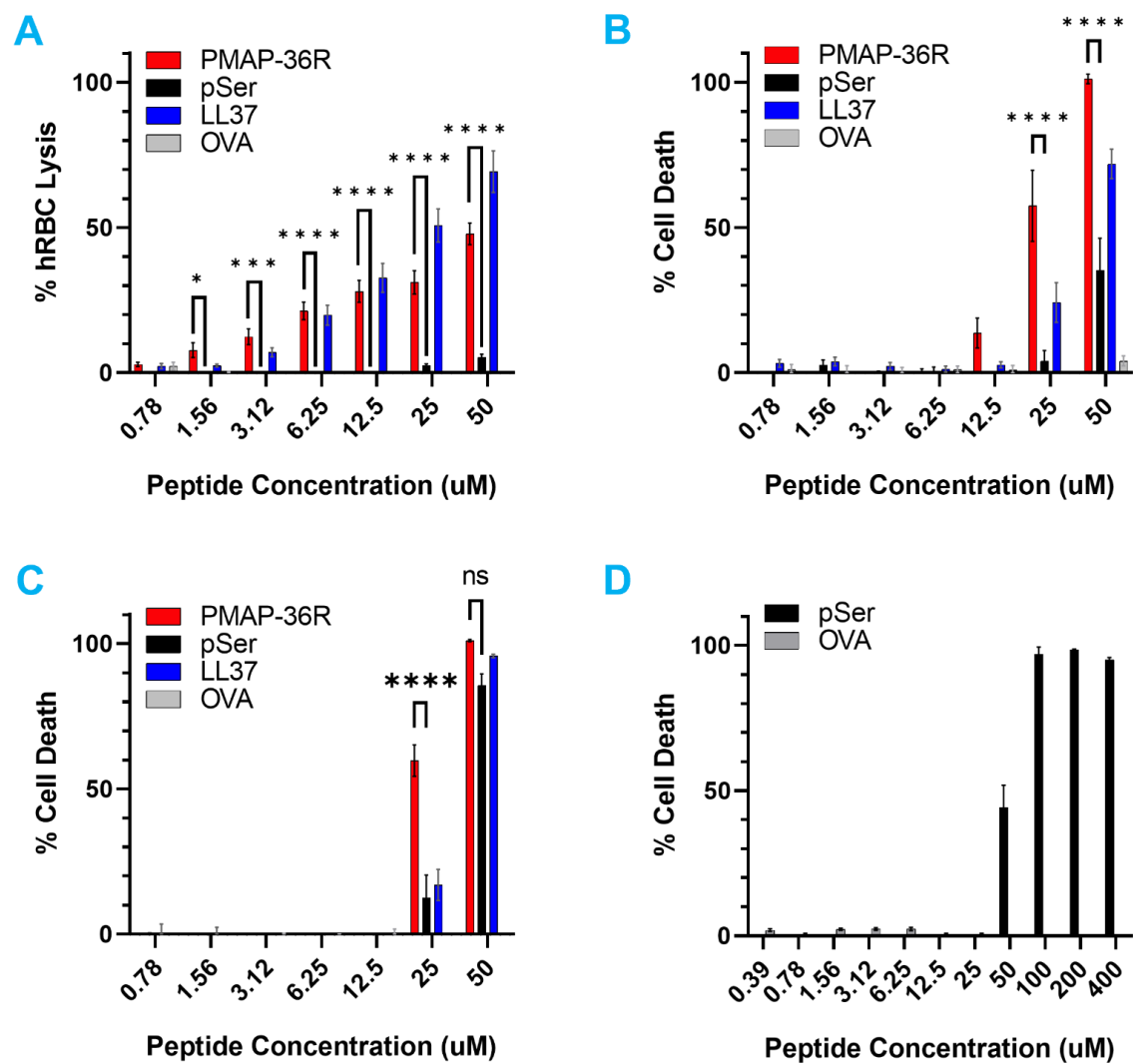
Figure 2. The PMAP-36R cathelicidin derivative pSer possesses reduced cytotoxicity. (A) human RBC hemolysis assay showing reduced lytic activity of pSer compared to PMAP-36R or LL-37. Peptides at the labeled concentrations were incubated with human RBCs for 1 hour at 37° C in 1X PBS buffer. RBC lysis was determined by the spectral absorbance (490nm) of cell supernatants relative to PBS-only and TritonX-100 containing controls. (B-C) MTS formazan formation assay with (B) Vero hACE2, and (C) HEK-293T cell lines showing reduced cell death in wells receiving pSer compared to PMAP36-R. Peptides at the labeled concentrations were incubated with cells in 1% FBS containing DMEM for 48 hours prior to the addition of MTS substrate. The percentage of cell death was calculated relative to untreated and NP-40 receiving control wells. Results are representative of 3 independent experiments performed in triplicate. (D) MTS formazan formation assay with the Vero A2T2 cell line showing saturation of toxic effect at 100µM. Peptides at the labeled concentrations were incubated with cells in 1% FBS containing DMEM for 24 hours prior to the addition of MTS substrate. The percentage of cell death was calculated relative to untreated and NP-40 receiving control wells. Results are representative of 2 independent experiments performed in duplicate. Significance calculated by two-way ANOVA with Bonferonni's correction comparing pSer against control PMAP-36R (*<.05, **<.01, **<.001, *<.0001).
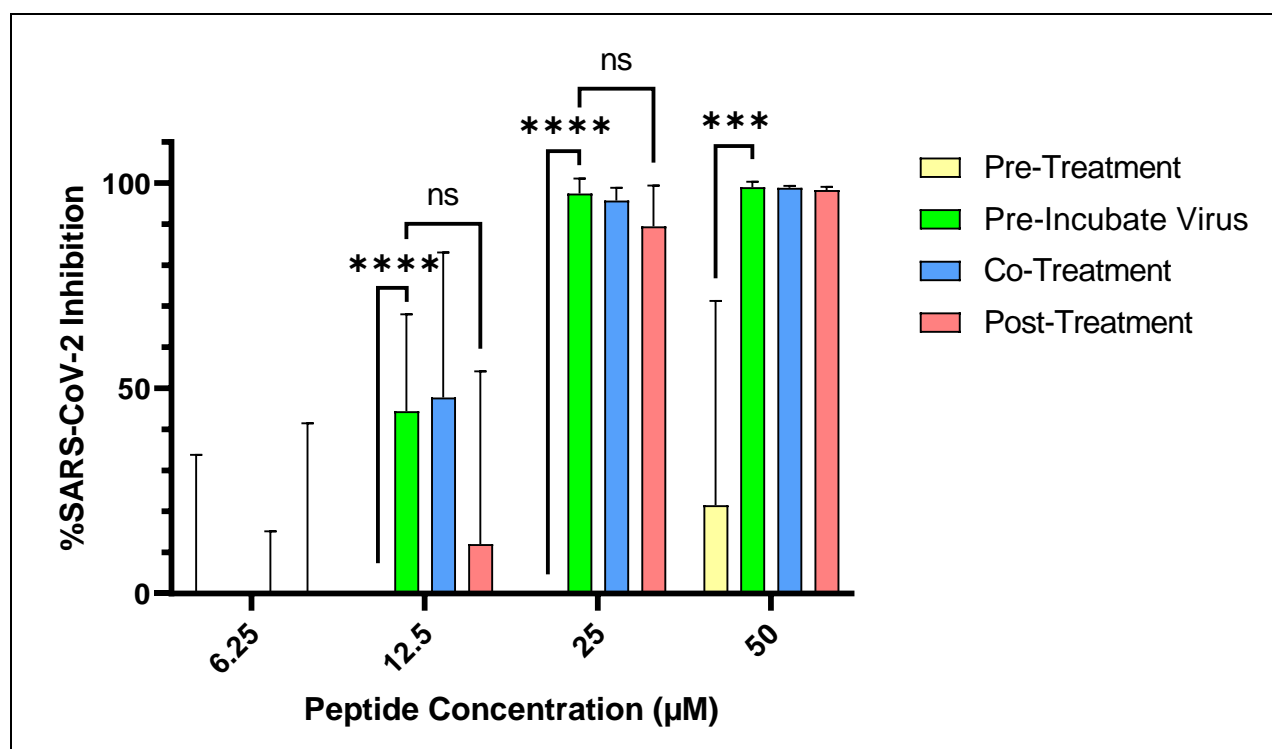
Figure 3. The PMAP-36R derivative Yongshi (pSer) mediates SARS-CoV-2 inhibition via acting on both virions and cells. Inhibition of SARS-CoV-2 infection of Vero A2T2 cells. Peptides at the labeled concentrations were pre-incubated with virus for 1 hour or added directly to cells 1 hour before, at the time of, or 1 hour after infection with 100pfu of SARS-CoV-2 (nCoV/USA_WA1/2020). For pre-treatment groups, the added peptide was removed immediately prior to infection and replaced with control medium. Infected cells were fixed and quantified by focus forming assay after 48 hours. Inhibition of viral infection was calculated based on the percent area of each well staining positively for viral spike protein compared to control wells without peptide inhibitor treatment. Results are representative of 2 independent experiments performed in triplicate. Significance calculated by two-way ANOVA with Bonferonni's correction comparing each group against pre-incubated virus (*<.05, **<.01, **<.001, *<.0001).
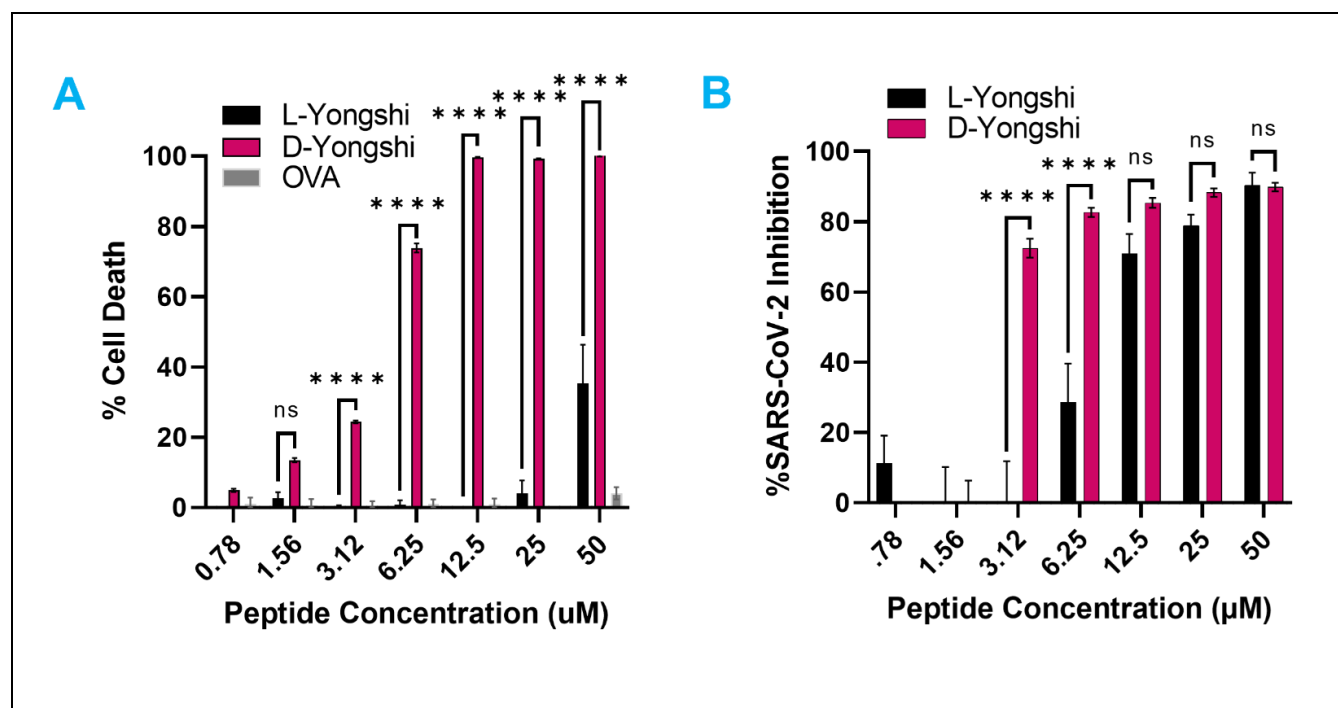
Figure 4. The D-enantiomer of Yongshi loses SARS-CoV-2 specificity. (A) Toxicity towards Vero hACE2 cells was evaluated by MTS formazan formation assay. Peptides at the labeled concentrations were incubated with cells in 1% FBS containing DMEM for 48 hours prior to the addition of MTS substrate. The percentage of cell death was calculated relative to untreated and NP-40 receiving control wells. (B) Inhibition of SARS-CoV-2 infection of Vero hACE2 cells. Peptides at the labeled concentrations were pre-incubated with 100pfu of live SARS-CoV-2 virus (nCoV/USA_WA1/2020) for 1 hour at 37° C before addition to confluent Vero hACE2 cells in a 96-well plate. Infected cells were fixed and quantified by focus forming assay after 48 hours. Inhibition of viral infection was calculated based on the percent area of each well staining positively for viral spike protein compared to control wells without peptide inhibitor treatment. Results are representative of 3 independent experiments performed in triplicate. Data for L-Yongshi is reproduced from figures 1 and 2. Significance calculated by two-way ANOVA with Bonferonni's correction comparing D-Yongshi against control L-Yongshi (*<.05, **<.01, **<.001, *<.0001).
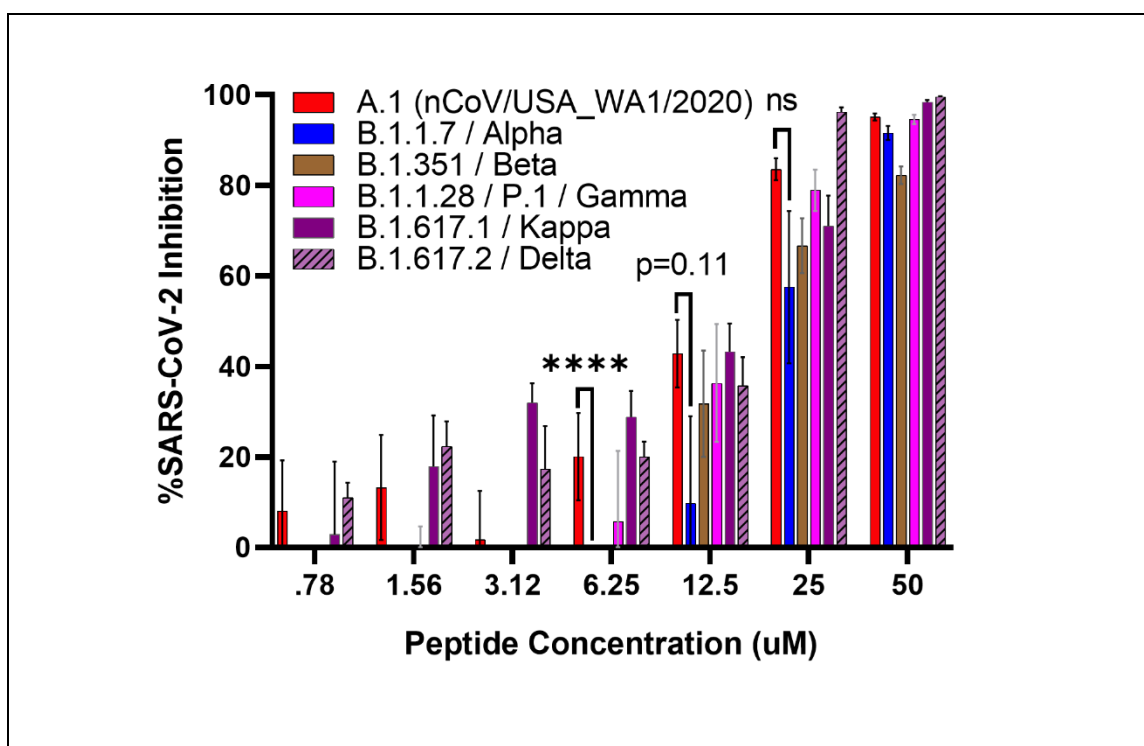
Figure 5. Yongshi retains inhibitory activity against emergent SARS-CoV-2 variants alpha, beta, gamma, kappa, and delta. Dilutions of the Yongshi peptide were tested for inhibition of SARS-CoV-2 and its drifted variants. Peptides at the labeled concentrations were pre-incubated with 100pfu of the indicated SARS-CoV-2 variant virus for 1 hour at 37° C before addition to confluent Vero hACE2 cells in a 96-well plate. Infected cells were fixed and quantified by focus forming assay after 48 hours. Inhibition of viral infection was calculated based on the percent area of each well staining positively for viral spike protein compared to control wells without peptide inhibitor treatment. Results are representative of 2 to 3 independent experiments performed in triplicate. Significance calculated by two-way ANOVA with Bonferonni's correction comparing A.1 inhibition against each variant (*<.05, **<.01, **<.001, *<.0001).

Figure 6. Deep-learning sequence alignment algorithm and computational modeling predict stable binding interactions between Yongshi and HR1. (**A**) Sequence alignments between Yongshi and HR1/HR2 sequences of SARS-CoV-1, SARS-CoV-2, and MERS-CoV by SAdLSA [178]. <D> denotes the mean of predicted distance between aligned residues, and SeqID is Sequence Identity. Identical and statistically favorable amino acid substitutions are denoted by "*" and "+", respectively. The digits below each alignment indicate the probability that the predicted structural for each aligned amino acid pair will be less than 3 Å, e.g., the number 6 predicts a probability score between 60 to 70%. Note that SARS-CoV-1 and SARS-CoV-2 have identical sequences in their HR2 regions aligned to Yongshi. (**B**) A structural model of two SARS-Cov-2 HR1s in complex with a single Yongshi peptide. The two HR1s are shown in the surface representation, and the Yongshi peptide is shown in ribbon backbone and Licorice sidechain representations in the upper snapshot, and the same surface representation in the lower snapshot. The lower snapshot is slightly rotated from the upper snapshot to show a large positively charged surface patch of Yongshi as pointed by a yellow arrow. The color codes for amino acids are hydrophobic (white), polar (green), positive (blue), negative (red). (**C**) A structural model of three SARS-Cov-2 HR1s in complex with three Yongshi peptides after 100ns of MD simulation. The upper snapshot is shown in cartoon representation for three HR1s (blue, cyan, grey), and ribbon representation for Yongshi (yellow). The lower snapshot is in the same orientation as the upper one but shown in the same representation as snapshots in (B).

Figure 7. Phylogenetic tree of HR1 segments in disparate coronaviruses. 111 coronavirus spike protein HR1 sequences that share homology with the HR1 of SARS-CoV-2 were identified by BLASTp[172]. Sequences were aligned using MUSCLE and the resultant phylogenetic tree was visualized with ggtree[194,195]. Three of the HR1 sequences (red) were analyzed in detail in panel B and they share a common ancestor sequence near the root of the tree. The inferred breadth of coverage is shaded (blue). The three HR1 peptides we tested for binding with Yongshi peptide are marked in red.
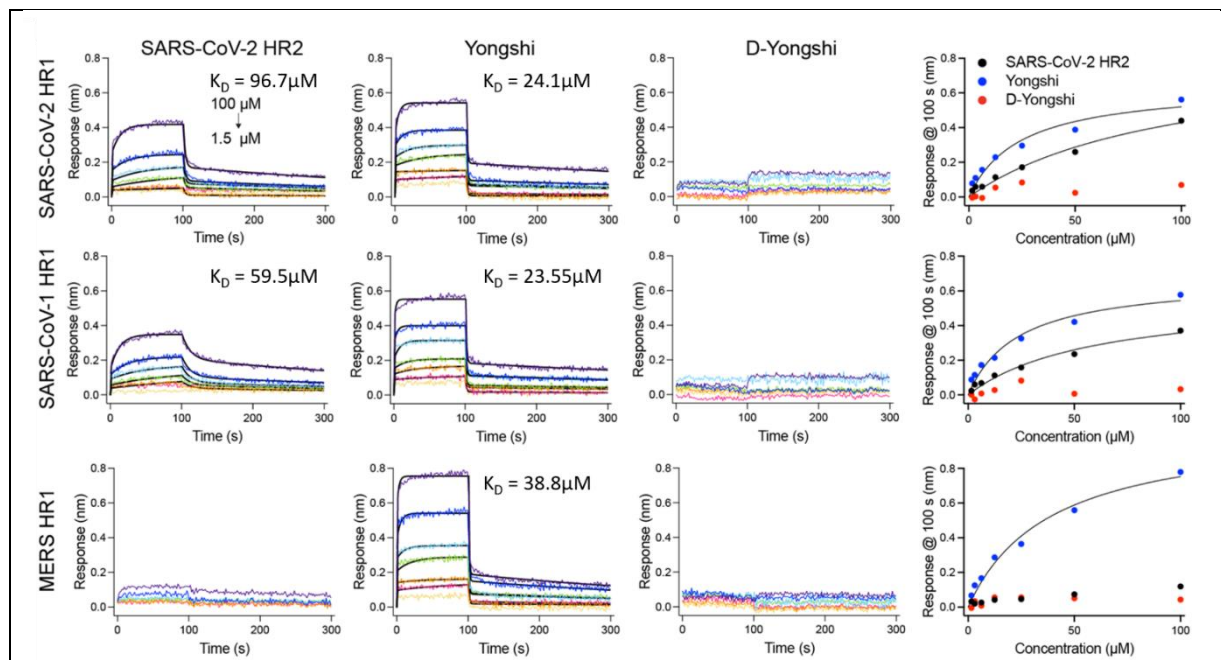
Figure 8. Yongshi binds to HR1 peptide with higher affinity than HR2. Biotinylated HR1 peptide from SARS-CoV-2, SARS-CoV-1, or MERS-CoV was bound to a streptavidin-coated bio-layer interferometry sensor and incubated with serial dilutions of either SARS-CoV-2 HR2, Yongshi, or D-Yongshi starting from 100μM. (A) Representative plots of peptide binding over 100s of association followed by 200s of dissociation. (B) Regression analysis of the peptide binding response at each concentration after 100s of association. Relative steady state affinities were derived from the K_D of the hyperbola.
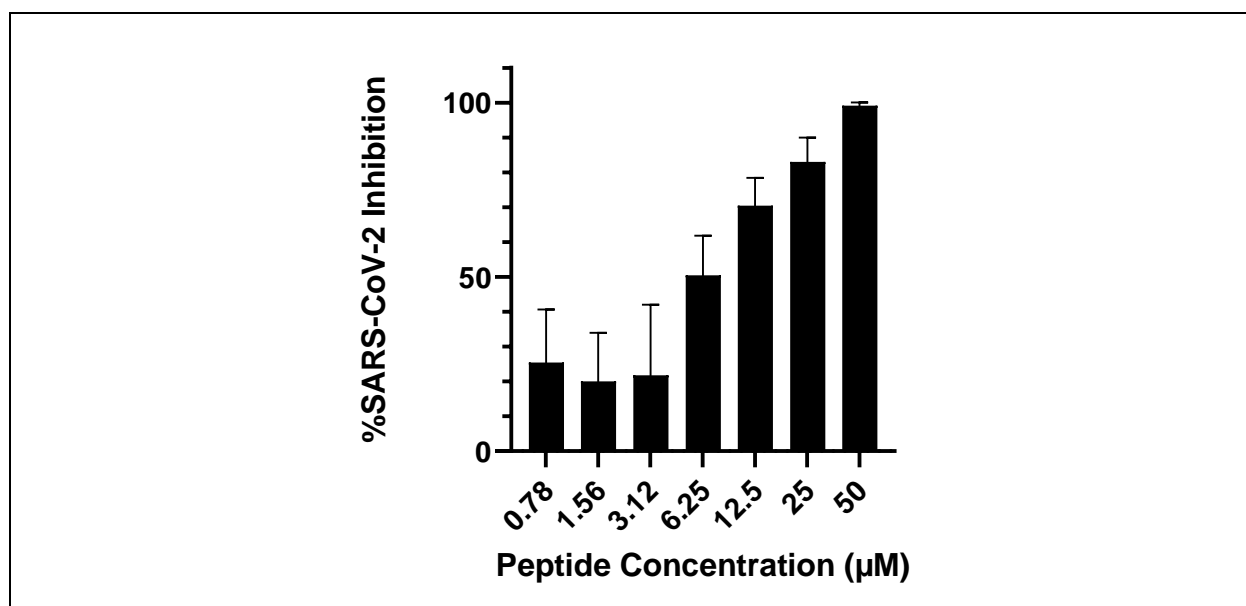
Figure 9. Yongshi remains active against the SARS-CoV-2 Omicron Variant. Peptides at the labeled concentrations were pre-incubated with 100pfu of the SARS-CoV-2 XBB.1.16 variant virus for 1 hour at 37° C before addition to confluent Vero hACE2 cells in a 96-well plate. Infected cells were fixed and quantified by focus forming assay after 24 hours. Inhibition of viral infection was calculated based on the percent area of each well staining positively for viral spike protein compared to control wells without peptide inhibitor treatment. Results are representative of 2 independent experiments performed in triplicate.

Tables

	SARS-CoV-2 IC$_{50}$ (µM)	RBC Hemolysis TD$_{50}$ (µM)	Vero TD$_{50}$ 48 hour (µM)	HEK293T TD$_{50}$ (µM)	Vero TD$_{50}$ 24 hour (µM)
LL-37	49.27	30.53	39.44	26.61	NA
OVA	NA	>50	>50	>50	>400
PMAP-36R	7.31	>50	23.47	24.61	NA
Yongshi (pSer)	11.24	>50	>50	26.98	50.41
p9N	23.73	NA	NA	NA	NA
p12N	25.2	NA	NA	NA	NA
p14N	>50	NA	NA	NA	NA
p2C	22.68	NA	NA	NA	NA
p5C	>50	NA	NA	NA	NA
p9C	>50	NA	NA	NA	NA

Table 1. Calculated IC$_{50}$ and TD$_{50}$ values for PMAP-36R derivatives and control LL-37 or OVA peptides. IC$_{50}$ and TD$_{50}$ values were calculated for each peptide by S-curve regression.

Variant	IC$_{50}$ (µM)
A.1	12.13*
B.1.1.7 (Alpha)	20.54
B.1.351 (Beta)	21.64
B.1.1.28 (Gamma)	16.11
B.1.617.1 (Kappa)	17.34
B.1.617.2 (Delta)	13.28

Table 2. Calculated IC$_{50}$ values for Yongshi against drifted SARS-CoV-2 variants. IC$_{50}$ values were calculated for each variant by S-curve regression. *The IC$_{50}$ of A.1 is calculated from a set of experiments performed at the same time as the other variants and therefore varies slightly from the IC$_{50}$ presented in Table 1.

Supplemental Information

Peptide Name	Sequence	Species	NCBI/Uniprot Reference Sequence
PMAP-36R	VGRFRRLRKKTRKRLKKIGKVLKWIPPIVGSIPLGCG	*Sus Scrofa*	NP_001123437.1
p9N	KTRKRLKKIGKVLKWIPPIVGSIPLGCG	Truncation of PMAP-36R	
p12N	KRLKKIGKVLKWIPPIVGSIPLGCG	Truncation of PMAP-36R	
p14N	LKKIGKVLKWIPPIVGSIPLGCG	Truncation of PMAP-36R	
p2C	VGRFRRLRKKTRKRLKKIGKVLKWIPPIVGSIPLG	Truncation of PMAP-36R	
p5C	VGRFRRLRKKTRKRLKKIGKVLKWIPPIVGSI	Truncation of PMAP-36R	
p9C	VGRFRRLRKKTRKRLKKIGKVLKWIPPI	Truncation of PMAP-36R	
Yongshi (pSer)	VGRFRRLRKKTRKRLKKIGKVLKWIPPIVGSIPLGSG	Serine Mutant of PMAP-36R	
D-Yongshi	(All D-amino acids) VGRFRRLRKKTRKRLKKIGKVLKWIPPIVGSIPLGSG	D-Enantiomer of Yongshi	
LL37	LLGDFFRKSKEKIGKEFKRIVQRIKDFLRNLVPRTES	*Homo sapiens*	NP_004336.4
OVA (257-264)	SIINFEKL		AUD54707.1
SARS-CoV-2 HR2	DISGINASVVNIQKEIDRLNEVAKNLNESLIDLQEL		P0DTC2
SARS-CoV-1 HR1	Biotin-ANQFNKAISQIQESLTTTSTALGKLQDVVNQNAQALNTLVKQ		P59594
SARS-CoV-2 HR1	Biotin-ANQFNSAIGKIQDSLSSTASALGKLQDVVNQNAQALNTLVKQ		P0DTC2
MERS-CoV HR1	Biotin-ANKFNQALGAMQTGFTTTNEAFQKVQDAVNNNAQALSKLASE		AXP07345.1
PT	KRFKKFFMKLKKSVKKRVMKFFKKPMVIGVTFPF	*Pseudonaja textilis*	U5KJJ1.1
PC1	KRRKFFRSIRKRIKKLRKSIKKRLKKLPFEVPLVFSIPF	*Phascolarctos cinerus*	XP_020854988.1
PC 1a	RKRIKKLRKSIKKRLKKLPFEVPLVFSIPF	Truncation of PC1	

CDC	KRFKKFFKKVKKSVKKRLKKIFKKPMVIGVSIPF	*Crotalus durissus cascavella*	AGS36137.1
NS	KRFKNFFKKIKTGIKKVIKKTKE	*Notechis scutatus*	XP_026545399.1
PB	KQPKRVKRFKKFFRKIKKGFRKIFKKTKIFIGGTIPI	*Python bivittatus*	XP_007443270.1
TS	KRFKKFFKKIKKSVKKRVKKLFKKPRVIPISIPF	*Thamnophis sirtalis*	XP_013912467.1
Pangolin 1	RTKRFRKLGNLLQKGGQKIGQKIERIGQKIKDFFSNLVPRQEGA	*Manis javanica*	XP_017524805.2
Pangolin 1a	NLLQKGGQKIGQKIERIGQKIKDFFSNLVPRQEGA	Truncation of Pangolin 1	
Pangolin 1b	KIERIGQKIKDFFSNLVPRQEGA	Truncation of Pangolin 1	
Pangolin 1c	RTKRFRKLGNLLQK	Truncation of Pangolin 1	
Bat Cathelicidin 2	VRRKETRAWRLPAPIGLWAPPGDGPAEPDPPVHGL	*Myotis lucifugus*	G1PZ56
Bat Cathelicidin 2a	VRRKETRAWRLPAPIGLWAPPGDG	Truncation of Bat Cathelicidin 2	
Bat Cathelicidin 3	VRFNYDRLSNIIKRGGYKLGEGLEIVG	*Myotis lucifugus*	XP_006108362.1
Bat Cathelicidin 3a	VRFNYDRLSNIIKRGGYKLGEG	Truncation of Bat Cathelicidin 3	
Bat Cathelicidin 3b	VRFNYDRLSNIIKRGGYKL	Truncation of Bat Cathelicidin 3	
Bat Cathelicidin 4	IKNVELNIENLGERIKNAKKKVWEKIKSFGRRIKDFFRKPSPEVEP	*Myotis brandtii*	XP_014395994.1
Bat Cathelicidin 4a	VELNIENLGERIKNAKKKVWEKIKSFGRRIKDFFRKPSPEVEP	Truncation of Bat Cathelicidin 4	
Bat Cathelicidin 4b	VELNIENLGERIKNAKKKVWEKIKSFGRRIKDFFRK	Truncation of Bat Cathelicidin 4	

Bat Cathelicidin 4c	GERIKNAKKKVWEKIKSFGRRIKDFFRKPSPEVEP	Internal Deletion of Bat Cathelicidin 4	
Bat Cathelicidin 4d	GERIKNAKKKVWEKIKSFGRRIKDFFRK	Truncation of Bat Cathelicidin 4	
Bat Cathelicidin 4e	GERIKNAKKKVWEKIKSFGRR	Truncation of Bat Cathelicidin 4	
Bat Cathelicidin 4f	KNVELNIENLGERIKNAKKK	Truncation of Bat Cathelicidin 4	
Bat Cathelicidin 5	IDRSKLPPAVRDLYDNARNNIINNILRNF	*Myotis lucifugus*	XP_014306451.1
Bat Cathelicidin 5a	AVRDLYDNARNNIINNILRNF	Truncation of Bat Cathelicidin 5	
Bat Cathelicidin 9	GVPAQEPVRKAPPPPPDLQPQTPGPWPSPTWSPFPPPAQNKDFGFNSKR	*Myotis lucifugus*	G1Q810
Bat Cathelicidin 9a	PVRKAPPPPPDLQPQTPGPWPSPTWSPFPPPAQNKDFGFNSKR	Truncation of Bat Cathelicidin 9	
Bat Cathelicidin 9b	PVRKAPPPPPDLQPQTPGPWPSPTWSPFPPP	Truncation of Bat Cathelicidin 9	
Bat Cathelicidin 11a	ERQQEDSREQPTAPPPEEEAASDIDR	*Myotis brandtii*	XP_005867266.1
Bat Cathelicidin 13	VILGAENLGERIKNAKKKVWEKIKSFGRRIKEFFRKPSPEVEP	*Myotis davidii*	ELK24988.1
Bat Cathelicidin 13a	VILGAENLGERIKNAKKKVWEKIKSFGRRIK	Truncation of Bat Cathelicidin 13	

Cat 1	RKLGQLGELIQQGGQKIVEKIQKIGQRIRDFFSNLRPRQEA	*Felis catus*	NP_001191707.1
Cat 1a	KIVEKIQKIGQRIRDFFSNLRPRQEA	Truncation of Cat 1	
Cat 1b	KIGQRIRDFFSNLRPRQEA	Truncation of Cat 1	
Beluga 1	RRIPFWPIPLRWQWPPPWFPPSFPIPRISRKR	*Delphinapterus leucas*	XP_022428982.1
Beluga 1a	PPPWFPPSFPIPRISRKR	Truncation of Beluga 1	
Puma 1	LGQLGELIQRGGQKIGEKIQNIGQRIRDFFSNLRPMQEA	*Puma concolor*	XP_025772022.1
Puma 1a	KIQNIGQRIRDFFSNLRPMQEA	Truncation of Puma 1	

Supplemental Table 1. Sequence of peptides used in this study. Those with greater than 50% inhibition at 50μM appear in bold text.

| 25µM | 12.5µM | 6.25µM | 3.12µM | 1.56µM | 0.78µM | Control |
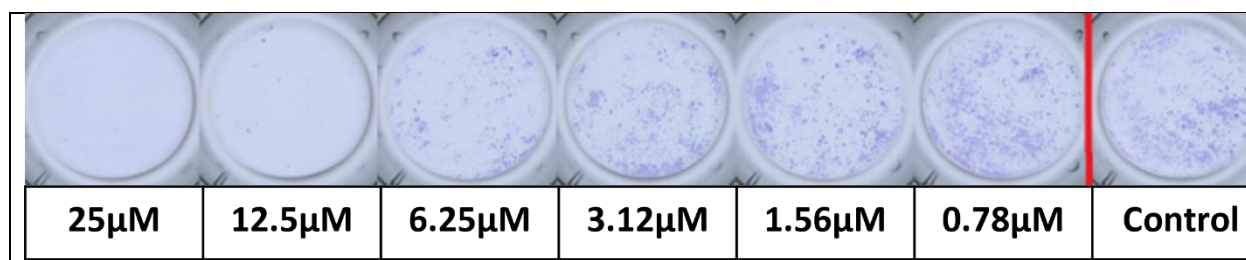
Supplemental Figure 1. Representative IHC Staining of Vero E6 hACE2 cells infected with SARS-CoV-2 and treated with pSer. pSer at the labeled concentrations was pre-incubated with 100 pfu of live SARS-CoV-2 virus (nCoV/USA_WA1/2020) for 1 hour at 37° C before addition to confluent Vero E6 hACE2 cells in a 96-well plate. Infected cells were fixed, permeabilized, and stained with anti-spike antibody.
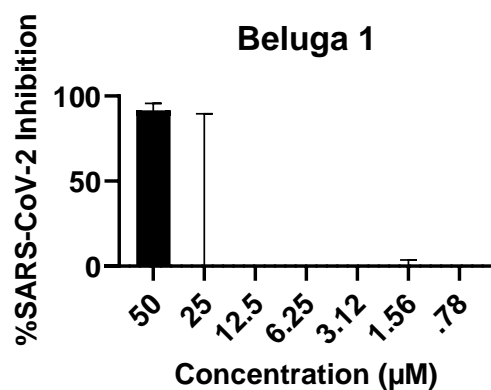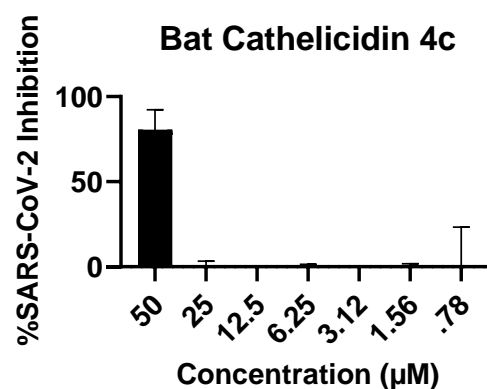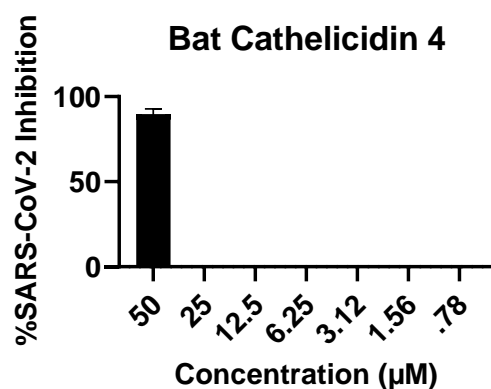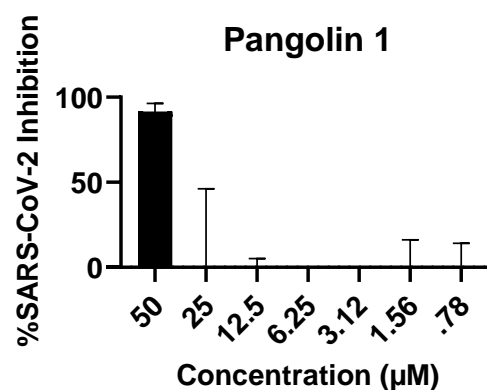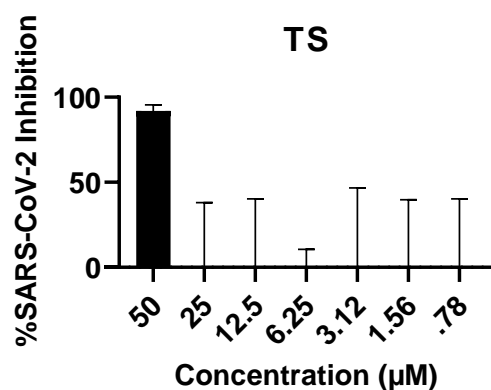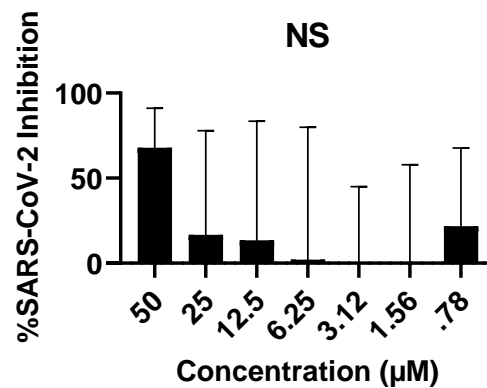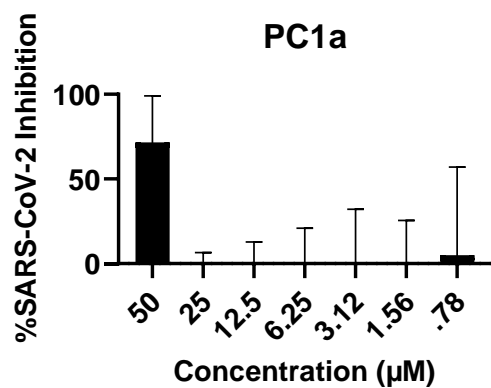
Supplemental Figure 2. Dose-response curves of other cathelicidin peptides with greater than 50% SARS-CoV-2 inhibition at 50μM. Inhibition of SARS-CoV-2 infection by various zoonotic cathelicidin peptides. Peptides at the labeled concentrations were pre-incubated with 100 pfu of live SARS-CoV-2 virus (nCoV/USA_WA1/2020) for 1 hour at 37° C before addition to confluent Vero E6 hACE2 cells in a 96-well plate. Infected cells were fixed and quantified by focus forming assay after 48 hours. Inhibition of viral infection was calculated based on the percent area of each well staining positively for viral spike protein compared to control wells without peptide inhibitor treatment. Results are representative of 3 independent experiments performed in triplicate.

Chapter 3: Atovaquone and pibrentasvir inhibit the SARS-CoV-2 endoribonuclease and restrict infection *in vitro* but not *in vivo*

Author List

Troy von Beck[1], Luis Mena Hernandez[1], Hongyi Zhou[2], Katharine Floyd[1], Mehul Suthar[1,3], Jeffrey Skolnick[2], Joshy Jacob[1,*].

Author List Footnotes

[1] Emory Vaccine Center, Yerkes National Primate Center, Emory University, 954 Gatewood Road Atlanta, GA 30329, USA
[2] Center for the Study of Systems Biology, School of Biological Sciences, Georgia Institute of Technology, 950 Atlantic Drive, NW, Atlanta, GA 30332, USA
[3] Department of Pediatrics, Division of Infectious Diseases, Emory University School of Medicine, Atlanta, GA 30322, USA

Summary

The emergence of SARS-CoV-1 in 2003, followed by MERS-CoV and now SARS-CoV-2 has proven the latent threat these viruses pose to humanity. While the SARS-CoV-2 pandemic has shifted to a stage of endemicity, the threat of new coronaviruses emerging from animal reservoirs remains. To address this issue, the global community must develop small molecule drugs targeting highly conserved structures in the coronavirus proteome. Here, we characterized existing drugs for their ability to inhibit the endoribonuclease activity of the SARS-CoV-2 non-structural protein 15 (nsp15) via *in silico, in vitro*, and *in vivo* techniques. We have identified nsp15 inhibition by the drugs pibrentasvir and atovaquone, of which the latter two effectively inhibit SARS-CoV-2 and HCoV-OC43 at low micromolar concentrations in cell culture. Further, atovaquone but not pibrentasvir is observed to modulate HCoV-OC43 dsRNA and infection in a manner consistent with nsp15 inhibition. Although neither pibrentasvir nor atovaquone

translate to clinical efficacy in a murine prophylaxis model of SARS-CoV-2 infection, atovaquone may

serve as a basis for the design of future nsp15 inhibitors.

Introduction

Severe acute respiratory syndrome coronavirus 2 (SARS-CoV-2), the causative agent of

coronavirus disease of 2019 (COVID-19) continues to spread globally and cause significant morbidity and

mortality among unvaccinated individuals and those with weakened immune systems [196]. Further,

control of the virus has been complicated by the expansion of novel variants possessing mutations that

enhance transmissibility and erode the protection provided by the original A.1 lineage-based vaccines,

convalescent plasma, and monoclonal therapies [145,173]. Contrary to the observed evolution of SARS-CoV-

2 antibody escape variants, susceptibility to the small molecule antiviral remdesivir has remained

consistent overtime, despite the sporadic appearance of remdesivir resistant viruses in hospitalized

patients [197,198]. This trend likely reflects the lack of selection for remdesivir resistant strains outside the

hospital environment and highlights the long-term value of identifying new small molecules targeting

conserved viral proteins.

To complement the antagonism of viral RNA synthesis and polypeptide processing by

remdesivir, molnupiravir, and ritonavir-boosted nirmatrelvir (Paxlovid), we focused on identifying

inhibitors of the viral endoribonuclease encoded by non-structural protein 15 (nsp15). This protein is

conserved among all mammalian coronaviruses and functions to regulate the accumulation and

localization of viral double-stranded RNA (dsRNA). Nsp15 cleaves RNA at unpaired pyrimidine bases,

with a strong preference for uridine over cytidine [102,106,199]. This nuclease activity functions to limit

cytosolic dsRNA and thereby antagonize intracellular pattern recognition receptors (PRRs) specific for

dsRNA and 5' poly(U) sequences, including MDA5, PKR, and OAS/RNase L [68,105,200]. Deficiency for nsp15

has been linked to reduced viral fitness across multiple coronaviruses including SARS-CoV-1, human

coronavirus 229E (HCoV-229E), infectious bronchitis virus (IBV), mouse hepatitis virus (MHV), and porcine epidemic diarrhea virus (PEDV) [66,68,105,200-202]. In those studies, the loss of viral fitness correlated with the early induction of a type I interferon response and the rapid apoptosis of infected cells. Further, in the context of MHV, knockout mutations in nsp15 were not found to increase total cellular dsRNA content but did result in a greater proportion of "free" dsRNA foci not sequestered in the replication complex associated double-membraned vesicles (DMVs) [68]. The conserved dependence of SARS-CoV-1 and other distantly related coronaviruses on nsp15 for immune evasion strongly supports the existence of a similar dependence for SARS-CoV-2.

Due to the pressing need for SARS-CoV-2 antiviral therapeutics, there is a heightened interested in repurposing drugs approved by the United States Food and Drug Administration (USFDA) for the treatment of COVID-19 patients. This approach can accelerate the drug discovery pipeline by limiting the selection of potential therapeutics to those with known safety and tolerability profiles [203]. Additionally, *in silico* analyses using algorithms like AutoDock, Dockthor, GOLD, or FRAGSITE can stratify the candidates for drug repurposing based on the strength of modeled interactions with a target protein [204-206].

In the following experiments, we applied the newly updated FRAGSITE2 virtual ligand screening algorithm to rank potential SARS-CoV-2 nsp15 inhibitors from the DrugBank compound library [207]. Top ranked drugs were screened for inhibition of recombinant nsp15 enzymatic activity and inhibition of SARS-CoV-2 and HCoV-OC43 infection in cell culture. This yielded two candidate drugs, pibrentasvir (predicted by FRAGSITE2) and atovaquone (predicted by other *in silico* methods), which were MAVS dependent and acted early during viral infection. However, in a murine infection model with live SARS-CoV-2 virus, we found that neither atovaquone nor pibrentasvir were able to reduce viral replication or

symptomatic weight loss; while the origin of this difference in response is unclear, it might reflect problems with bioavailability.

Methods

In Silico Screening of FDA Approved Drugs for Nsp15 Binding Activity

Given the amino acid sequence of SARS-CoV-2 nsp15, FRAGSITE2 predicts its three-dimension (3D) structure using our previously developed method TASSER [208]. This method produced a structure with no major deviations from the experimentally determined protein data bank (PDB) 6VWW crystal structure of nsp15 (TM-score 0.90) and performed well in our methodology. The 3D structure of a single nsp15 monomer was then compared to a library of experimentally determined protein-ligand binding pockets from the PDB [209]. The top list of matched pockets is used to derive a profile representing the target pocket, which is then combined with the ligand profiles of the screened compound library to form a feature vector. We then utilized boosted tree regression machine learning method to train a model on the DUD-E benchmarking set [210]. This model was then used to make new predictions by screening on the DrugBank database [211].

Growth and Purification of Recombinant SARS-CoV-2 Nsp15

To produce recombinant nsp15 for *in vitro* screening assays, a vector encoding the SARS-CoV-2 nsp15 with a c-terminal twin strep tag (Addgene, Catalog#:141381) was transfected into HEK293T cells using the transporter 5 PEI transfection reagent (Polysciences, Catalog#: 26008-5). 72 hours post-transfection, adherent cells were collected by mechanical scraping, washed once in 1X PBS, and lysed in ice-cold 1X PBS containing 1% NP-40 and a 1X concentration of Halt protease inhibitor cocktail (Thermo Fisher Scientific, Catalog#: 78429). Recombinant nsp15 was column purified by strep-tag affinity (Zymo

Research, Catalog#: P2004). Purified nsp15 in Strep-Elution Buffer (Zymo Research, Catalog#: P2004-3-30) was diluted 1:1 with 100% glycerol and stored at -20° C until use. Proper assembly of recombinant nsp15 into homohexamers was confirmed by western blot following native polyacrylamide gel electrophoresis (Supplemental Figure 1). For western blot, recombinant nsp15 was detected by polyclonal rabbit anti-Strep II tag antibody (Abnova, Catalog#: PAB16601) and anti-rabbit Ig HRP conjugated secondary antibody (SouthernBiotech , Catalog#: 4030-05). In subsequent experiments, SARS-CoV-2 nsp15 bearing an N-terminal 6x-his tag was purchased from a commercial supplier (Novus Biologicals, Catalog#: NBP3-07082) and stored frozen in PBS without the addition of 50% glycerol.

Library Screening for SARS-CoV-2 Nsp15 Inhibitory Activity

The direct inhibition SARS-CoV-2 nsp15 nuclease activity by each inhibitor was measured *in vitro* using recombinant strep-tagged or his-tagged nsp15 and a 5'-FAM-dA-rU-dA-dA-TAMRA-3' FRET probe as previously described [111]. Briefly, purified SARS-CoV-2 nsp15 was added to a concentration of 30nM in NendoU buffer (100mM NaCl, 20mM HEPES, pH 7.8) supplemented with 5mM McCl$_2$, 0.5µM FRET probe, and inhibitor at the specified concentration on ice. For experiments with strep-tagged nsp15, FAM fluorescence was recorded at 1-minute intervals for 1 hour on a Bio-rad CFX 96 real-time qPCR thermocycler at 30° C using the SYBR channel. For experiments with his-tagged nsp15, FAM fluorescence was recorded at 1-minute intervals for 1 hour on a Roche LightCycler480 at 37° C using the SYBR channel. For analysis, the recorded fluorescence of each well after 10 minutes was normalized to the starting fluorescence and to a no-enzyme negative control well. Inhibition of nuclease activity was then calculated as the percent reduction in FAM fluorescence relative to no-inhibitor positive control wells.

Evaluation of Drug-induced Nsp15 Aggregation

N-terminally his-tagged nsp15 (Novus Biologicals, Catalog#: NBP3-07082) was diluted to 700nM in NendoU Buffer containing 5mM $MnCl_2$ with or without 100μM drug additive. Control and drug treated samples were then heated at 37°C for 10 minutes to simulate the nuclease assay reaction conditions. As a positive control, an additional preparation of control nsp15 without drug was heated to 95°C for 10 minutes to denature the protein and induce aggregation. Following incubation, NativePAGE sample buffer was added to a 1X concentration and the protein preparations were then separated on a 4-12% non-denaturing Bis-Tris polyacrylamide gel (Thermo Fisher Scientific, Catalog#: NP0323BOX) using light cathode buffer (Thermo Fisher Scientific, Catalog#: BN2002). Proteins were then transferred to a PVDF membrane and washed twice with methanol followed by blocking with TBST containing 5% w/v non-fat dry milk for 1 hour. Membranes were then stained with primary anti-6x-His tag antibody (Thermo Fisher Scientific, Catalog#: PA1-983B) diluted 1:1000 in TBST overnight. Membranes were then washed 3 times with TBST and stained with anti-rabbit Ig HRP conjugated secondary antibody (SouthernBiotech , Catalog#: 4030-05) diluted 1:10,000 in TBST for 2 hours. After 3 additional washes, protein bands were detected by chemiluminescence using SuperSignal West Femto Maximum Sensitivity Substrate (Thermo Fisher Scientific, Catalog#: 34094).

Cell Lines and Viruses

HEK293T cells were purchased from ATCC (ATCC, Catalog#: CRL-3216). A549 cells expressing human ACE2 and TMPRSS2 were purchased from InvivoGen (InvivoGen, Catalog#: a549-hace2tpsa). Wild-type A549 and A549 MAVS$^{-/-}$ were provided by the lab of Dr. Suthar. VeroE6-TMPRSS2 cells were kindly provided by Barney Graham (Vaccine Research Center, NIH, Bethesda, MD). All cell lines were

cultured in DMEM (Thermo Fisher Scientific, Catalog#: 12-614Q) with 10% heat inactivated fetal bovine serum (Gibco, Catalog#: A5256701), 2mM L-glutamine (Quality Biological, Catalog#: 118-084-721), and 1X concentrations of penicillin, streptomycin, and amphotericin (PSA) (Quality Biological, Catalog#:120-096-711).

The B.1.351 variant (GISAID: EPI_ISL_890360) was provided by Andy Pekosz of John Hopkins University, Baltimore, MD. Both SARS-CoV-2 B.1.351 and A.1 (nCoV/USA_WA1/2020) viral stocks were grown on VeroE6-TMPRSS2 cells, and viral titers were determined by plaque assays on VeroE6-TMPRSS2 cells. VeroE6-TMPRSS2 cells were cultured in complete DMEM with puromycin at 10 mg/ml (Gibco, catalog#: A11138-03). HCoV-OC43 (VR-1558) was obtained from ATCC and grown on A549 WT cells. HCoV-OC43 stocks were titered by focus forming assay.

Coronavirus Infection Inhibition Assay

For infection assays 96-well plates containing $2x10^4$ A549 hACE2 TMPRSS2 or A549 WT cells were used for the SARS-CoV-2 and HCoV-OC43 viruses respectively. Cells were plated and grown overnight in complete DMEM at 37° C and 5% CO_2 prior to infection with an MOI of 0.1 of SARS-CoV-2 or HCoV-OC43 in 50µL of unsupplemented DMEM. Cells were infected at either 37° C or 33° C for SARS-CoV-2 and HCoV-OC43 respectively. 2 hours after infection, 2X concentrations of each inhibitor diluted in DMEM with 2%FBS, 2X PSA, and 2X L-glutamine were added. Infected cells were then incubated for 48 hours at 5% CO_2 and 37° C or 24 hours at 5% CO_2 and 33° C for SARS-CoV-2 and HCoV-OC43 respectively. The reduced growth time and temperature for HCoV-OC43 was used to compensate for its faster growth time in A549 cells and preference for upper respiratory tract conditions.

Infected cells were quantified by focus forming assay. Briefly, infected cells were fixed with 2% paraformaldehyde and permeabilized by 1X PBS containing 0.1% saponin and 0.1% FBS. For SARS-CoV-2, viral spike protein was detected by a human isotype CR3022 antibody (Abcam, catalog#: ab273073) and goat anti-human Ig HRP conjugated secondary (SouthernBiotech, catalog#: 2045-05). For HCoV-OC43, viral nucleocapsid was detected by anti-HCoV-OC43 nucleocapsid mouse monoclonal antibody (Millipore-Sigma, catalog#: MAB9013) and a goat anti-mouse Ig HRP conjugated secondary (SouthernBiotech, catalog#: 1030-05). Plates were developed for 10 minutes by incubation with TruBlue Peroxidase Substrate (SeraCare, catalog #50-78-02). Images were collected on an Immunospot CTL instrument and analyzed by an in-house script to quantify the area of infection. Plotted results represent the percent of area of the cell monolayer infected relative to control wells.

Cell Viability Assay

2×10^4 A549 WT cells were plated and grown overnight in complete DMEM at 37° C and 5% CO2 prior to the replacement of media with inhibitors diluted in 100µL of 1% FBS containing DMEM with 1X PSA and 1X L-glutamine. Cells were incubated at 33° C for 24 hours before the addition of 20µL of CellTiter 96-Aqueous One (Promega, Catalog#: PAG3580). Cells were then incubated at 33° C for 1 hour, followed by measurement of the absorbance at 450nm.

Flow cytometry of HCoV-OC43 infected cells

Confluent monolayers of A549 WT cells seeded in 12-well plates were infected with HCoV-OC43 at an MOI of 0.1 prior to the addition of inhibitors, FBS, L-glut, and PSA as in the focus forming assay. At 12 hours post-infection, cells were washed once with 1X PBS (retained in case of non-adherent cells) and

adherent cells were released by trypsinization. The adherent and non-adherent cell fractions were combined, pelleted, and resuspended in BD Cytofix/Cytoperm (BD Biosciences, Catalog#:554722). Cells were fixed and permeabilized for 20 minutes on ice followed by two washes with BD Perm/Wash buffer (BD Biosciences, catalog#: 554723). Cells were then stained with mouse anti-HCoV OC43 N protein (Millipore-Sigma, catalog#: MAB9013) diluted 1:200 in perm/wash buffer for 30 minutes at room temperature. Cells were washed twice with perm/wash buffer and then stained with FITC conjugated goat anti-mouse Fab (SouthernBiotech, catalog#: 1015-02) diluted 1:1000 in perm/wash buffer. Cells were washed twice in 1X PBS containing 1% FBS and analyzed on a BD FACS Aria II flow cytometer using the FITC channel.

Immunohistochemistry of Viral dsRNA in HCoV-OC43 Infected Cells

A549 MAVS$^{-/-}$ cells were seeded one day prior to infection on glass coverslips in complete DMEM media. Cells were then infected with HCoV-OC43 at an MOI of 1 for 2 hours in unsupplemented DMEM prior to the addition of inhibitors, FBS, L-glut, and PSA as in the focus forming assay. 24 hours later, cells were fixed in 4% paraformaldehyde in 1X PBS for 10 minutes and then permeabilized in immunofluorescence perm/wash buffer containing 1X PBS, 0.5% saponin, 0.1% BSA, 5% normal goat serum, and 5% normal donkey serum. Cells were stained with mouse anti-OC43 N protein (Millipore-Sigma, catalog#: MAB9013) and rabbit anti-dsRNA clone J2 (AbsoluteAntibody, catalog#: Ab01299-23.0) each diluted 1:50 in IF perm/wash buffer overnight at 4° C. Unbound antibody was removed by washing in perm/wash buffer. Cells were then stained with secondary antibodies PE conjugated donkey anti-rabbit Ig (BioLegend, catalog# 406421) and AF488 conjugated goat anti-mouse Ig (LifeTechnologies, Catalog#: A11001) diluted 1:300 in perm/wash buffer for 1 hour at 37° C. Again unbound antibody was removed by washing in perm/wash buffer and excess saponin was then washed out with 1X PBS. Cell

nuclei were then stained with Hoescht 33342 (Thermo Fisher Scientific, Catalog#: 62249) diluted 1:80 in

1X PBS for 10 minutes at 37° C. Excess Hoescht 33342 was removed by washing in 1X PBS before

mounting the coverslips to a glass slide with 100% glycerol. Slides were kept away from light and imaged

on a fluorescence microscope within 3 hours of mounting.

Infection of mice with SARS-CoV-2 B.1.351

C57BL/6J mice were purchased from Jackson Laboratories. All mice used in these experiments

were females 8 weeks of age. Stock B.1.351 virus was diluted in 0.9% Normal Saline, USP (MedLine,

catalog#: RDI30296;). Mice were dosed with either 40mg/kg of atovaquone or 24mg/kg of pibrentasvir

via daily intraperitoneal (i.p.) injections for 4 days beginning one day prior to infection. Mice were

anesthetized with isoflurane and infected intranasally with virus (50 µl; 1×106 PFU/mouse) in an animal

biosafety level 3 (ABSL-3) facility. Mice were monitored daily for weight loss. All experiments adhered to

the guidelines approved by the Emory University Institutional Animal Care and Use Committee.

Quantitative reverse transcription-PCR of lung tissues

At three days post-infection, mice were euthanized with an isoflurane overdose. One lobe of

lung tissue was collected in an Omni Bead Ruptor tube filled with Tripure Isolation Reagent (Roche,

catalog#: 11667165001). Tissue was homogenized using an Omni Bead Ruptor 24 instrument (5.15 ms,

15 s) and then centrifuged to remove debris. RNA was extracted using a Direct-zol RNA Miniprep Kit

(Zymo Research, catalog#: R2051) and then converted to cDNA using a high-capacity reverse

transcriptase cDNA kit (Thermo Fisher Scientific, catalog#: 4368813). To quantify RNA, IDT Prime Time

gene expression master mix and were used with SARS-CoV-2 RDRP- and subgenomic-specific TaqMan

gene expression primer/probe sets as previously described [212,213]. All qPCRs were performed in 384-well

plates and run on a QuantStudio5 qPCR system.

Results

Predicted Nsp15 Binding Drugs Inhibit Nuclease Activity in vitro

To identify drugs with the potential for nsp15 binding and inhibitory activity, we first performed

an *in silico* screen of compounds contained in the DrugBank database using our recently developed

FRAGSITE2 methodology. After manual review of the predicted compounds to remove those not

approved for human use by the USFDA, we compiled a small list of highly ranked drugs (Table 1). These

drugs were predicted to interact with one of two binding pockets on the N-terminal oligomerization

domain of nsp15. Oritavancin was the top hit predicted for binding pocket 1 which comprises the main

interface between opposing monomers of nsp15 in the hexameric assembly (Figure 1A, Supplemental

Figure 2A). Rifamixin was the top hit for binding pocket 2, which is composed of residues from both the

N-terminal oligomerization domain and the middle-domain of nsp15 (Figure 1B, Supplemental Figure

2B). Both rifamixin, rifapentine, and everolimus are predicted to bind the same pocket, although

rifamixin also has a predicted interaction with a valine residue in position 31. Beyond our own

predictions, we also selected several compounds predicted by previous nsp15 docking studies to bind

the catalytic site, which included atovaquone, paritaprevir, glisoxepide, and idarubicin (Table 2) [214,215].

To validate our *in silico* predictions, we produced recombinant nsp15 bearing a C-terminal twin

strep II epitope tag (Supplemental Figure 1) and confirmed its cleavage of a small fluorescent RNA probe

in vitro and sensitivity to inhibition by the known RNase inhibitor benzopurpurin (Figure 2A) [110]. The *in*

silico predicted drugs were then screened using the same nuclease assay for their ability to inhibit cleavage at a concentration of 100μM (Figure 2B). As expected, benzopurpurin effectively prevented substrate RNA cleavage, as did idarubicin, pibrentasvir, and atovaquone. Conversely, cyanocobalamin, desmopressin, rifamixin, and rifapentine strongly suppressed the fluorescent signal generated by substrate cleavage and could not be evaluated by this assay. Similarly, oritavancin was found to non-specifically induce the formation of insoluble aggregates of nsp15 and therefore was not a true inhibitor (Supplemental Figure 3). In subsequent experiments we also evaluated the ability of the top performing drugs benzopurpurin, pibrentasvir, atovaquone, and idarubicin to inhibit a commercially sourced SARS-CoV-2 nsp15 bearing an N-terminal his-tag tested at a physiological 37°C (Figure 2B). Overall the results were in agreement with the previous assay, although the reported inhibitory activity was reduced for each drug. Using the his-tagged nsp15, a dose-response experiment was also performed to evaluate the activity of each drug when serially diluted down to a concentration of 5μM (Figure 2C).

Nsp15 Inhibitors Restrict SARS-CoV-2 Infection in vitro

Candidate drugs benzopurpurin, pibrentasvir, atovaquone, and idarubicin were further investigated for their ability to restrict SARS-CoV-2 infection of A549 alveolar epithelial cells overexpressing the human ACE2 receptor and TMPRSS2 protease (A549 hAT) (Figure 3A). Consistent with previous investigations of SARS-CoV-1, benzopurpurin was incapable of restricting SARS-CoV-2 infection of A549 hAT2 cells [110]. By comparison, atovaquone effectively inhibited infection with an EC50 of 2.46μM and pibrentasvir inhibited greater than 90% of infection even at the lowest concentration of 0.625μM. Neither drug was observed to alter the cellular morphology or metabolic activity (Supplemental Figure 4). Idarubicin is a genotoxic chemotherapy and could not be evaluated in culture due to high cytotoxicity even at the lowest concentration of 0.625μM. The results of our screen are

corroborated by previous reports of these drugs' *in vitro* efficacy. Pibrentasvir has been demonstrated

to inhibit the nsp14/nsp10 exonuclease of SARS-CoV-2 and restrict infection of Calu-3 cells with a

reported EC50 of 0.7μM [216]. Similarly, atovaquone has a reported EC50 of 1.5μM in VeroE6 cells, 2.7μM

in VeroE6 cells expressing hTMPRSS2, and 6.8μM in Huh7.5 cells, but a markedly increased EC50 of

29.7μM in Calu-3 cells [217,218].

Notably, atovaquone and pibrentasvir have differential effects on SARS-CoV-2 focus formation

(Figure 3B). Compared to untreated cells, both atovaquone and pibrentasvir limit the cell to cell

spreading of SARS-CoV-2 as indicated by the reduced size and frequency of distinct foci. Foci in

atovaquone treated cells stain for spike protein with similar intensity to untreated cells, however the

foci in pibrentasvir treated cells stain more faintly. This may indicate that in addition to preventing cell

to cell spread, pibrentasvir disrupts earlier steps in viral replication leading to reduced spike protein

production. This observation agrees with the earlier described mechanism of nsp14/nsp10 exonuclease

inhibition [216]. The proposed action of pibrentasvir and atovaquone on targets besides nsp15 is further

supported by the high antiviral effect at concentrations where no nsp15 inhibition is observed in the

fluorescence assay. These suggest that while inhibition of nsp15 may augment the antiviral effect for

each drug, it is unlikely to be the dominating mechanism for either.

Nsp15 Inhibitors Restrict HCoV-OC43 Infection in vitro

As nsp15 is highly conserved among all mammalian coronaviruses, we sought to determine

whether the inhibitory action of pibrentasvir and atovaquone would also be conserved against a related

mild coronavirus, hCoV-OC43. As hCoV-OC43 does not depend on ACE2 for cellular entry, infections

were performed in wild-type A549 cells and detected by staining with anti-OC43 N protein monoclonal

antibody. Both pibrentasvir and atovaquone inhibited hCoV-OC43 infection *in vitro* (Figure 4A). Further, this inhibition could be detected by flow cytometry as early as 12 hours post-infection (Supplemental Figure 5). While pibrentasvir inhibited hCoV-OC43 to a similar extent as SARS-CoV-2, atovaquone had a reduced peak inhibition at higher concentrations but remained active at lower concentrations compared to SARS-CoV-2.

After confirming both drugs remained active against hCoV-OC43, we further examined whether they would lose inhibitory activity in a MAVS knockout cell line. Since, MAVS acts as a downstream signaling intermediary of the two cytosolic dsRNA sensors MDA5 and RIG-I, compounds which inhibit viral infection via nsp15 should be MAVS dependent. Indeed, pibrentasvir and atovaquone experienced moderate and severe reductions in inhibitory activity respectively (Figure 4A). The more modest reduction in inhibition for pibrentasvir suggests that this drug is only partially dependent on nsp15 and is governed by other mechanisms such as the previously discussed exonuclease inhibition [216]. As atovaquone lost inhibitory activity in MAVS$^{-/-}$ A549 cells, we hypothesized that atovaquone may alter the localization or accumulation of viral dsRNA. Previously, Deng et al. reported that an nsp15 deficient variant of MHV possessed normal amounts of dsRNA but altered localization, with an increase in cytosolic dsRNA not associated with replication transcription complexes [68]. We therefore investigated by immunofluorescence the localization of dsRNA in MAVS$^{-/-}$ A549 cells with and without inhibitor treatment (Figure 4B-C). dsRNA staining was specific to HCoV-OC43 infected cells with enrichment of dsRNA foci in the perinuclear space typical of coronaviruses. Notably, atovaquone treated cells displayed a greater number of distinct dsRNA foci per cell that spread throughout the cytoplasm, while pibrentasvir treated cells were not significantly altered in dsRNA content.

Again, both pibrentasvir and atovaquone remain active against HCoV-OC43 at concentrations below their observed inhibition of nsp15 in the fluorescence assay. While it is possible these drugs may bind

more tightly to the nsp15 of HCoV-OC43 than SARS-CoV-2, it is more likely that additional targets are present which together produce the antiviral effect. However, the effect of atovaquone does appear restricted to the sensing of dsRNA and further involves the localization of dsRNA. It is therefore plausible that in addition to nsp15 inhibition, atovaquone is further augmenting the activation of cytosolic dsRNA sensors or potentially disrupting the formation of DMVs responsible for sequestering viral dsRNA.

Atovaquone and Pibrentasvir Are Not Protective in a Mouse Model of SARS-CoV-2 Infection

Following the *in vitro* characterization of atovaquone and pibrentasvir, we further examined whether either drug could limit SARS-CoV-2 infection in mice using a prophylaxis treatment regimen (Figure 5A). C57BL/6 mice were dosed with either 40mg/kg of atovaquone or 24mg/kg of pibrentasvir via daily intraperitoneal (i.p.) injections beginning one day prior to infection with 1×10^6 pfu of SARS-CoV-2 B.1.351 delivered intranasally. The dosing regimens were designed following guidance of previous pharmacokinetic and antiviral studies of atovaquone and pibrentasvir in murine models [217,219-221]. Mice were monitored for weight loss daily beginning on day 0 until euthanasia at the peak of infection of on day 3. RNA was extracted from the lung tissue and turbinates of each mouse to quantitate the extent of viral replication by RT-qPCR.

Despite the observed *in vitro* inhibition of SARS-CoV-2 infection, neither atovaquone nor pibrentasvir was protective in the *in vivo* model. Although both RNA-dependent RNA polymerase (RdRp) and subgenomic (Sg) viral transcripts trended lower in the pibrentasvir and atovaquone treated groups, this effect was not statistically significant in either the lung or nasal turbinate tissues (Figure 5B-E). Moreover, there was no therapeutic effect, as treated and control mice had nearly identical weight loss on day 3 post-infection (Figure 5F).

Discussion

Here we report the discovery of nascent nsp15 inhibitory activity present in several drugs approved for human use by the USFDA for the treatment of conditions unrelated to SARS-CoV-2. These include: idarubicin, an anthracycline inhibitor of DNA topoisomerase II used in the treatment of leukemia; pibrentasvir, an inhibitor of the hepatitis C virus nonstructural protein 5A; and atovaquone, an antimicrobial drug used in the treatment of several fungal and parasitic infections. While these drugs were not protective in our mouse model system, it remains possible that an alternative formulation, dosage, or delivery method, such as direct application of the compound to airways via a nebulizer could produce improved *in vivo* protection. The identification of these compounds and their *in vitro* characterization may serve as a basis for the future design of novel nsp15 inhibitors based on chemical modification of the afore-mentioned drugs. Further, the success of FRAGSITE2 in identifying pibrentasvir as a high precision highly ranked hit exemplifies the potential for this tool in future drug discovery. One major advantage of FRAGSITE2 over the FINDSITE[comb2.0][222] and FRAGSITE[207] methods is that FRAGSITE2 does not use template ligands to derive the profile for the protein target, thus it can make predictions for ligands which do not have close homologous template ligands in the PDB. Compared to the FINDSITE[comb2.0] and FRAGSITE methods that depend on template ligands for deriving the target profile, FRAGSITE2 has comparable performance while having the potential to discover ligands that are remote from PDB, DrugBank and ChEMBL libraries [223].

Until recently, the repertoire of known nsp15 inhibitors was essentially limited to the generic RNase A inhibitors benzopurpurin B and Congo Red whose activity was originally characterized by Ortiz-Alcantara et al. in 2010 [110]. Since then, 5 publications have expanded this list to include Tipiracil [111],

NSC95397 [112], Exebryl-1 [113], epigallocatechin gallate [114], and betulonic acid derivatives [115]. Of these

compounds, only the betulonic acid derivatives show substantial inhibition (<10µM) of viral replication

in cell culture, however this effect was restricted to HCoV-229E and was not reproducible for SARS-CoV-

2, MHV-A59, or feline infectious peritonitis virus (FIPV) [115]. Our findings complement these earlier

studies and expand the repertoire of nsp15 inhibitors with *in vitro* efficacy. However, it should also be

noted that both atovaquone and pibrentasvir possess additional mechanisms of SARS-CoV-2 inhibition,

and it is unclear whether the interaction with nsp15 alone is sufficient to achieve their low micromolar

effective range [216,218].

While pibrentasvir has not previously received significant *in vivo* characterization for the

treatment of COVID-19, two prior studies have examined atovaquone. In the first of these studies,

Ahmed et al. performed a screen of predicted SARS-CoV-2 main protease inhibitors, which included

atovaquone. Although atovaquone only modestly inhibited the main protease activity at 50µM, it

successfully inhibited viral replication with an IC50 of 1.5µM in Vero E6 cells and 6.8µM in Huh7.5 cells.

However, atovaquone binds significantly to serum proteins in tissue culture medium and switching to a

serum free culture system further reduced the IC50 to just 20nM in WHO Vero cells. They further

determined the pharmacokinetics of atovaquone in a mouse model, showing an 18-38 hour half-life and

peak total plasma, total free plasma, and lung epithelial lining fluid concentrations of 273µM, 44nM, and

70nM respectively after 7 days of receiving 20mg/kg of atovaquone orally [217]. Although we did not

quantitate free plasma atovaquone in our dosing regimen, our regimen used double the daily dose and

was not limited by the low bioavailability of atovaquone achieved by oral dosing [224]. The second study

was a small randomized, double-blind, placebo-controlled trial to evaluate the efficacy of 1500mg of

oral atovaquone given twice daily to reduce the viral load over 10 days when first administered within

72 hours of hospitalization [225]. This dosing regimen follows similar guidelines in the treatment and

prevention of *Pneumocystis jiroveci* and *Pneumocystis carinii* pneumonia in adults, albeit the doses are doubled from 750mg to 1500mg twice per day. This provides an estimated daily dose in a similar range to our 40mg/kg regimen, although the oral route likely reduces the bioavailability compared to i.p. injection. Despite a similar dose to both our study and the study of Ahmed et al. the total plasma concentration of atovaquone in the clinical trial peaked at 31.6µM after 5 days of administration. Throughout the course of the clinical trial, atovaquone treatment was not found to significantly lower the viral load at any point during the 10 days of atovaquone treatment [225]. As a whole, these results reaffirm that even under the ideal conditions of prophylaxis and a high daily dose in our mouse model, atovaquone is ultimately ineffective at controlling SARS-CoV-2.

The experiments presented here provide some insight into the mechanism of action and *in vivo* potential of atovaquone and pibrentasvir but are ultimately limited in several regards. First, our *in vivo* study was based on dosing regimens previously used in pharmacokinetic studies or other disease models, but for which we have not determined exact serum or lung epithelial fluid concentrations according to our dosing regimen and delivery method. It may be that a full dose escalation study in mice could identify a higher "safe" threshold for atovaquone or pibrentasvir treatment that would produce an *in vivo* protective effect. Second, our *in vitro* studies are limited by a lack of established assays for confirming specific inhibition of nsp15 in the cellular context. To this end we have employed MAVS^{-/-} cells and immunofluorescence of viral dsRNA puncta to make inferences regarding the activity of atovaquone and pibrentasvir in cell culture, but ultimately lack a robust and high-throughput assay to specifically evaluate nsp15 activity during cellular infection. The field of nsp15 research would greatly benefit from the identification of a compound that robustly inhibits nsp15 in cell culture to act as a positive control and an assay which produces an easily quantifiable readout. This would allow

researchers to skip the *in vitro* screens with recombinant nsp15 and simultaneously avoid pursuing inhibitors which do not function in the cellular context.

To conclude, the studies presented here show the first evidence of SARS-CoV-2 nsp15 inhibition for idarubicin, atovaquone, and pibrentasvir. Further characterization of the specific binding interactions between each compound and nsp15 will allow for the determination of the minimal structural elements required for nsp15 inhibition. These future studies will also provide the opportunity to enhance nsp15 binding specificity via the subtraction, substitution, or addition of chemical moieties to the base compound. Finally, our *in vivo* experiments answer long-standing questions concerning the clinical utility of atovaquone and pibrentasvir in COVID-19 treatment that were raised by *in vitro* experiments in prior publications.

Figures
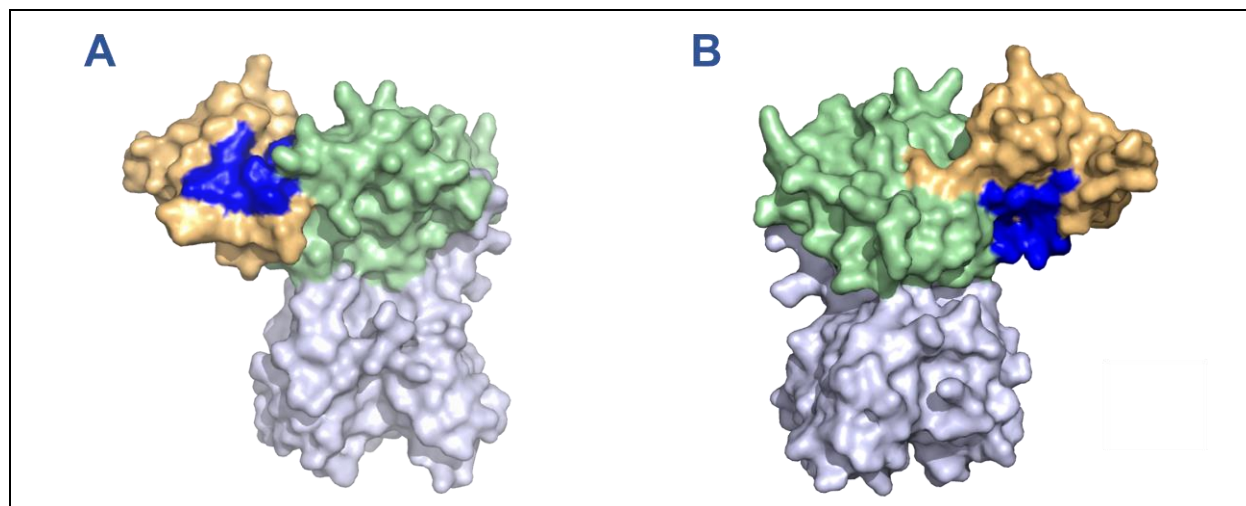
Figure 1. Binding pockets of 11 drugs on monomeric nsp15 predicted by in silico screening with FRAGSITE2 on monomeric nsp15. Binding pockets are highlighted in blue, while the oligomerization, middle, and catalytic domains are depicted in orange, green, and purple respectively. (A) Binding pocket 1, predicted for oritavancin, ledipasvir, posaconazole, micafungin, linaclotide, pibrentasvir, desmopressin, and cyanocobalamin. (B) Binding pocket 2, predicted for rifamixin, rifapentine, and everolimus. Depictions generated based on PDB structure 7N06.
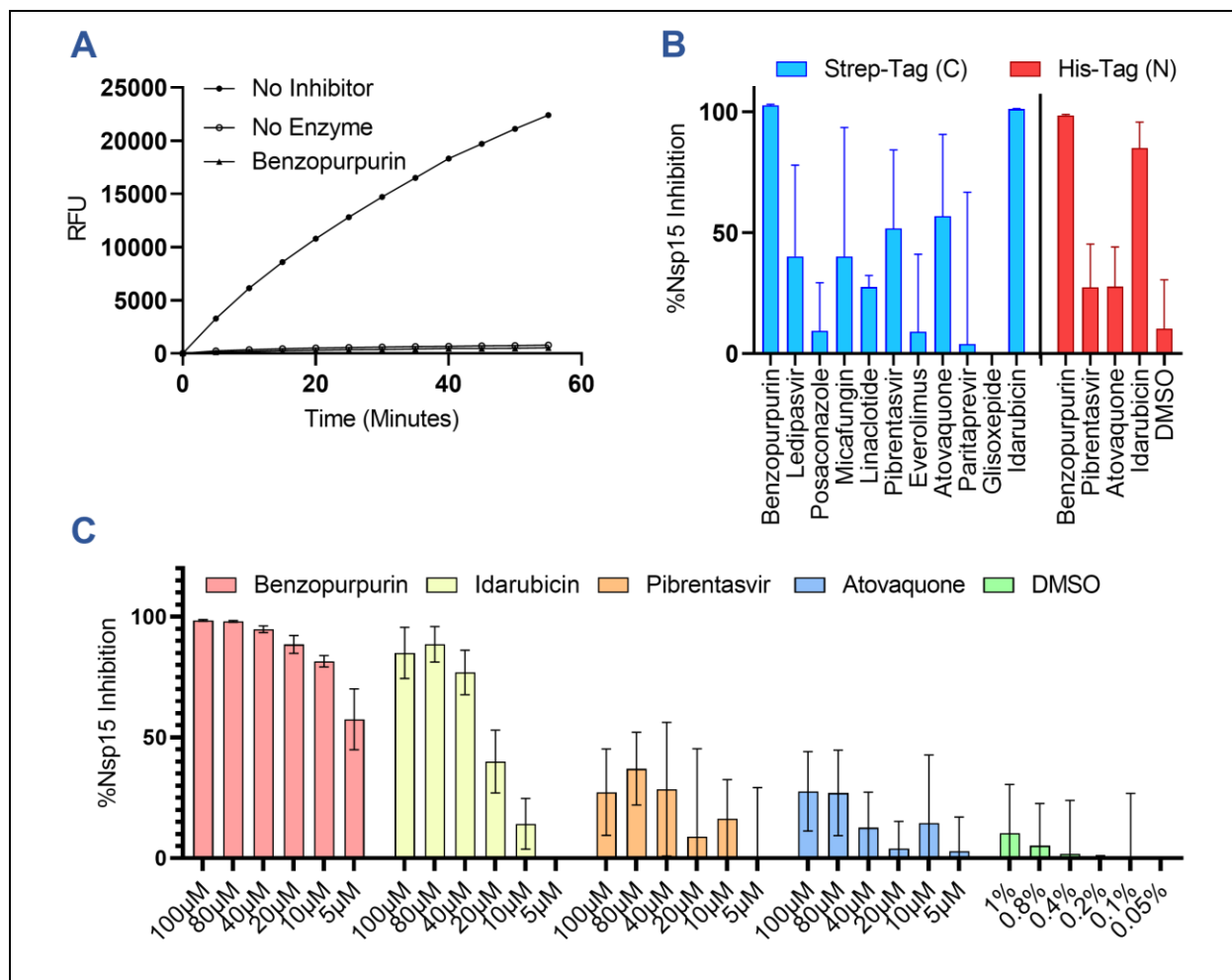
Figure 2. In vitro screening results of predicted inhibitors against nsp15 nuclease activity. (A) Representative results of a real-time nsp15 nuclease assay demonstrating cleavage of the FRET probe as measured by relative fluorescence units (RFU) and quenching of the nsp15 nuclease activity by addition of 100μM benzopurpurin. (B) Graph showing the percent inhibition of nsp15 nuclease activity by *in silico* predicted drugs at 100μM for C-terminally strep-tagged nsp15 incubated at 30°C or N-terminally his-tagged nsp15 incubated at 37°C. (C) Dose-response curves for nsp15 inhibition at the indicated drug concentrations with N-terminally his-tagged nsp15. At 100μM of drug the resulting solution contains 1% DMSO. Columns and error bars represent the average and standard deviation of 3 independent experiments.
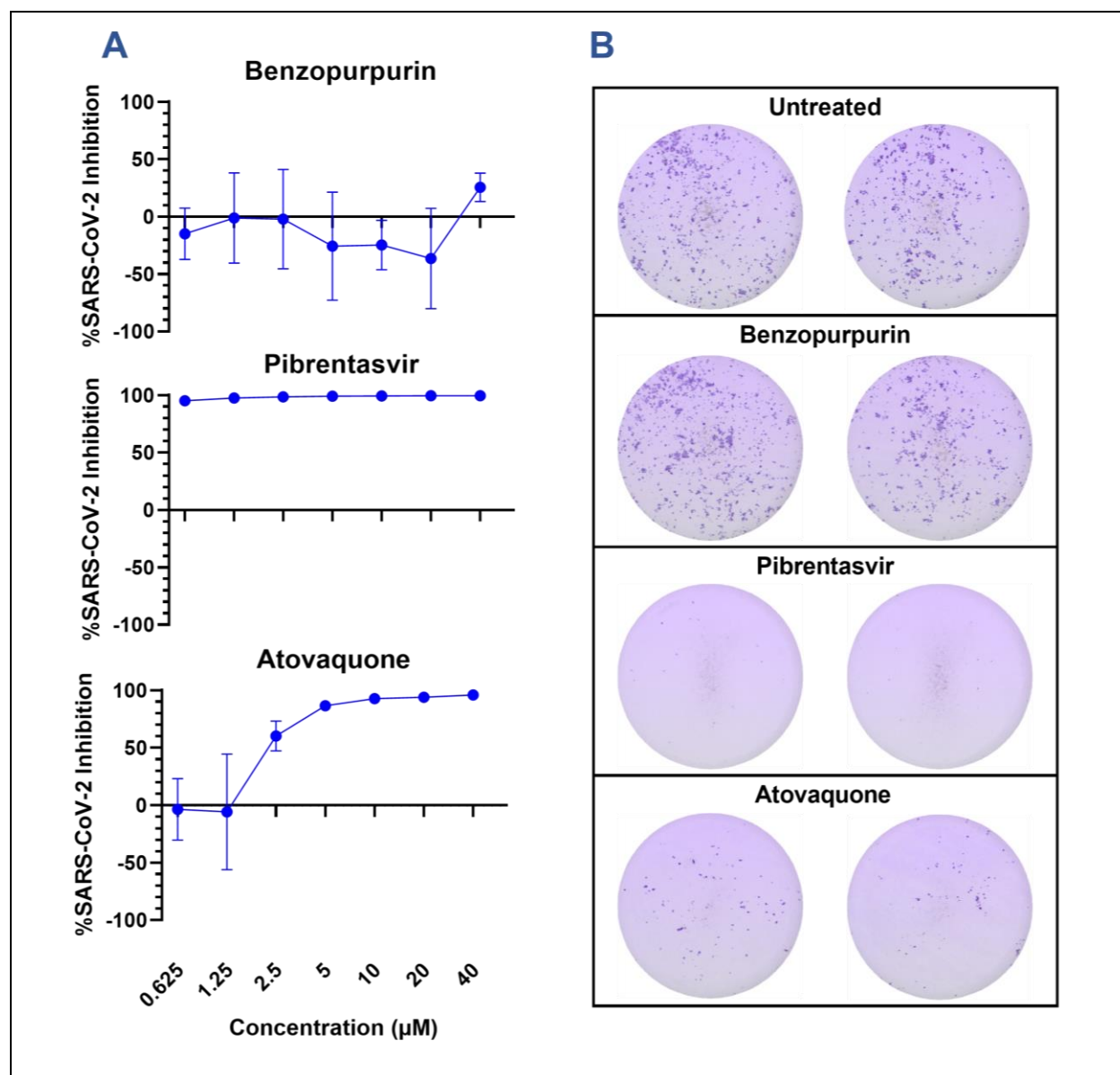
Figure 3. Inhibition of SARS-CoV-2 infection by in silico predicted inhibitors. (A) A549 hAT cells were infected with an MOI of 0.1 of SARS-CoV-2 A.1 (nCoV/USA_WA1/2020) for 2 hours before addition of select inhibitors at the indicated concentration. Foci were developed at 48 hours using cross-reactive anti-SARS-CoV-1 Spike antibody and viral inhibition calculated relative to the area of infection in control untreated samples. Graphs are representative of 2 experiments performed in triplicate. (B) Representative images from focus forming assays presented in 2A of samples treated with 10µM of the indicated drug.
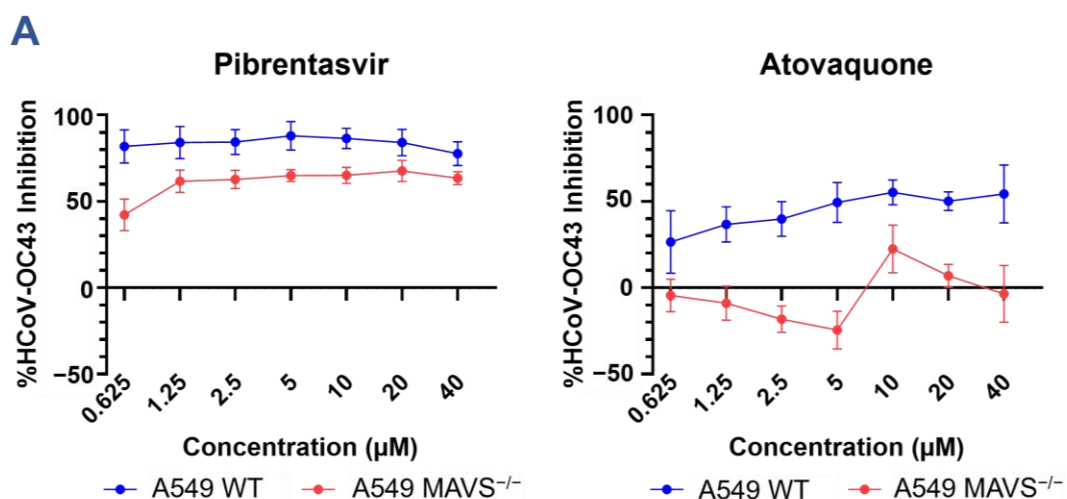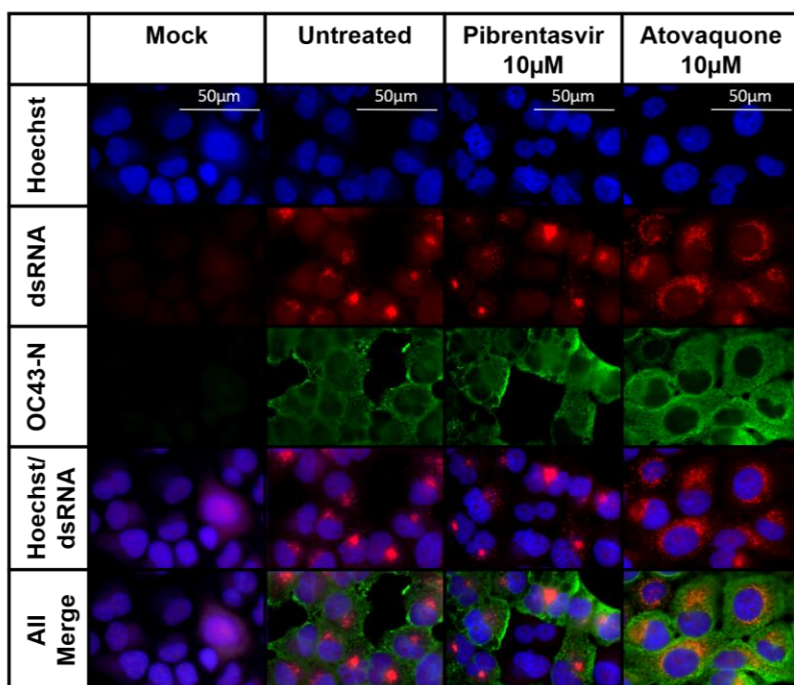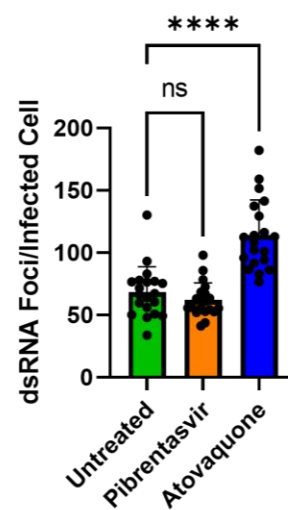
Figure 4. Inhibition of HCoV-OC43 infection by atovaquone and pibrentasvir. (A) A549 WT or A549 MAVS$^{-/-}$ cells were infected at an MOI of 0.1 of HCoV-OC43 for 2 hours before addition of select inhibitors at the indicated concentration. Foci were developed at 24 hours using anti-OC43 N protein antibody and viral inhibition calculated relative to the area of infection in control untreated samples. Graphs are representative of 2-3 experiments performed in triplicate. (B) Representative images of HCoV-OC43 infection following treatment with nsp15 inhibitors. A549 MAVS$^{-/-}$ cells coated on glass slides were infected with HCoV-OC43 at an MOI of 0.1. Nsp15 inhibitors were added to the indicated concentration 2 hours post-infection. Slides were fixed 24 hours post-infection, permeabilized, and stained for the presence of HCoV-OC43 N protein and viral dsRNA with monoclonal antibodies. (C) Graphical representation of the number of distinct dsRNA foci per infected cell in 3B. dsRNA foci were automatically counted in ImageJ version 1.53f51. The plot is representative of 20 random fields of view taken from 5 experiments, where each field of view is represented by a black dot. Results analyzed by One-Way ANOVA with multiple comparisons. p-values represented as ns = not significant, ****<.0001.
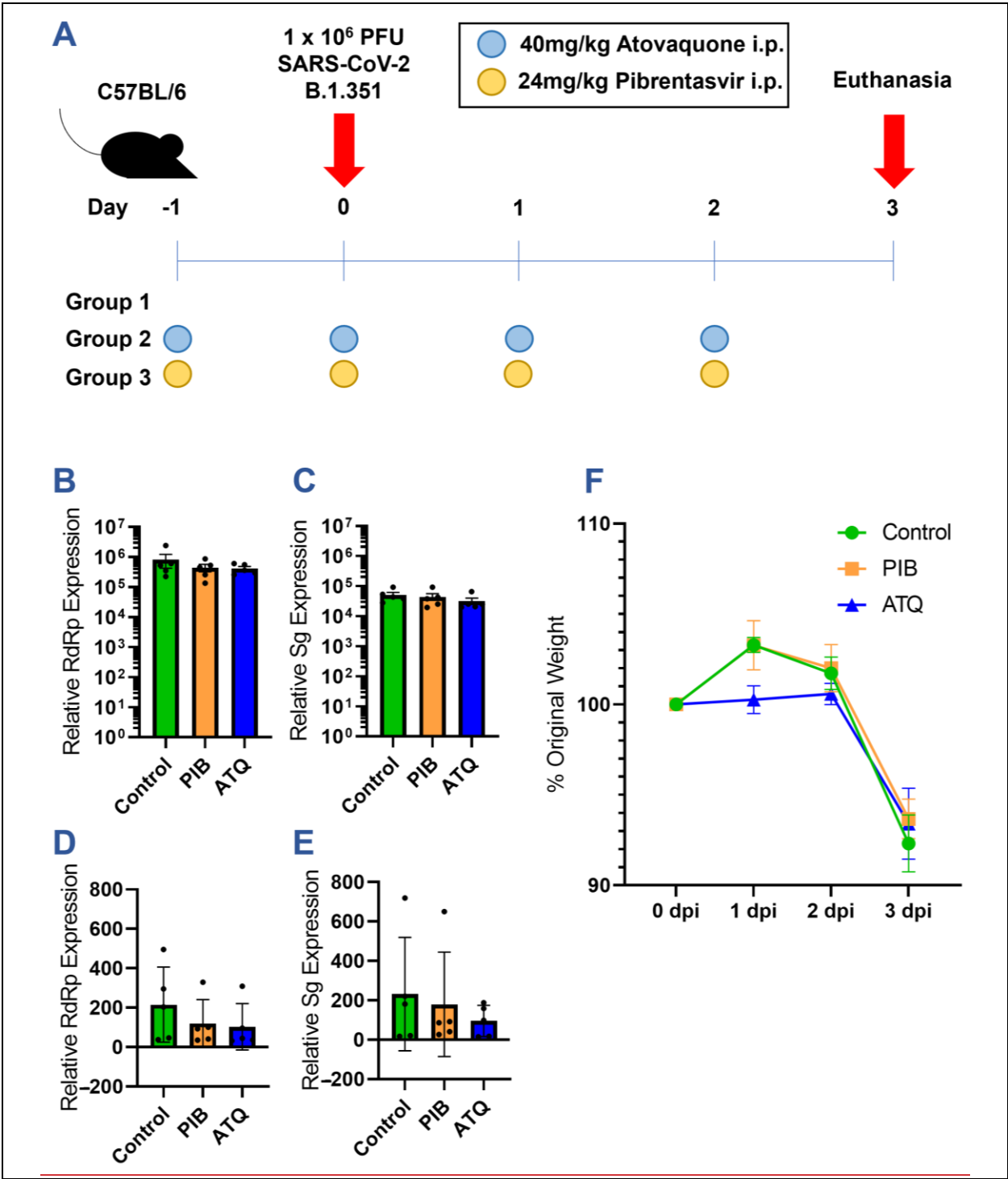
Figure 5. Efficacy of prophylactic atovaquone and pibrentasvir treatment in a mouse model of SARS-CoV-2 infection. (A) Diagram of mouse study. C57/BL6 mice were divided into 3 study groups with 5 mice per treatment regimen. (B-E) RT-qPCR quantitation of viral RNA copies in mouse lung and turbinate extracts. (B) Lung RdRp (C) Lung Sg (D) Turbinate RdRp (E) Turbinate Sg. Equal amounts of lung and turbinate cDNA from each mouse collected on day 3 was amplified with viral RdRp, viral subgenomic, and mouse GAPDH specific primer/probe sets. The concentration of viral RNA is normalized across samples to GAPDH and expressed relative to the background amplification in uninfected lung tissue and turbinate samples. Black dots indicate values for individual mice. (F) Weights of mice in each treatment group normalized to the day 0 weight.

Tables

Table 1. Ranking of FDA-approved drugs predicted by FRAGsite to bind nsp15 from SARS-CoV-2. Compounds are grouped by binding pocket 1 (orange) or binding pocket 2 (blue).

Drug Name	Score	Precision	Binding Site
Oritavancin	1.29	0.9	2LEU 26ILE 31VAL 50PRO 51VAL 52ASN 53VAL 55PHE 56GLU
Ledipasvir	1.10	0.9	
Posaconazole	1.06	0.9	
Micafungin	1.06	0.9	
Linaclotide	1.02	0.9	
Pibrentasvir	0.97	0.87	
Desmopressin	0.97	0.86	
Cyanocobalamin	0.93	0.83	
Rifamixin	0.99	0.88	31VAL 42LEU 43PHE 44GLU 46LYS 54ALA 55PHE 58TRP 59ALA 61ARG 86TRP 91ASP
Rifapentine	0.80	0.68	42LEU 43PHE 44GLU 46LYS 54ALA 55PHE 58TRP 59ALA 61ARG 86TRP 91ASP
Everolimus	0.77	0.65	

Table 2. Additional compounds predicted by other in silico studies to bind nsp15 from SARS-CoV2.

Drug Name	Binding Site	Reference
Atovaquone		214
Paritaprevir	Catalytic Pocket	214
Glisoxepide		215
Idarubicin		215

Supplemental Information
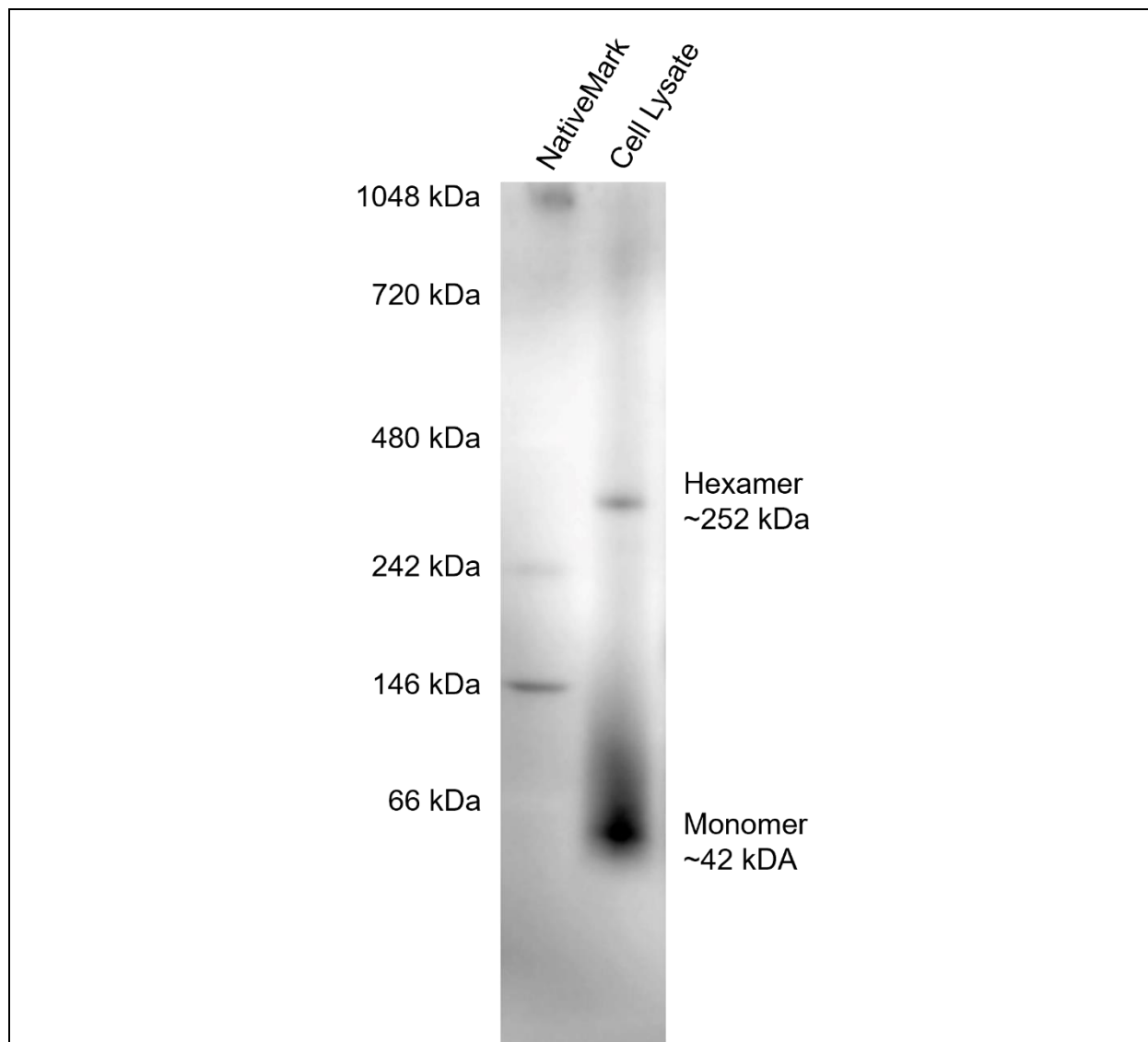
Supplemental Figure 1. Western blot analysis of HEK293T cells expressing strep-tagged nsp15 of SARS-CoV-2. HEK293T cells transfected with the pLVX-EF1alpha-SARS-CoV-2-nsp15-2xStrep-IRES-Puro were lysed in non-ionic detergent and separated under non-denaturing conditions. Protein bands specific to nsp15 and its hexameric oligomer were detected with polyclonal anti-Strep II tag antibody.
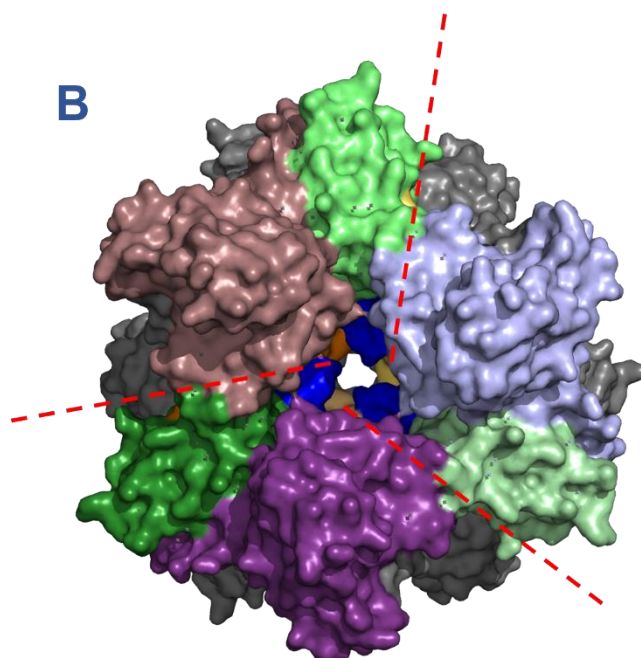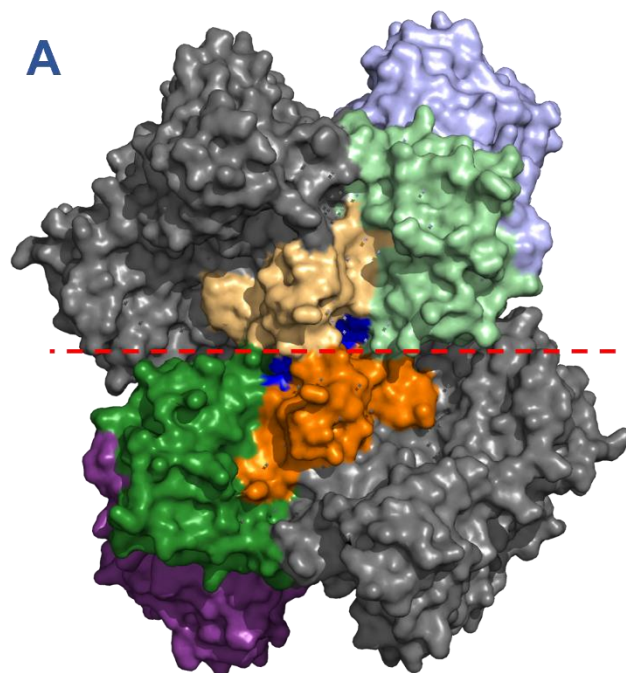
Supplemental Figure 2. Binding pockets of 11 drugs on hexameric nsp15 predicted by an in silico screening with FRAGSITE2. Binding pockets are highlighted in blue, while the oligomerization, middle, and catalytic domains are depicted in orange, green, and purple respectively. Domains from individual monomers forming a single interface appear in differing shades of the same base color, additional monomers appear in gray. (A) Binding pocket 1, predicted for oritavancin, ledipasvir, posaconazole, micafungin, linaclotide, pibrentasvir, desmopressin, and cyanocobalamin. Dashed line bisects opposing nsp15 trimers. The complete pocket is occluded by interactions between opposing trimers. (B) Binding pocket 2, predicted for rifamixin, rifapentine, and everolimus. Dashed lines intersect interfaces between individual monomers of one nsp15 trimer. Binding pockets remain exposed in the interior cavity of nsp15. Depictions generated based on PDB structure 7N06.
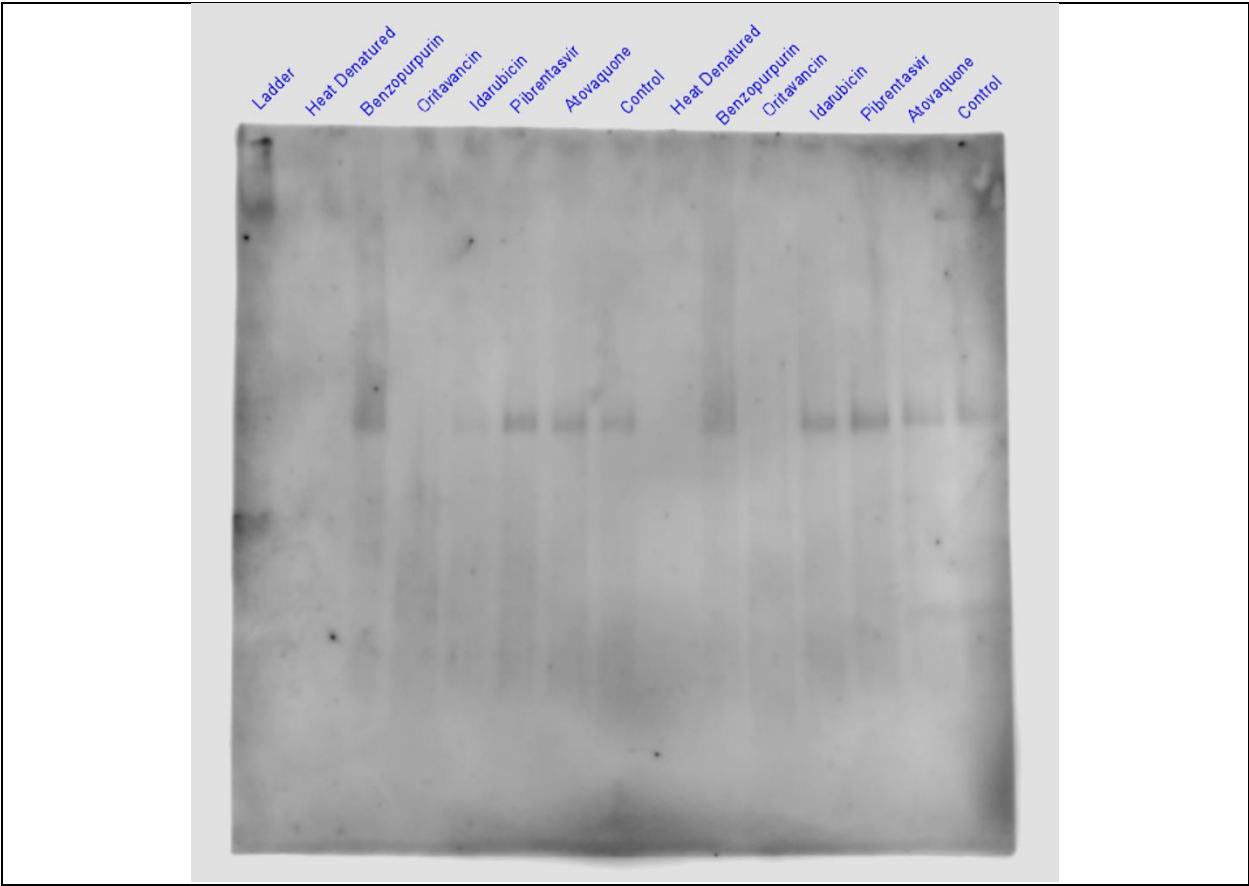
Supplemental Figure 3. Evaluation of drug-induced nsp15 aggregation. N-terminally his-tagged nsp15 was diluted to 700nM in NendoU Buffer containing 5mM $MnCl_2$ with or without 100µM of the indicated drug. Control and drug treated samples were then heated at 37°C for 10 minutes to simulate the nuclease assay reaction conditions. As a positive control, an additional preparation of nsp15 without drug was heated to 95°C for 10 minutes (Heat Denatured). Following incubation, the protein preparations were then separated on a non-denaturing polyacrylamide gel and evaluated by western blot. Control samples each produced a single band of the expected size corresponding to hexameric nsp15 (~240kDa), while the heat denatured samples produced no observable bands. Benzopurpurin, idarubicin, pibrentasvir, and atovaquone all produced a single band of similar size and staining intensity as control protein. However, oritavancin produced no detectable bands and appeared like the heat denatured aggregation positive control. Data presented is two of four repeats.

Lanes:

1. NativeMark Unstained Protein Standard
2. Heat denatured nsp15, replicate 1
3. Benzopurpurin treated nsp15, replicate 1
4. Oritavancin treated nsp15, replicate 1
5. Idarubicin treated nsp15, replicate 1
6. Pibrentasvir treated nsp15, replicate 1
7. Atovaquone treated nsp15, replicate 1
8. Control nsp15, replicate 1
9. Heat denatured nsp15, replicate 2
10. Benzopurpurin treated nsp15, replicate 2
11. Oritavancin treated nsp15, replicate 2
12. Idarubicin treated nsp15, replicate 2
13. Pibrentasvir treated nsp15, replicate 2
14. Atovaquone treated nsp15, replicate 2
15. Control nsp15, replicate 2
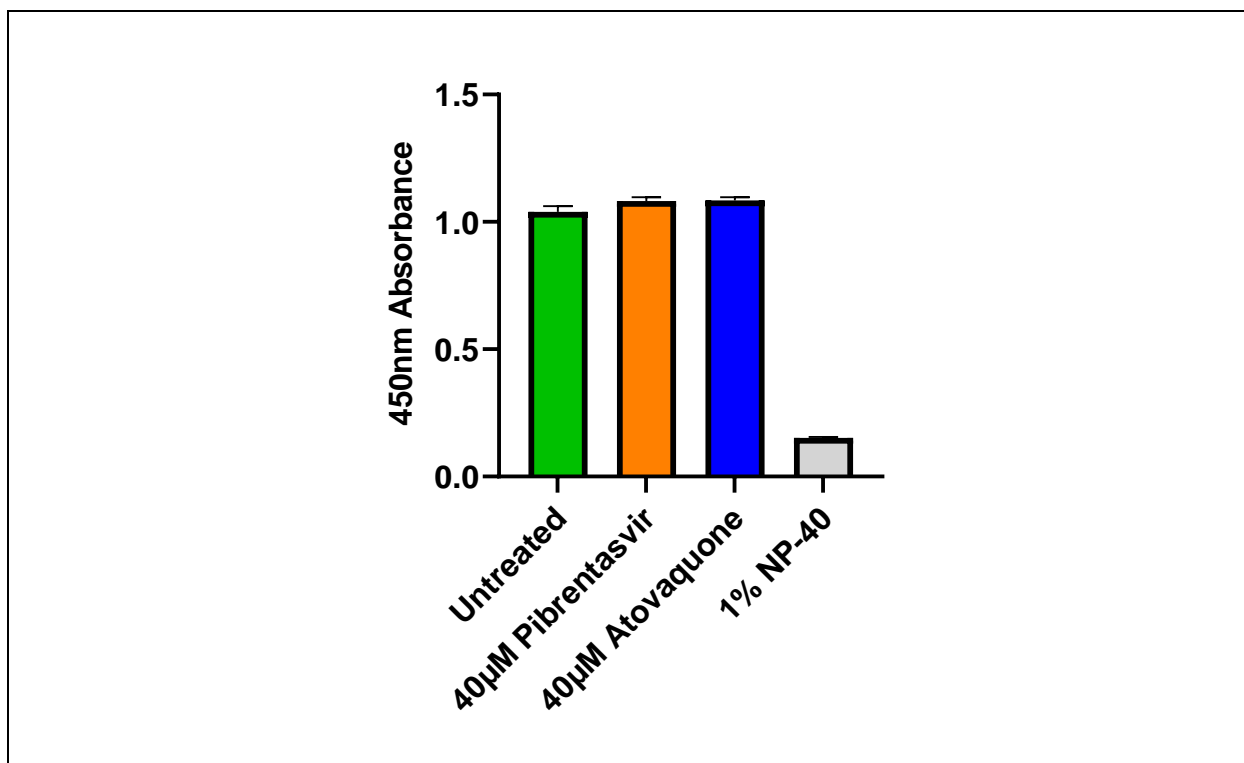
Supplemental Figure 4. MTS formazan formation viability assay. A549 wild-type cells were incubated for 24 hours with either control 1% FBS containing DMEM, or with the addition of 40μM atovaquone, 40μM pibrentasvir, or 1% NP-40. Metabolic activity was determined by addition of MTS reagent and production of the colored formazan product over a 1-hour period, measured by absorbance at 450nm. Results are representative of 1 experiment performed in triplicate.

OC43-N+
0.049

FSC-A

Specimen_001_No Virus.fcs
A549 Cells
8112

OC43-N+
1.93

FSC-A

Specimen_001_Virus Only.fcs
A549 Cells
8454

OC43-N+
0.44

FSC-A

Specimen_001_Pibrentasvir10uM.fcs
A549 Cells
8175

OC43-N+
0.61

FSC-A

Specimen_001_Atovaquone10uM.fcs
A549 Cells
6279
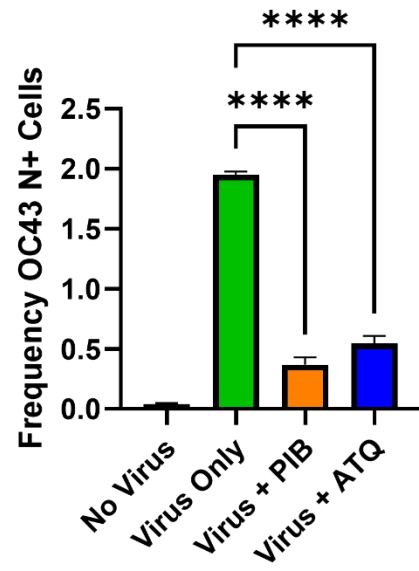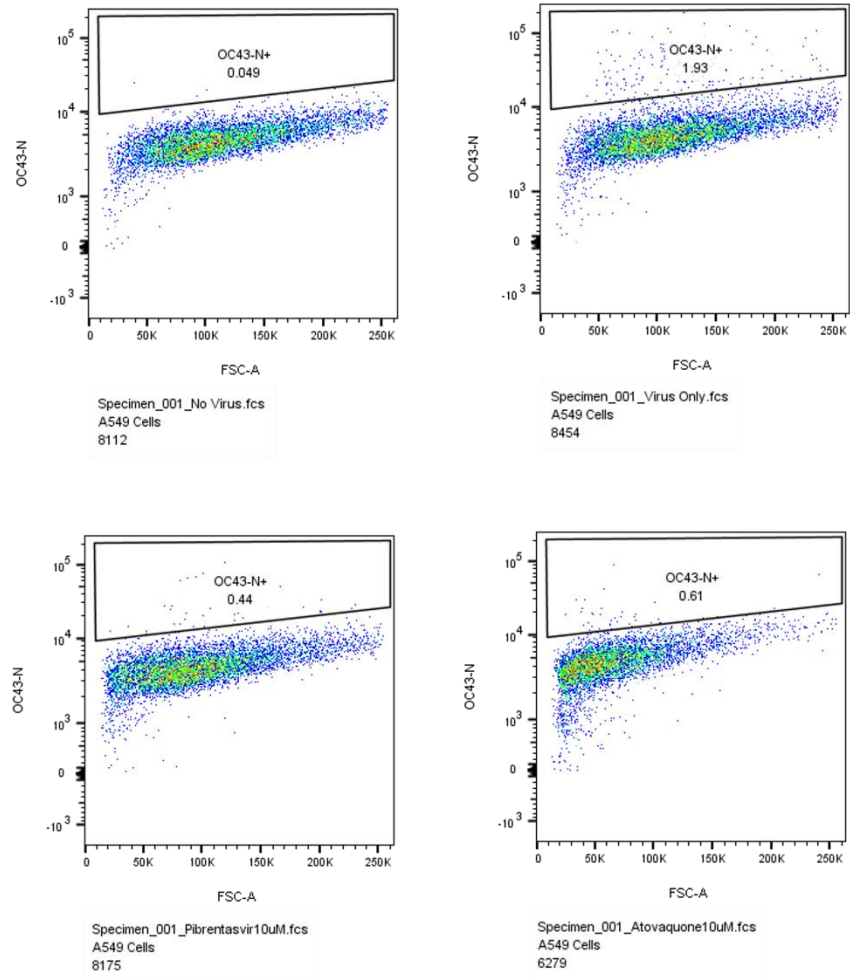
Supplemental Figure 5. Flow cytometric quantification of HCoV-OC43 infected cells with and without nsp15 inhibitor treatment. (A-D) Representative flow plots of A549 WT cells 12 hours post-infection with HCoV-OC43 at an MOI of 0.01. Inhibitors were added to a concentration of 10µM at 2 hours post-infection. At 12 hours post-infection, cells were trypsinized prior to fixation and permeabilization. HCoV-OC43 infected cells were detected by staining with primary mouse anti-HCoV-OC43 N protein and secondary Goat anti-mouse Ig conjugated to APC-Cy7. (A) Mock infected (B) HCoV-OC43 infected (C) HCoV-OC43 infected with 10µM pibrentasvir (D) HCoV-OC43 infected with 10µM atovaquone. (E) Graphical representation of flow plots presented in S2A. Columns and error bars are representative of 1 experiment performed in triplicate. Results analyzed by One-Way ANOVA with multiple comparisons. p-values represented as *<.05, **<.01, ***<.001, ****<.0001.

Chapter 4: Discussion

Repurposed drugs and biologics as novel antiviral compounds

Over the course of this thesis, we have endeavored to identify novel SARS-CoV-2 antivirals using two different interpretations of the drug repurposing approach. In chapter 2, we explored the potential of repurposing canonically antimicrobial cathelicidins from other species for antiviral efficacy, while in chapter 3 we employed a much more traditional approach to drug-repurposing by evaluating the potential of FDA approved small-molecule drugs to incidentally inhibit SARS-CoV-2. In both approaches, we are able to expedite the therapeutic discovery process by the exclusion of potentially toxic compounds from the candidate therapeutic pipeline. For cathelicidins, we rely on the mere existence of these peptides in humans and other species as evidence of their therapeutic potential, noting that the risk of toxicity towards humans likely increases as we traverse the evolutionary tree of life and diverge farther from the lineages of humans and mammals. By comparison, the study of small-molecule drugs takes a far more empirical approach, where the known toxicity profiles and pharmacokinetic properties aids in the selection of novel antivirals active at biologically relevant concentrations.

In chapter 2, we present the feasibility of mining zoonotic cathelicidins as novel human therapeutics. Our experiments began with identification and initial screening of cathelicidins from 16 diverse species for inhibition of SARS-CoV-2 in a simple focus forming assay. While only PMAP-36R (and later Yongshi) would present substantial inhibition of SARS-CoV-2, this screening would reinforce one of the core principles of this repurposing strategy, in that the vast majority of tested peptides (even those of non-mammalian origin) were not cytotoxic and did not disrupt the cell monolayer at physiological concentrations. Our experiments then turned towards engineering and mechanistic characterization of PMAP-36R, demonstrating that while inhibition relied on both the N-terminal and C-terminal elements, the peptide tolerated replacement of the penultimate cysteine residue. As previously demonstrated for

PMAP-36, removal of this cysteine prevents dimerization of the peptide, and thereby reduces toxicity towards mammalian cells, but this was not coupled to reduced viral inhibition[127]. The inhibition of this derivative peptide termed Yongshi remained active against the drifted variants of SARS-CoV-2 and relied on a combination of cellular pre-conditioning to an antiviral state and direct interactions with the SARS-CoV-2 virion. While searching for a mechanistic explanation for the efficacy of Yongshi compared to other cathelicidins, we discovered uncanny homology between Yongshi, and the heptad repeats of SARS-CoV-2. This potential heptad mimicry was reaffirmed by *in vitro* BLI studies and supports a non-canonical mechanism of fusion inhibition promoting Yongshi's antiviral effect.

While Yongshi presents some definitive antiviral activity, it remains an active area of discovery as to how to deploy Yongshi, or for that matter, any other antiviral peptide for therapeutic effect. In further unpublished studies, we have begun developing an mRNA formulation of Yongshi for *in situ* production of the antiviral peptide (See Appendix A for Methods). This formulation is based on the *in vitro* synthesis of a Semliki Forest Virus self-amplifying replicon, bearing a Yongshi transgene, which is conjugated to a nanostructured-lipid carrier for intranasal delivery to airway epithelial cells (Figure 1A). We first validated production of the Yongshi transgene by western blot of cells transfected with the mRNA construct (Figure 1B). While lacking a specific antibody for Yongshi, we were only able to quantify transgene activity in the mCRAMP-Yongshi fused variant but extrapolated this result to the other tested constructs. We then complexed the synthetic mRNA constructs to a nano-structured lipid carrier as previously described for use in an *in vivo* murine infection model of SARS-CoV-2[226]. Briefly, mice were dosed intranasally with 50µL of NLC (vehicle) or 50µL NLC complexed with 5µg of mRNA, rested for 3 days, infected intranasally with SARS-CoV-2, and then euthanized on day 3 post infection for RNA collection (Figure 1C). This approach yielded several interesting results that may guide the design of future antiviral mRNA constructs. First, a simple secreted Yongshi transgene was toxic to the mice,

causing substantial weight loss in the first 3 days after administration, however this was abated either by fusing the C-terminus of Yongshi to the N-terminus of a GPI-anchor sequence or the N-terminus of Yongshi to the C-terminus of the murine CRAMP cathelin domain (Figure 1D). The mCRAMP-Yongshi fusion is theorized to maintain the storage and activation of Yongshi in the same manner of murine CRAMP. Further, neither the NLC-only, membrane bound, or cathelin fusion groups experienced significant differences in weight loss compared to the vector group on any study day. Second, the expression of the self-amplifying construct was predominantly in the nasal tissue and not the lungs, was consistent across groups 6 days after NLC delivery, and was not impacted by the presence of the Yongshi transgene (Figure 1E-F). Finally, administration of either the vector only control or the mCRAMP-Yongshi fusion construct was able to inhibit SARS-CoV-2 replication in the nasal turbinates, but not the lungs (Figure 1G-J). Notably, the degree of infection inhibition was the same between the vector only and mCRAMP-Yongshi fusion groups, suggesting the effect is largely due to the induced innate immune response to the mRNA construct and not due to the presence of the Yongshi transgene. More work is needed to understand why a therapeutic effect may not have been seen for the mCRAMP-Yongshi fusion group, whether this transgene is properly secreted into airways and further cleaved into its active form is currently unknown. Similarly, it is also unknown whether the observed titers of the mRNA constructs on day 6 are enough to drive the antiviral concentrations of Yongshi protein tested *in vitro*.

In chapter 3 we employed new high-powered *in silico* techniques to curate a list of FDA-approved drugs with complementary chemical structures to the binding pockets of the SARS-CoV-2 nsp15. This approach proved to be efficacious, as 1 of the 11 *in silico* compounds identified by us (pibrentasvir) and 2 of the 4 compounds predicted by another research lab (atovaquone and idarubicin) reduced the enzymatic activity of nsp15 by >50% at 100μM. However, the sieve of drug discovery is a difficult barrier, and though idarubicin strongly inhibits recombinant nsp15 in solution, it was ultimately

too toxic in cell culture. Further characterization of the remaining two drugs, pibrentasvir and atovaquone, revealed they were highly effective against SARS-CoV-2 and the distantly related HCoV-OC43 infection of Vero E6 and A549 cells respectively. Of interest, the inhibitory activity of atovaquone was dependent on the cellular expression of MAVS, a signaling intermediary of intracellular dsRNA PRRs, and was linked to altered localization of viral dsRNA. These two observations further support that a major mechanism of action for atovaquone is nsp15 dependent, but that pibrentasvir only minorly affects nsp15 in the context of cellular infection. However, despite the observed inhibition of SARS-CoV-2 at pharmacologically attainable concentrations, neither pibrentasvir nor atovaquone would translate to *in vivo* efficacy in a mouse model of SARS-CoV-2. This again highlights the sieve of drug discovery, as the complexity of factors influencing antiviral effects compounds when moving from recombinant protein to cellular models, so does this repeat when moving from *in vitro* to *in vivo*.

In the larger context of SARS-CoV-2 antiviral drug development, drug-repurposing would be a defining feature of successful therapeutics. However, unlike our own studies, the roots of the three successful SARS-CoV-2 antivirals (remdesivir, molnupiravir, and Paxlovid) would all derive from previous antivirals. The relationship for remdesivir is the most evident, as this drug was originally developed for the treatment of hepatitis C, but would later be discovered to also inhibit the coronaviruses SARS-CoV, MERS-CoV, HCoV-NL63, HCoV-OC43, HCoV-229E, Bat-CoV HKU5, Bat-CoV HKU3, Bat-CoV SCH014, Bat-CoV WIV1, MHV, PDCoV[227-229]. These early pre-pandemic discoveries would lead to the rapid repurposing and adoption of remdesivir for the treatment of SARS-CoV-2. Similarly, molnupiravir had been previously developed for the treatment of influenza virus infection but was only at the stage of preclinical testing when the COVID-19 pandemic began[230]. Still, early and rapid screening resulted in molnupiravir being identified as a potent inhibitor of SARS-CoV, SARS-CoV-2, MERS-CoV, MHV, Bat-CoV HKU3, Bat-CoV HKU5, and Bat-CoV SHC014; ultimately leading to its further development as a SARS-

CoV-2 therapeutic[231]. Unlike remdesivir and molnupiravir, nirmatrelvir is not truly a "repurposed" drug as its exact chemical structure was not designed until after the emergence of SARS-CoV-2. However, the discovery of the prodrug nirmatrelvir and its active counterpart lufotrelvir is based on the chemical modification of the previously discovered human rhinovirus 3C-protease inhibitor rupintrivir[232].

In this regard, there are significant parallels between our own studies and those which yielded the life-saving antivirals of the SARS-CoV-2 pandemic. Even more-so, these successes and our own work highlight the power of drug-repurposing and the importance of investment in discovering new drugs to non-pandemic viruses as means to accelerate discoveries during a pandemic event.

Targeting conserved structures produces pandemic ready solutions

In order to establish durable safeguards to limit the damage of future pandemic outbreaks, newly designed therapeutics should primarily target conserved viral structures. The value in such a design strategy is immediately apparent when comparing the small molecule drugs of remdesivir, molnupiravir, and nirmatrelivir to the SARS-CoV-2 monoclonal antibody therapies.

Currently, no monoclonal therapies are approved for the treatment of SARS-CoV-2, as mutations within Omicron and earlier lineages of SARS-CoV-2 completely escaped neutralization by all developed monoclonal antibody therapies within 2 years of deployment[8,9]. The rapid evolution of escape variants towards these therapies is best attributed to the "immune exposed" nature of the SARS-CoV-2 spike protein and looser constraints on the receptor binding domain compared to catalytic structures. Effectively, the SARS-CoV-2 spike is under constant selective pressure from host derived antibodies due to being present on the virion surface and necessary for cellular infection. This is the canonical embodiment of the Red Queen hypothesis, as the virus and human immunity on the whole must

continually improve to avoid extinction, but the monoclonal antibodies "standing still" quickly become irrelevant. This is in contrast to many of the intracellular proteins expressed by SARS-CoV-2 such as the RdRp targeted by remdesivir and molnupiravir, the 3CL-protease targeted by Paxlovid, and the endoribonuclease targeted by atovaquone in our own studies. Though patients may develop antibodies against these targets from lytic cells, the proteins themselves are never exposed to antibodies inside infected cells. While these proteins can be digested and presented on MHC class I to cytotoxic CD8 T cells, this mechanism does not exert a strong selective effect on protein evolution. This is in part due to the high heterogeneity of MHC in human populations, meaning that the assortment of MHC peptide complexes varies substantially between individuals and any one viral protein modification is unlikely to provide a population level advantage by immune escape[233].

The spike protein of SARS-CoV-2 is also less constrained in terms of its function compared to intracellular catalytic factors. The RBD of the spike protein must only bind the ACE2 receptor long enough to allow cleavage by TMPRSS2 or internalization by endocytic means, but otherwise performs no additional actions. The RdRp, 3CL-protease, and endoribonuclease all must not only bind their respective substrates, but then engage in a secondary catalytic reaction, creating substantial restrictions for the evolution of drug escape variants. Furthermore, the binding interaction of spike and ACE2 or spike and antibody is determined by a relatively large surface area on the folded protein, compared to the catalytic proteins which are interacting with only a few residues or a few bases of protein or RNA substrate at any one time. Essentially, the spike protein has a greater degree of freedom to introduce mutations which ablate antibody binding without disrupting its core function of ACE2 binding. Indeed, there has been the documented appearance of resistance mutations to remdesivir and Paxlovid, but these have not spread at a population level, likely due to a lack of selective advantage outside the hospital environment[234,235].

These comparisons between the spike and catalytic proteins of SARS-CoV-2 demonstrate the importance of targeting structures that are not just conserved across viral families, but which are heavily constrained by their interactions with invariant substrates. Our own studies of atovaquone and nsp15 fit squarely into this paradigm. As discussed in detail in chapter 1, the overall sequence of the endoribonuclease varies between individual coronaviruses and arteriviruses, but the core catalytic triad responsible for uridylate-specific cleavage is uniquely invariant. Similarly, our exploration of cathelicidin antivirals was originally predicated on the identification of peptides with differential binding to the viral lipid envelope, but subsequently identified specific interactions of Yongshi with the conserved S2 region of the spike protein. To summarize, the rapid identification and deployment of COVID-19 small molecule inhibitors was rooted in the studies of pre-pandemic coronavirus inhibitors targeting conserved structures and continued identification of such inhibitors is an imperative act of vigilance against future pandemics.

The future of Yongshi and nsp15 inhibitors

The experiments conducted in this thesis adhere to the principles of drug-repurposing and the targeting of conserved structures, but ultimately stop short of producing an antiviral successful in preclinical animal models. We have already discussed the possible factors potentially contributing to this outcome, be it poor cleavage of the Yongshi precursor or low bioavailability of atovaquone and pibrentasvir. To address these shortcomings, engineering of new derivative peptides and small molecules will almost certainly be necessary.

Beginning with Yongshi, while the peptide possesses an antiviral activity decoupled from its cytotoxicity, which was unique among our tested cathelicidins, the overall therapeutic index is modest at just over a 4-fold difference between the IC_{50} and TD_{50}. Our studies performed reductive experiments

to identify key residues related to antiviral effect in PMAP-36R, but did not pursue further mutational experiments to generate peptides with greater discriminatory capacity for host and viral components. To rationally design new peptide derivatives, a more complete understanding of Yongshi's unique interactions with the viral membrane and the heptad repeats is necessary. These should include lipidomics based experiments to study the incorporation of Yongshi into viral and host membranes as well as more complex binding studies to determine whether Yongshi can not only bind the HR1 of SARS-CoV-2 but can also displace HR2 in a physiological setting. Separately, detailed characterization of the expression and post-translational processing of the CRAMP-Yongshi fusion construct will determine how this synthetic peptide may be further optimized. Mass spectrometry of the mucosal fluid following mRNA delivery can be used to detect the production of the CRAMP-Yongshi peptide, the proportion of the cleaved Yongshi peptide, and further relate the concentration of this peptide to other endogenous proteins, including the endogenous murine CRAMP cathelicidin.

For the drugs atovaquone and pibrentasvir, each are effective in cell culture well below their toxic thresholds, but this does not translate to *in vivo* efficacy even at similar plasma level concentrations. While it may be possible to further increase the doses for each compound above those approved for human use, a better approach is to employ atovaquone and pibrentasvir as model compounds to be edited by the addition or removal of chemical moieties to generate molecules effective at lower concentrations. However, this again relies on detailed mapping of the interactions between each compound and its molecular target in SARS-CoV-2. Further, while we provide evidence for atovaquone's function as a nsp15 inhibitor, the activity of pibrentasvir appears largely determined by other viral factors. As the activity of atovaquone and pibrentasvir are conserved in HCoV-OC43, an important first experiment would be to evolve HCoV-OC43 in the presence of sub-neutralizing concentrations of atovaquone and pibrentasvir by serial passaging. Resistant strains could then be

sequenced to identify the location of resistance mutations, and further understand the molecular targets of each drug. Finally, the holy grail of such an inhibitor study would be to capture a crystal structure of each drug complexed with its target viral protein. This would permit the structure-based design necessary to improve atovaquone and pibrentasvir, and potentially produce the first nsp15 inhibitor successful in pre-clinical models.

Figures
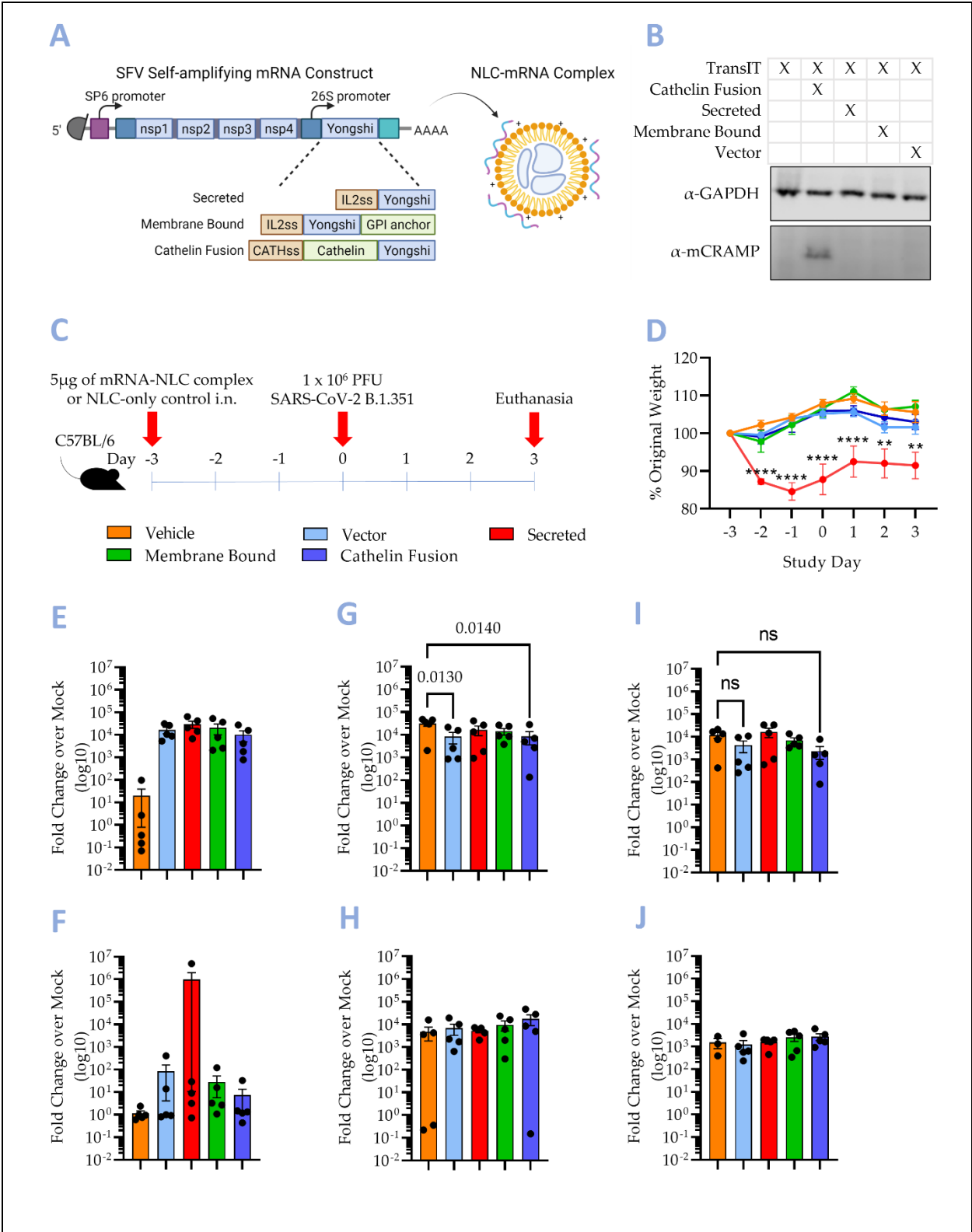
Figure 1. Characterization of a self-amplifying mRNA construct for therapeutic delivery of Yongshi. (A) Schematic of self-amplifying mRNA construct based on the Semliki Forest virus replicon and complexation to a nano-structured lipid carrier molecule. 4 constructs were produced and tested including the base vector without a Yongshi transgene (vector), a variant bearing the IL2 signal sequence followed by Yongshi (secreted), a variant bearing Yongshi sandwiched between the IL2 signal sequence and the CD59 GPI-anchor sequence (membrane bound), or a variant with the murine CRAMP signal sequence and cathelin domains fused to Yongshi (cathelin fusion). (B) Western blot of HEK293 cells transfected with each mRNA construct and stained with α-GAPDH and α-mCRAMP cathelin domain. (C) Schematic of mouse model testing prophylactic administration of each mRNA construct in SARS-CoV-2 B.1.351 infection. (D) Mouse weight analysis. Weights were collected daily, and groups were compared to the vector mouse group for statistical analysis. Significance was determined by two-way ANOVA with Dunnet's test for multiple comparisons. *<.05, **<.01, ***<.001, ****<.001. (E-J) RT-qPCR determination of mRNA construct (E-F), viral RdRp (G-H), and viral sub-genomic (I-J) titers on day 3 post-infection from turbinate (E,G,I) and lung (F,H,J) tissue. RT-qPCR data for each target gene is normalized to GAPDH and graphed relative to uninfected control mice. Statistical significance was determined by one-way ANOVA with Fisher's LSD test for multiple comparisons to vehicle control mice. Mouse experiments reflect 5 mice per group. We would also like to acknowledge and thank Mehul S. Suthar and Katharine Floyd for performing the murine infection experiments detailed in panels D-J.

Appendix A: Methods for Yongshi self-amplifying mRNA construct experiments.

Design and synthesis of self-amplifying mRNA constructs

Self-amplifying mRNA constructs were designed based on the Semliki Forest Virus (SFV) replicon encoded by the pSFV1 eukaryotic expression vector (Cat#: 18448-019, Invitrogen). Codon optimized Yongshi mRNA variants were purchased as gBlock gene fragments from IDT with appropriate 5' and 3' cloning adapters. gBlocks were cloned into the pSFV1 vector by standard techniques using the SmaI and BamHI restriction sites. Successful ligation was confirmed using the SP1 (5'-CGGCGGTCCTAGATTGGTGCG-3') and SP2 (5'-CGCGGGCGCCACCGGCGGCCG-3') sequencing primers.

Secreted Yongshi AA sequence	MYRMQLLSCIALSLALVTNSG<u>VGRFRRLRKKTRKRLKKIGKVLKWIPPIVGSIPLGSG</u>
Membrane bound Yongshi AA sequence	MYRMQLLSCIALSLALVTNSG<u>VGRFRRLRKKTRKRLKKIGKVLKWIPPIVGSIPLGSG</u>NGGTSLSEKTVLLLVTPFLAAAWSLHP
mCRAMP cathelin fusion Yongshi AA sequence	MQFQRDVPSLWLWRSLSLLLLLGLGFSQTPSYRDAVLRAVDDFNQQSLDTNLYRLLDLDPEPQGDEDPDTPKSVRFRVKETVCGKAERQLPEQCAFKEQGVVKQCMGAVTLNPAADSFDISCNEPGAQPFRFKK<u>VGRFRRLRKKTRKRLKKIGKVLKWIPPIVGSIPLGSG</u>

In vitro synthesis of self-amplifying mRNA

pSFV1 plasmid constructs were grown in One Shot Stbl3 *E. coli* at 30° C overnight and purified with the ZymoPURE II plasmid prep system (Cat#: D4200, Zymo Research). 5µg of purified plasmid was digested with SpeI-HF enzyme overnight at 37°C. Linearized plasmid was precipitated with EDTA, sodium acetate, and ethanol and then resuspended in 25µL of Rnase free water. mRNA synthesis was carried out using the mMESSAGE mMACHINE SP6 transcription kit (Cat#: AM1340, Thermo Fisher Scientific Scientific) according to the manufacturer's recommendations. 20µL transcription reactions were supplemented with 1µL of GTP and incubated for 3 hours instead of 1 to improve yield of the 9kb mRNA

transcript. pSFV1 template DNA was removed by digestion with 1µL TURBO DNase prior to purification of mRNA transcripts using the MEGAclear kit (Cat#: AM1908, Thermo Fisher Scientific Scientific) according to the manufacturer's recommendations. RNA was eluted using the included elution solution heated to 95°C to maximize mRNA recovery. Eluted mRNA was divided into 5µg aliquots and stored at -80°C until use.

Transfection of HEK293 cells with mRNA complexes

24 hours prior to transfection, 3×10^5 HEK293 cells were plated in each well of a 12-well plate in 1mL of DMEM + 10% FBS. 1 hour prior to transfection the media was replaced with fresh DMEM containing 10% FBS. 1µg of synthesized mRNA was diluted in 100µL of OptiPro SFM medium and complexed with 2µL of Boost mRNA and 2µL of TransIT mRNA reagent (Cat#:MIR 2225, Mirus) for 5 minutes. 100µL of TransIT mRNA complexes were added to each well. 72 hours after transfection cell lysates were harvested with 100µL of RIPA buffer.

Western blot of mRNA transfected cells

Cell lysates were mixed with NuPAGE LDS Sample buffer and β-mercaptoethanol before denaturing at 95°C for 5 minutes. Proteins were separated on a NuPAGE 4-12% Bis-Tris gel according to the manufacturer's recommendations and transferred to a nitrocellulose membrane. Membranes were blocked in 1X TBST + 5% Dry Milk for 1 hour at room temperature. Blocked membranes were incubated with primary antibody diluted 1:1000 in 1X TBST + 3% BSA overnight at 4°C. Unbound primary was removed by 3 washes with 1X TBST, before incubation with secondary antibody diluted 1:10,000 in 1X TBST + 3% BSA. Unbound secondary was removed by 3 washes with 1X TBST. Nsp1 and CRAMP protein

bands were detected by chemiluminescence using SuperSignal West Femto substrate. Unfortunately, a specific band for Semliki-Forest-Virus nsp1 could not be detected by cross-reactivity with the Chikungunya-nsp1 antibody (data not shown). GAPDH was recorded by fluorescence using the 800nm channel. Antibodies used are as follows: rabbit anti-CRAMP (Cat#: 139643, US Biological), rabbit anti-Chikungunya nsp1 (Cat#:GTX135191, GeneTex), mouse anti-GAPDH (Cat#: 649201, BioLegend), goat anti-rabbit Ig HRP (Cat#: 4030-05, SouthernBiotech), goat anti-mouse Ig 800CW (Cat#: 926-32210, LI-COR). Size analysis performed using PageRuler Plus Prestained Protein Ladder (Cat#: 26619, Thermo Fisher Scientific) as a reference.

Complexation of mRNA constructs with NLC

To prepare mRNA-NLC complexes, a 10mM sodium citrate buffer solution (SCB) and a 50% sucrose, 10mM sodium citrate buffer solution (SSCB) were first prepared and adjusted to a pH of 6.3 by dropwise addition of 1M HCl. Component A was produced by diluting 18.6μL of NLC with 35μL of SSCB and 121.4μL of SCB. Component B was produced by diluting 35μg of purified mRNA construct with 35μL of SSCB and enough SCB to reach a final volume of 175μL. Component A and B were then rapidly mixed by pipetting and incubated on wet ice for 30 minutes.

Mouse mRNA construct delivery and infection

For each group, five C57BL/6 mice were lightly anesthetized with isoflurane prior to delivery of 25μL of NLC-mRNA complex solution to each nare. 72 hours after priming with the NLC-mRNA construct, mice were infected with 1×10^6 PFU of SARS-CoV-2 B.1.351 virus via the i.n. route in an animal biosafety

level 3 (ABSL-3) facility. Mice were monitored daily for weight loss. All experiments adhered to the

guidelines approved by the Emory University Institutional Animal Care and Use Committee.

Quantitative reverse transcription-PCR of lung tissues

At three days post-infection, mice were euthanized with an isoflurane overdose. One lobe of

lung tissue and nasal turbinates were collected in an Omni Bead Ruptor tube filled with Tripure Isolation

Reagent (Roche, catalog#: 11667165001). Tissue was homogenized using an Omni Bead Ruptor 24

instrument (5.15 ms, 15 s) and then centrifuged to remove debris. RNA was ex-tracted using a Direct-zol

RNA Miniprep Kit (Zymo, catalog#: R2051) and then converted to cDNA using a high-capacity reverse

transcriptase cDNA kit (Thermo, catalog#: 4368813). To quantify RNA, IDT Prime Time gene expression

master mix and were used with mouse GAPDH, SARS-CoV-2 RDRP, and SARS-CoV-2 subgenomic-specific

TaqMan gene expression primer/probe sets as previously described[212,213]. mRNA construct RNA was

quantified using a custom IDT primer probe set against the SFV nsp3 region (F': 5'-

ACAGACTGTCACTGAGCAG-3', R': 5'-TCTCTGCAGTAGATGGTCAC-3', Probe: 5'-

AGATAGGCTGCAGCAATCCCTCAA-3'). All qPCRs were performed in 384-well plates and run on a

QuantStudio5 qPCR system.

Works Cited

1   Zhou, P. *et al.* A pneumonia outbreak associated with a new coronavirus of probable bat origin. *Nature* **579**, 270-273, doi:10.1038/s41586-020-2012-7 (2020).

2   Lytras, S. *et al.* Exploring the Natural Origins of SARS-CoV-2 in the Light of Recombination. *Genome Biol Evol* **14**, doi:10.1093/gbe/evac018 (2022).

3   Feng, E. C., Amy. *Restrictions and rewards: how China is locking down half a billion citizens*, <https://www.npr.org/sections/goatsandsoda/2020/02/21/806958341/restrictions-and-rewards-how-china-is-locking-down-half-a-billion-citizens> (2020).

4   *CDC Museum COVID-19 Timeline*, <https://www.cdc.gov/museum/timeline/covid19.html> (2023).

5   Haug, N. *et al.* Ranking the effectiveness of worldwide COVID-19 government interventions. *Nat Hum Behav* **4**, 1303-1312, doi:10.1038/s41562-020-01009-0 (2020).

6   Korley, F. K. *et al.* Early Convalescent Plasma for High-Risk Outpatients with Covid-19. *N Engl J Med* **385**, 1951-1960, doi:10.1056/NEJMoa2103784 (2021).

7   Levine, A. C. *et al.* COVID-19 Convalescent Plasma Outpatient Therapy to Prevent Outpatient Hospitalization: A Meta-analysis of Individual Participant Data From Five Randomized Trials. *medRxiv*, doi:10.1101/2022.12.16.22283585 (2022).

8   Cox, M. *et al.* SARS-CoV-2 variant evasion of monoclonal antibodies based on in vitro studies. *Nat Rev Microbiol* **21**, 112-124, doi:10.1038/s41579-022-00809-7 (2023).

9   *FDA Announces Bebtelovimab is Not Currently Authorized in Any US Region*, <https://www.fda.gov/drugs/drug-safety-and-availability/fda-announces-bebtelovimab-not-currently-authorized-any-us-region> (2022).

10   Al-Bari, M. A. A. Targeting endosomal acidification by chloroquine analogs as a promising strategy for the treatment of emerging viral diseases. *Pharmacol Res Perspect* **5**, e00293, doi:10.1002/prp2.293 (2017).

11   Oliver, M. E. & Hinks, T. S. C. Azithromycin in viral infections. *Rev Med Virol* **31**, e2163, doi:10.1002/rmv.2163 (2021).

12   Sheahan, T. P. *et al.* Comparative therapeutic efficacy of remdesivir and combination lopinavir, ritonavir, and interferon beta against MERS-CoV. *Nat Commun* **11**, 222, doi:10.1038/s41467-019-13940-6 (2020).

13   Pruijssers, A. J. *et al.* Remdesivir Inhibits SARS-CoV-2 in Human Lung Cells and Chimeric SARS-CoV Expressing the SARS-CoV-2 RNA Polymerase in Mice. *Cell Rep* **32**, 107940, doi:10.1016/j.celrep.2020.107940 (2020).

14   Gottlieb, R. L. *et al.* Early Remdesivir to Prevent Progression to Severe Covid-19 in Outpatients. *N Engl J Med* **386**, 305-315, doi:10.1056/NEJMoa2116846 (2022).

15   Beigel, J. H. *et al.* Remdesivir for the Treatment of Covid-19 - Final Report. *N Engl J Med* **383**, 1813-1826, doi:10.1056/NEJMoa2007764 (2020).

16   Dryden-Peterson, S. *et al.* Nirmatrelvir Plus Ritonavir for Early COVID-19 in a Large U.S. Health System : A Population-Based Cohort Study. *Ann Intern Med* **176**, 77-84, doi:10.7326/M22-2141 (2023).

17   Jayk Bernal, A. *et al.* Molnupiravir for Oral Treatment of Covid-19 in Nonhospitalized Patients. *N Engl J Med* **386**, 509-520, doi:10.1056/NEJMoa2116044 (2022).

18   Group, R. C. *et al.* Dexamethasone in Hospitalized Patients with Covid-19. *N Engl J Med* **384**, 693-704, doi:10.1056/NEJMoa2021436 (2021).

19   Ahmed, M. H. & Hassan, A. Dexamethasone for the Treatment of Coronavirus Disease (COVID-19): a Review. *SN Compr Clin Med* **2**, 2637-2646, doi:10.1007/s42399-020-00610-8 (2020).

20   Hoang, T. N. *et al.* Baricitinib treatment resolves lower-airway macrophage inflammation and neutrophil recruitment in SARS-CoV-2-infected rhesus macaques. *Cell* **184**, 460-475 e421, doi:10.1016/j.cell.2020.11.007 (2021).

21   Kalil, A. C. *et al.* Baricitinib plus Remdesivir for Hospitalized Adults with Covid-19. *N Engl J Med* **384**, 795-807, doi:10.1056/NEJMoa2031994 (2021).

22   Marconi, V. C. *et al.* Efficacy and safety of baricitinib for the treatment of hospitalised adults with COVID-19 (COV-BARRIER): a randomised, double-blind, parallel-group, placebo-controlled phase 3 trial. *Lancet Respir Med* **9**, 1407-1418, doi:10.1016/S2213-2600(21)00331-3 (2021).

23   Guimaraes, P. O. *et al.* Tofacitinib in Patients Hospitalized with Covid-19 Pneumonia. *N Engl J Med* **385**, 406-415, doi:10.1056/NEJMoa2101643 (2021).

24   Salama, C. *et al.* Tocilizumab in Patients Hospitalized with Covid-19 Pneumonia. *N Engl J Med* **384**, 20-30, doi:10.1056/NEJMoa2030340 (2021).

25   Rosas, I. O. *et al.* Tocilizumab in Hospitalized Patients with Severe Covid-19 Pneumonia. *N Engl J Med* **384**, 1503-1516, doi:10.1056/NEJMoa2028700 (2021).

26   group, C.-C. Sarilumab in adults hospitalised with moderate-to-severe COVID-19 pneumonia (CORIMUNO-SARI-1): An open-label randomised controlled trial. *Lancet Rheumatol* **4**, e24-e32, doi:10.1016/S2665-9913(21)00315-5 (2022).

27   Lescure, F. X. *et al.* Sarilumab in patients admitted to hospital with severe or critical COVID-19: a randomised, double-blind, placebo-controlled, phase 3 trial. *Lancet Respir Med* **9**, 522-532, doi:10.1016/S2213-2600(21)00099-0 (2021).

28   Donato, A. A. In non-critically ill patients with COVID-19, therapeutic anticoagulation improved survival to discharge without organ support. *Ann Intern Med* **174**, JC134, doi:10.7326/ACPJ202112210-134 (2021).

29   Investigators, R.-C. *et al.* Therapeutic Anticoagulation with Heparin in Critically Ill Patients with Covid-19. *N Engl J Med* **385**, 777-789, doi:10.1056/NEJMoa2103417 (2021).

30   Zhang, L. *et al.* The D614G mutation in the SARS-CoV-2 spike protein reduces S1 shedding and increases infectivity. *bioRxiv*, doi:10.1101/2020.06.12.148726 (2020).

31   Markov, P. V. *et al.* The evolution of SARS-CoV-2. *Nat Rev Microbiol* **21**, 361-379, doi:10.1038/s41579-023-00878-2 (2023).

32   Tian, F. *et al.* N501Y mutation of spike protein in SARS-CoV-2 strengthens its binding to receptor ACE2. *Elife* **10**, doi:10.7554/eLife.69091 (2021).

33   Meng, B. *et al.* Recurrent emergence of SARS-CoV-2 spike deletion H69/V70 and its role in the Alpha variant B.1.1.7. *Cell Rep* **35**, 109292, doi:10.1016/j.celrep.2021.109292 (2021).

34   Jangra, S. *et al.* The E484K mutation in the SARS-CoV-2 spike protein reduces but does not abolish neutralizing activity of human convalescent and post-vaccination sera. *medRxiv*, doi:10.1101/2021.01.26.21250543 (2021).

35   Keyel, A. C. *et al.* SARS-CoV-2 Vaccine Breakthrough by Omicron and Delta Variants, New York, USA. *Emerg Infect Dis* **28**, 1990-1998, doi:10.3201/eid2810.221058 (2022).

36   Fan, Y. *et al.* SARS-CoV-2 Omicron variant: recent progress and future perspectives. *Signal Transduct Target Ther* **7**, 141, doi:10.1038/s41392-022-00997-x (2022).

37   Mohapatra, R. K. *et al.* The recently emerged BA.4 and BA.5 lineages of Omicron and their global health concerns amid the ongoing wave of COVID-19 pandemic - Correspondence. *Int J Surg* **103**, 106698, doi:10.1016/j.ijsu.2022.106698 (2022).

38   Parums, D. V. Editorial: The XBB.1.5 ('Kraken') Subvariant of Omicron SARS-CoV-2 and its Rapid Global Spread. *Med Sci Monit* **29**, e939580, doi:10.12659/MSM.939580 (2023).

39   Kalathiya, U. *et al.* Highly Conserved Homotrimer Cavity Formed by the SARS-CoV-2 Spike Glycoprotein: A Novel Binding Site. *J Clin Med* **9**, doi:10.3390/jcm9051473 (2020).

40   Peacock, T. P. *et al.* The furin cleavage site in the SARS-CoV-2 spike protein is required for transmission in ferrets. *Nat Microbiol* **6**, 899-909, doi:10.1038/s41564-021-00908-w (2021).

41   Zhang, J., Xiao, T., Cai, Y. & Chen, B. Structure of SARS-CoV-2 spike protein. *Curr Opin Virol* **50**, 173-182, doi:10.1016/j.coviro.2021.08.010 (2021).

42   Yan, R. *et al.* Structural basis for the recognition of SARS-CoV-2 by full-length human ACE2. *Science* **367**, 1444-1448, doi:10.1126/science.abb2762 (2020).

43   Premkumar, L. *et al.* The receptor binding domain of the viral spike protein is an immunodominant and highly specific target of antibodies in SARS-CoV-2 patients. *Sci Immunol* **5**, doi:10.1126/sciimmunol.abc8413 (2020).

44   Wrapp, D. *et al.* Cryo-EM structure of the 2019-nCoV spike in the prefusion conformation. *Science* **367**, 1260-1263, doi:10.1126/science.abb2507 (2020).

45   Lam, S. D., Waman, V. P., Fraternali, F., Orengo, C. & Lees, J. Structural and energetic analyses of SARS-CoV-2 N-terminal domain characterise sugar binding pockets and suggest putative impacts of variants on COVID-19 transmission. *Comput Struct Biotechnol J* **20**, 6302-6316, doi:10.1016/j.csbj.2022.11.004 (2022).

46   Padmanabhan, P., Desikan, R. & Dixit, N. M. Targeting TMPRSS2 and Cathepsin B/L together may be synergistic against SARS-CoV-2 infection. *PLoS Comput Biol* **16**, e1008461, doi:10.1371/journal.pcbi.1008461 (2020).

47   Xia, S. *et al.* Fusion mechanism of 2019-nCoV and fusion inhibitors targeting HR1 domain in spike protein. *Cell Mol Immunol* **17**, 765-767, doi:10.1038/s41423-020-0374-2 (2020).

48   Bayati, A., Kumar, R., Francis, V. & McPherson, P. S. SARS-CoV-2 infects cells after viral entry via clathrin-mediated endocytosis. *J Biol Chem* **296**, 100306, doi:10.1016/j.jbc.2021.100306 (2021).

49   Santamaria, A. *et al.* Strikingly Different Roles of SARS-CoV-2 Fusion Peptides Uncovered by Neutron Scattering. *J Am Chem Soc* **144**, 2968-2979, doi:10.1021/jacs.1c09856 (2022).

50   Bhatt, P. R. *et al.* Structural basis of ribosomal frameshifting during translation of the SARS-CoV-2 RNA genome. *Science* **372**, 1306-1313, doi:10.1126/science.abf3546 (2021).

51   Roman, C., Lewicka, A., Koirala, D., Li, N. S. & Piccirilli, J. A. The SARS-CoV-2 Programmed -1 Ribosomal Frameshifting Element Crystal Structure Solved to 2.09 A Using Chaperone-Assisted RNA Crystallography. *ACS Chem Biol* **16**, 1469-1481, doi:10.1021/acschembio.1c00324 (2021).

52   Harcourt, B. H. *et al.* Identification of severe acute respiratory syndrome coronavirus replicase products and characterization of papain-like protease activity. *J Virol* **78**, 13600-13612, doi:10.1128/JVI.78.24.13600-13612.2004 (2004).

53   MacDonald, E. A. *et al.* Recognition of Divergent Viral Substrates by the SARS-CoV-2 Main Protease. *ACS Infect Dis* **7**, 2591-2595, doi:10.1021/acsinfecdis.1c00237 (2021).

54   Oudshoorn, D. *et al.* Expression and Cleavage of Middle East Respiratory Syndrome Coronavirus nsp3-4 Polyprotein Induce the Formation of Double-Membrane Vesicles That Mimic Those Associated with Coronaviral RNA Replication. *mBio* **8**, doi:10.1128/mBio.01658-17 (2017).

55   Ricciardi, S. *et al.* The role of NSP6 in the biogenesis of the SARS-CoV-2 replication organelle. *Nature* **606**, 761-768, doi:10.1038/s41586-022-04835-6 (2022).

56   Gao, Y. *et al.* Structure of the RNA-dependent RNA polymerase from COVID-19 virus. *Science* **368**, 779-782, doi:10.1126/science.abb7498 (2020).

57   Subissi, L. *et al.* One severe acute respiratory syndrome coronavirus protein complex integrates processive RNA polymerase and exonuclease activities. *Proc Natl Acad Sci U S A* **111**, E3900-3909, doi:10.1073/pnas.1323705111 (2014).

58   Tvarogova, J. *et al.* Identification and Characterization of a Human Coronavirus 229E Nonstructural Protein 8-Associated RNA 3'-Terminal Adenylyltransferase Activity. *J Virol* **93**, doi:10.1128/JVI.00291-19 (2019).

59   Wang, Q. *et al.* Structural Basis for RNA Replication by the SARS-CoV-2 Polymerase. *Cell* **182**, 417-428 e413, doi:10.1016/j.cell.2020.05.034 (2020).

60   Yue, K. *et al.* The stalk domain of SARS-CoV-2 NSP13 is essential for its helicase activity. *Biochem Biophys Res Commun* **601**, 129-136, doi:10.1016/j.bbrc.2022.02.068 (2022).

61   Ivanov, K. A. & Ziebuhr, J. Human coronavirus 229E nonstructural protein 13: characterization of duplex-unwinding, nucleoside triphosphatase, and RNA 5'-triphosphatase activities. *J Virol* **78**, 7833-7838, doi:10.1128/JVI.78.14.7833-7838.2004 (2004).

62   Walker, A. P. *et al.* The SARS-CoV-2 RNA polymerase is a viral RNA capping enzyme. *Nucleic Acids Res* **49**, 13019-13030, doi:10.1093/nar/gkab1160 (2021).

63   Saramago, M. *et al.* New targets for drug design: importance of nsp14/nsp10 complex formation for the 3'-5' exoribonucleolytic activity on SARS-CoV-2. *FEBS J* **288**, 5130-5147, doi:10.1111/febs.15815 (2021).

64   Viswanathan, T. *et al.* Structural Basis of RNA Cap Modification by SARS-CoV-2 Coronavirus. *bioRxiv*, doi:10.1101/2020.04.26.061705 (2020).

65   El-Kamand, S. *et al.* A distinct ssDNA/RNA binding interface in the Nsp9 protein from SARS-CoV-2. *Proteins* **90**, 176-185, doi:10.1002/prot.26205 (2022).

66   Kang, H. *et al.* Biochemical and genetic analyses of murine hepatitis virus Nsp15 endoribonuclease. *J Virol* **81**, 13587-13597, doi:10.1128/JVI.00547-07 (2007).

67   Di, H., McIntyre, A. A. & Brinton, M. A. New insights about the regulation of Nidovirus subgenomic mRNA synthesis. *Virology* **517**, 38-43, doi:10.1016/j.virol.2018.01.026 (2018).

68   Deng, X. *et al.* Coronavirus nonstructural protein 15 mediates evasion of dsRNA sensors and limits apoptosis in macrophages. *Proc Natl Acad Sci U S A* **114**, E4251-E4260, doi:10.1073/pnas.1618310114 (2017).

69   Schubert, K. *et al.* SARS-CoV-2 Nsp1 binds the ribosomal mRNA channel to inhibit translation. *Nat Struct Mol Biol* **27**, 959-966, doi:10.1038/s41594-020-0511-8 (2020).

70   Tidu, A. *et al.* The viral protein NSP1 acts as a ribosome gatekeeper for shutting down host translation and fostering SARS-CoV-2 translation. *RNA* **27**, 253-264, doi:10.1261/rna.078121.120 (2020).

71   Xu, Z. *et al.* SARS-CoV-2 impairs interferon production via NSP2-induced repression of mRNA translation. *Proc Natl Acad Sci U S A* **119**, e2204539119, doi:10.1073/pnas.2204539119 (2022).

72   Miorin, L. *et al.* SARS-CoV-2 Orf6 hijacks Nup98 to block STAT nuclear import and antagonize interferon signaling. *Proc Natl Acad Sci U S A* **117**, 28344-28354, doi:10.1073/pnas.2016650117 (2020).

73   Li, T. *et al.* Molecular Mechanism of SARS-CoVs Orf6 Targeting the Rae1-Nup98 Complex to Compete With mRNA Nuclear Export. *Front Mol Biosci* **8**, 813248, doi:10.3389/fmolb.2021.813248 (2021).

74   Konno, Y. *et al.* SARS-CoV-2 ORF3b Is a Potent Interferon Antagonist Whose Activity Is Increased by a Naturally Occurring Elongation Variant. *Cell Rep* **32**, 108185, doi:10.1016/j.celrep.2020.108185 (2020).

75   Stewart, H. *et al.* The SARS-CoV-2 protein ORF3c is a mitochondrial modulator of innate immunity. *bioRxiv*, 2022.2011.2015.516323, doi:10.1101/2022.11.15.516323 (2022).

76   Zhang, Y. *et al.* The ORF8 protein of SARS-CoV-2 mediates immune evasion through down-regulating MHC-Iota. *Proc Natl Acad Sci U S A* **118**, doi:10.1073/pnas.2024202118 (2021).

77   Scherer, K. M. *et al.* SARS-CoV-2 nucleocapsid protein adheres to replication organelles before viral assembly at the Golgi/ERGIC and lysosome-mediated egress. *Sci Adv* **8**, eabl4895, doi:10.1126/sciadv.abl4895 (2022).

78   Neuman, B. W. *et al.* Supramolecular architecture of severe acute respiratory syndrome coronavirus revealed by electron cryomicroscopy. *J Virol* **80**, 7918-7928, doi:10.1128/JVI.00645-06 (2006).

79   Lu, S. *et al.* The SARS-CoV-2 Nucleocapsid phosphoprotein forms mutually exclusive condensates with RNA and the membrane-associated M protein. *bioRxiv*, doi:10.1101/2020.07.30.228023 (2020).

80   Xu, R., Shi, M., Li, J., Song, P. & Li, N. Construction of SARS-CoV-2 Virus-Like Particles by Mammalian Expression System. *Front Bioeng Biotechnol* **8**, 862, doi:10.3389/fbioe.2020.00862 (2020).

81   Plescia, C. B. *et al.* SARS-CoV-2 viral budding and entry can be modeled using BSL-2 level virus-like particles. *J Biol Chem* **296**, 100103, doi:10.1074/jbc.RA120.016148 (2021).

82   Zhang, Z. *et al.* Structure of SARS-CoV-2 membrane protein essential for virus assembly. *Nat Commun* **13**, 4399, doi:10.1038/s41467-022-32019-3 (2022).

83   Neuman, B. W. *et al.* A structural analysis of M protein in coronavirus assembly and morphology. *J Struct Biol* **174**, 11-22, doi:10.1016/j.jsb.2010.11.021 (2011).

84   Mandala, V. S. *et al.* Structure and drug binding of the SARS-CoV-2 envelope protein transmembrane domain in lipid bilayers. *Nat Struct Mol Biol* **27**, 1202-1208, doi:10.1038/s41594-020-00536-8 (2020).

85   DeDiego, M. L. *et al.* A severe acute respiratory syndrome coronavirus that lacks the E gene is attenuated in vitro and in vivo. *J Virol* **81**, 1701-1713, doi:10.1128/JVI.01467-06 (2007).

86   Castano-Rodriguez, C. *et al.* Role of Severe Acute Respiratory Syndrome Coronavirus Viroporins E, 3a, and 8a in Replication and Pathogenesis. *mBio* **9**, doi:10.1128/mBio.02325-17 (2018).

87   Freundt, E. C. *et al.* The open reading frame 3a protein of severe acute respiratory syndrome-associated coronavirus promotes membrane rearrangement and cell death. *J Virol* **84**, 1097-1109, doi:10.1128/JVI.01662-09 (2010).

88   Yue, Y. *et al.* SARS-Coronavirus Open Reading Frame-3a drives multimodal necrotic cell death. *Cell Death Dis* **9**, 904, doi:10.1038/s41419-018-0917-y (2018).

89   Ke, Z. *et al.* Structures and distributions of SARS-CoV-2 spike proteins on intact virions. *Nature* **588**, 498-502, doi:10.1038/s41586-020-2665-2 (2020).

90   Zhang, L. *et al.* SARS-CoV-2 spike-protein D614G mutation increases virion spike density and infectivity. *Nat Commun* **11**, 6013, doi:10.1038/s41467-020-19808-4 (2020).

91   Timilsina, U., Umthong, S., Ivey, E. B., Waxman, B. & Stavrou, S. SARS-CoV-2 ORF7a potently inhibits the antiviral effect of the host factor SERINC5. *Nat Commun* **13**, 2935, doi:10.1038/s41467-022-30609-9 (2022).

92   Saramago, M. *et al.* The nsp15 Nuclease as a Good Target to Combat SARS-CoV-2: Mechanism of Action and Its Inactivation with FDA-Approved Drugs. *Microorganisms* **10**, doi:10.3390/microorganisms10020342 (2022).

93   Joseph, J. S. *et al.* Crystal structure of a monomeric form of severe acute respiratory syndrome coronavirus endonuclease nsp15 suggests a role for hexamerization as an allosteric switch. *J Virol* **81**, 6700-6708, doi:10.1128/JVI.02817-06 (2007).

94   Zhang, L. *et al.* Structural and Biochemical Characterization of Endoribonuclease Nsp15 Encoded by Middle East Respiratory Syndrome Coronavirus. *J Virol* **92**, doi:10.1128/JVI.00893-18 (2018).

95   Guarino, L. A. *et al.* Mutational analysis of the SARS virus Nsp15 endoribonuclease: identification of residues affecting hexamer formation. *J Mol Biol* **353**, 1106-1117, doi:10.1016/j.jmb.2005.09.007 (2005).

96   Bhardwaj, K. *et al.* Structural and functional analyses of the severe acute respiratory syndrome coronavirus endoribonuclease Nsp15. *J Biol Chem* **283**, 3655-3664, doi:10.1074/jbc.M708375200 (2008).

97   Wilson, I. M., Frazier, M. N., Li, J. L., Randall, T. A. & Stanley, R. E. Biochemical Characterization of Emerging SARS-CoV-2 Nsp15 Endoribonuclease Variants. *bioRxiv*, doi:10.1101/2022.05.10.491349 (2022).

98   Athmer, J. *et al.* In Situ Tagged nsp15 Reveals Interactions with Coronavirus Replication/Transcription Complex-Associated Proteins. *mBio* **8**, doi:10.1128/mBio.02320-16 (2017).

99   Cao, J. & Zhang, X. Comparative in vivo analysis of the nsp15 endoribonuclease of murine, porcine and severe acute respiratory syndrome coronaviruses. *Virus Res* **167**, 247-258, doi:10.1016/j.virusres.2012.05.006 (2012).

100   Bhardwaj, K., Sun, J., Holzenburg, A., Guarino, L. A. & Kao, C. C. RNA recognition and cleavage by the SARS coronavirus endoribonuclease. *J Mol Biol* **361**, 243-256, doi:10.1016/j.jmb.2006.06.021 (2006).

101   Cuchillo, C. M. *et al.* The role of 2',3'-cyclic phosphodiesters in the bovine pancreatic ribonuclease A catalysed cleavage of RNA: intermediates or products? *FEBS Lett* **333**, 207-210, doi:10.1016/0014-5793(93)80654-d (1993).

102   Ivanov, K. A. *et al.* Major genetic marker of nidoviruses encodes a replicative endoribonuclease. *Proc Natl Acad Sci U S A* **101**, 12694-12699, doi:10.1073/pnas.0403127101 (2004).

103   Posthuma, C. C. *et al.* Site-directed mutagenesis of the Nidovirus replicative endoribonuclease NendoU exerts pleiotropic effects on the arterivirus life cycle. *J Virol* **80**, 1653-1661, doi:10.1128/JVI.80.4.1653-1661.2006 (2006).

104   Sun, Y. *et al.* Nonstructural Protein 11 of Porcine Reproductive and Respiratory Syndrome Virus Suppresses Both MAVS and RIG-I Expression as One of the Mechanisms to Antagonize Type I Interferon Production. *PLoS One* **11**, e0168314, doi:10.1371/journal.pone.0168314 (2016).

105   Kindler, E. *et al.* Early endonuclease-mediated evasion of RNA sensing ensures efficient coronavirus replication. *PLoS Pathog* **13**, e1006195, doi:10.1371/journal.ppat.1006195 (2017).

106   Hackbart, M., Deng, X. & Baker, S. C. Coronavirus endoribonuclease targets viral polyuridine sequences to evade activating host sensors. *Proc Natl Acad Sci U S A* **117**, 8094-8103, doi:10.1073/pnas.1921485117 (2020).

107   Nga, P. T. *et al.* Discovery of the first insect nidovirus, a missing evolutionary link in the emergence of the largest RNA virus genomes. *PLoS Pathog* **7**, e1002215, doi:10.1371/journal.ppat.1002215 (2011).

108   Bukhari, K. *et al.* Description and initial characterization of metatranscriptomic nidovirus-like genomes from the proposed new family Abyssoviridae, and from a sister group to the Coronavirinae, the proposed genus Alphaletovirus. *Virology* **524**, 160-171, doi:10.1016/j.virol.2018.08.010 (2018).

109   Saberi, A., Gulyaeva, A. A., Brubacher, J. L., Newmark, P. A. & Gorbalenya, A. E. A planarian nidovirus expands the limits of RNA genome size. *PLoS Pathog* **14**, e1007314, doi:10.1371/journal.ppat.1007314 (2018).

110   Ortiz-Alacantare, J. B., K.; Palaninathan, S.; Frieman, M.; Baric, R.S.; Kao, C.C. Small molecule inhibitors of the SARS-CoV Nsp15 endoribonuclease. *Virus Adaptation and Treatment* **2010:2**, 125-133, doi:https://doi.org/10.2147/VAAT.S12733 (2010).

111   Kim, Y. *et al.* Tipiracil binds to uridine site and inhibits Nsp15 endoribonuclease NendoU from SARS-CoV-2. *Commun Biol* **4**, 193, doi:10.1038/s42003-021-01735-9 (2021).

112   Canal, B. *et al.* Identifying SARS-CoV-2 antiviral compounds by screening for small molecule inhibitors of nsp15 endoribonuclease. *Biochem J* **478**, 2465-2479, doi:10.1042/BCJ20210199 (2021).

113   Choi, R. *et al.* High-throughput screening of the ReFRAME, Pandemic Box, and COVID Box drug repurposing libraries against SARS-CoV-2 nsp15 endoribonuclease to identify small-molecule inhibitors of viral activity. *PLoS One* **16**, e0250019, doi:10.1371/journal.pone.0250019 (2021).

114   Hong, S. *et al.* Epigallocatechin Gallate Inhibits the Uridylate-Specific Endoribonuclease Nsp15 and Efficiently Neutralizes the SARS-CoV-2 Strain. *J Agric Food Chem* **69**, 5948-5954, doi:10.1021/acs.jafc.1c02050 (2021).

115   Stevaert, A. *et al.* Betulonic Acid Derivatives Interfering with Human Coronavirus 229E Replication via the nsp15 Endoribonuclease. *J Med Chem* **64**, 5632-5644, doi:10.1021/acs.jmedchem.0c02124 (2021).

116   Wang, G., Li, X. & Wang, Z. APD3: the antimicrobial peptide database as a tool for research and education. *Nucleic Acids Res* **44**, D1087-1093, doi:10.1093/nar/gkv1278 (2016).

117   Holthausen, D. J. *et al.* An Amphibian Host Defense Peptide Is Virucidal for Human H1 Hemagglutinin-Bearing Influenza Viruses. *Immunity* **46**, 587-595, doi:10.1016/j.immuni.2017.03.018 (2017).

118   Lee, S. H. *et al.* The amphibian peptide Yodha is virucidal for Zika and dengue viruses. *Sci Rep* **11**, 602, doi:10.1038/s41598-020-80596-4 (2021).

119   Gennaro, R., Skerlavaj, B. & Romeo, D. Purification, composition, and activity of two bactenecins, antibacterial peptides of bovine neutrophils. *Infect Immun* **57**, 3142-3146, doi:10.1128/iai.57.10.3142-3146.1989 (1989).

120   Romeo, D., Skerlavaj, B., Bolognesi, M. & Gennaro, R. Structure and bactericidal activity of an antibiotic dodecapeptide purified from bovine neutrophils. *J Biol Chem* **263**, 9573-9575 (1988).

121   Zanetti, M., Gennaro, R. & Romeo, D. Cathelicidins: a novel protein family with a common proregion and a variable C-terminal antimicrobial domain. *FEBS Lett* **374**, 1-5, doi:10.1016/0014-5793(95)01050-o (1995).

122   Basanez, G., Shinnar, A. E. & Zimmerberg, J. Interaction of hagfish cathelicidin antimicrobial peptides with model lipid membranes. *FEBS Lett* **532**, 115-120, doi:10.1016/s0014-5793(02)03651-7 (2002).

123   Zanetti, M. Cathelicidins, multifunctional peptides of the innate immunity. *J Leukoc Biol* **75**, 39-48, doi:10.1189/jlb.0403147 (2004).

124   Sorensen, O. E. *et al.* Human cathelicidin, hCAP-18, is processed to the antimicrobial peptide LL-37 by extracellular cleavage with proteinase 3. *Blood* **97**, 3951-3959, doi:10.1182/blood.v97.12.3951 (2001).

125   Sorensen, O. E. *et al.* Processing of seminal plasma hCAP-18 to ALL-38 by gastricsin: a novel mechanism of generating antimicrobial peptides in vagina. *J Biol Chem* **278**, 28540-28546, doi:10.1074/jbc.M301608200 (2003).

126   Alford, M. A., Baquir, B., Santana, F. L., Haney, E. F. & Hancock, R. E. W. Cathelicidin Host Defense Peptides and Inflammatory Signaling: Striking a Balance. *Front Microbiol* **11**, 1902, doi:10.3389/fmicb.2020.01902 (2020).

127   Scheenstra, M. R. *et al.* Cathelicidins PMAP-36, LL-37 and CATH-2 are similar peptides with different modes of action. *Sci Rep* **9**, 4780, doi:10.1038/s41598-019-41246-6 (2019).

128   Madhongsa, K. *et al.* Antimicrobial action of the cyclic peptide bactenecin on Burkholderia pseudomallei correlates with efficient membrane permeabilization. *PLoS Negl Trop Dis* **7**, e2267, doi:10.1371/journal.pntd.0002267 (2013).

129   Gidalevitz, D. *et al.* Interaction of antimicrobial peptide protegrin with biomembranes. *Proc Natl Acad Sci U S A* **100**, 6302-6307, doi:10.1073/pnas.0934731100 (2003).

130   Boman, H. G., Agerberth, B. & Boman, A. Mechanisms of action on Escherichia coli of cecropin P1 and PR-39, two antibacterial peptides from pig intestine. *Infect Immun* **61**, 2978-2984, doi:10.1128/iai.61.7.2978-2984.1993 (1993).

131   Subbalakshmi, C. & Sitaram, N. Mechanism of antimicrobial action of indolicidin. *FEMS Microbiol Lett* **160**, 91-96, doi:10.1111/j.1574-6968.1998.tb12896.x (1998).

132   Soundrarajan, N. *et al.* Protegrin-1 cytotoxicity towards mammalian cells positively correlates with the magnitude of conformational changes of the unfolded form upon cell interaction. *Sci Rep* **9**, 11569, doi:10.1038/s41598-019-47955-2 (2019).

133   Steinstraesser, L. *et al.* Protegrin-1 enhances bacterial killing in thermally injured skin. *Crit Care Med* **29**, 1431-1437, doi:10.1097/00003246-200107000-00022 (2001).

134   Schaller-Bals, S., Schulze, A. & Bals, R. Increased levels of antimicrobial peptides in tracheal aspirates of newborn infants during infection. *Am J Respir Crit Care Med* **165**, 992-995, doi:10.1164/ajrccm.165.7.200110-020 (2002).

135   Lysenko, E. S., Gould, J., Bals, R., Wilson, J. M. & Weiser, J. N. Bacterial phosphorylcholine decreases susceptibility to the antimicrobial peptide LL-37/hCAP18 expressed in the upper respiratory tract. *Infect Immun* **68**, 1664-1671, doi:10.1128/IAI.68.3.1664-1671.2000 (2000).

136   Bowdish, D. M. *et al.* Impact of LL-37 on anti-infective immunity. *J Leukoc Biol* **77**, 451-459, doi:10.1189/jlb.0704380 (2005).

137   Cao, X. *et al.* Cathelicidin-OA1, a novel antioxidant peptide identified from an amphibian, accelerates skin wound healing. *Sci Rep* **8**, 943, doi:10.1038/s41598-018-19486-9 (2018).

138   Verjans, E. T., Zels, S., Luyten, W., Landuyt, B. & Schoofs, L. Molecular mechanisms of LL-37-induced receptor activation: An overview. *Peptides* **85**, 16-26, doi:10.1016/j.peptides.2016.09.002 (2016).

139   Cai, S. *et al.* Python Cathelicidin CATHPb1 Protects against Multidrug-Resistant Staphylococcal Infections by Antimicrobial-Immunomodulatory Duality. *J Med Chem* **61**, 2075-2086, doi:10.1021/acs.jmedchem.8b00036 (2018).

140   Saud, Z. *et al.* The SARS-CoV2 envelope differs from host cells, exposes procoagulant lipids, and is disrupted in vivo by oral rinses. *J Lipid Res* **63**, 100208, doi:10.1016/j.jlr.2022.100208 (2022).

141   Currie, S. M. *et al.* Cathelicidins Have Direct Antiviral Activity against Respiratory Syncytial Virus In Vitro and Protective Function In Vivo in Mice and Humans. *J Immunol* **196**, 2699-2710, doi:10.4049/jimmunol.1502478 (2016).

142   Currie, S. M. *et al.* The human cathelicidin LL-37 has antiviral activity against respiratory syncytial virus. *PLoS One* **8**, e73659, doi:10.1371/journal.pone.0073659 (2013).

143   Tripathi, S. *et al.* The human cathelicidin LL-37 inhibits influenza A viruses through a mechanism distinct from that of surfactant protein D or defensins. *J Gen Virol* **94**, 40-49, doi:10.1099/vir.0.045013-0 (2013).

144   Barlow, P. G. *et al.* Antiviral activity and increased host defense against influenza infection elicited by the human cathelicidin LL-37. *PLoS One* **6**, e25333, doi:10.1371/journal.pone.0025333 (2011).

145   Chen, R. E. *et al.* Resistance of SARS-CoV-2 variants to neutralization by monoclonal and serum-derived polyclonal antibodies. *Nat Med* **27**, 717-726, doi:10.1038/s41591-021-01294-w (2021).

146   Steiner, H., Hultmark, D., Engstrom, A., Bennich, H. & Boman, H. G. Sequence and specificity of two antibacterial proteins involved in insect immunity. *Nature* **292**, 246-248 (1981).

147   Fleming, A. On a Remarkable Bacteriolytic Element Found in Tissues and Secretions. *Proceedings of the Royal Society of London Series B* **93**, 306, doi:10.1098/rspb.1922.0023 (1922).

148   Habermann, E. Bee and wasp venoms. *Science* **177**, 314-322 (1972).

149   Ganz, T. *et al.* Defensins. Natural peptide antibiotics of human neutrophils. *J Clin Invest* **76**, 1427-1435, doi:10.1172/JCI112120 (1985).

150   Giovannini, M. G., Poulter, L., Gibson, B. W. & Williams, D. H. Biosynthesis and degradation of peptides derived from Xenopus laevis prohormones. *Biochem J* **243**, 113-120 (1987).

151   Zasloff, M. Magainins, a class of antimicrobial peptides from Xenopus skin: isolation, characterization of two active forms, and partial cDNA sequence of a precursor. *Proc Natl Acad Sci U S A* **84**, 5449-5453 (1987).

152   Zanetti, M., Del Sal, G., Storici, P., Schneider, C. & Romeo, D. The cDNA of the neutrophil antibiotic Bac5 predicts a pro-sequence homologous to a cysteine proteinase inhibitor that is common to other neutrophil antibiotics. *J Biol Chem* **268**, 522-526 (1993).

153   Xiao, Y. *et al.* Identification and functional characterization of three chicken cathelicidins with potent antimicrobial activity. *J Biol Chem* **281**, 2858-2867, doi:10.1074/jbc.M507180200 (2006).

154   Uzzell, T., Stolzenberg, E. D., Shinnar, A. E. & Zasloff, M. Hagfish intestinal antimicrobial peptides are ancient cathelicidins. *Peptides* **24**, 1655-1667, doi:10.1016/j.peptides.2003.08.024 (2003).

155   Zanetti, M. The role of cathelicidins in the innate host defenses of mammals. *Curr Issues Mol Biol* **7**, 179-196 (2005).

156   Verheije, M. H., Coorens, M., Weerts, E. A. W. S., Berends, A. J., van Harten, R. M., Angel, M., Kooij, J., Ordonez, S. R., van Beurden, S. J., van Dijk, A., Haagsman, H. P., Veldhuizen, E. J. A. Antiviral activity of selected cathelicidins against infectious bronchitis virus. *PeptideScience* **114**, doi:https://doi.org/10.1002/pep2.24234 (2022).

157   Sousa, F. H. *et al.* Cathelicidins display conserved direct antiviral activity towards rhinovirus. *Peptides* **95**, 76-83, doi:10.1016/j.peptides.2017.07.013 (2017).

158   Mookherjee, N. *et al.* Modulation of the TLR-mediated inflammatory response by the endogenous human host defense peptide LL-37. *J Immunol* **176**, 2455-2464, doi:10.4049/jimmunol.176.4.2455 (2006).

159   Scott, M. G., Davidson, D. J., Gold, M. R., Bowdish, D. & Hancock, R. E. The human antimicrobial peptide LL-37 is a multifunctional modulator of innate immune responses. *J Immunol* **169**, 3883-3891, doi:10.4049/jimmunol.169.7.3883 (2002).

160   Mookherjee, N. *et al.* Systems biology evaluation of immune responses induced by human host defence peptide LL-37 in mononuclear cells. *Mol Biosyst* **5**, 483-496, doi:10.1039/b813787k (2009).

161   De, Y. *et al.* LL-37, the neutrophil granule- and epithelial cell-derived cathelicidin, utilizes formyl peptide receptor-like 1 (FPRL1) as a receptor to chemoattract human peripheral blood neutrophils, monocytes, and T cells. *J Exp Med* **192**, 1069-1074, doi:10.1084/jem.192.7.1069 (2000).

162   Huang, H. J., Ross, C. R. & Blecha, F. Chemoattractant properties of PR-39, a neutrophil antibacterial peptide. *J Leukoc Biol* **61**, 624-629, doi:10.1002/jlb.61.5.624 (1997).

163   Yang, J. *et al.* The I-TASSER Suite: protein structure and function prediction. *Nat Methods* **12**, 7-8, doi:10.1038/nmeth.3213 (2015).

164   Edara, V. V., Hudson, W. H., Xie, X., Ahmed, R. & Suthar, M. S. Neutralizing Antibodies Against SARS-CoV-2 Variants After Infection and Vaccination. *JAMA* **325**, 1896-1898, doi:10.1001/jama.2021.4388 (2021).

165   Edara, V. V. *et al.* Infection- and vaccine-induced antibody binding and neutralization of the B.1.351 SARS-CoV-2 variant. *Cell Host Microbe* **29**, 516-521 e513, doi:10.1016/j.chom.2021.03.009 (2021).

166   Edara, V. V. *et al.* Infection and Vaccine-Induced Neutralizing-Antibody Responses to the SARS-CoV-2 B.1.617 Variants. *N Engl J Med* **385**, 664-666, doi:10.1056/NEJMc2107799 (2021).

167   Krivov, G. G., Shapovalov, M. V. & Jr., R. D. Improved prediction of protein side-chain conformations with SCWRL4. *proteins* **77**, 778-795 (2009).

168   Humphrey, W., Dalke, A. & Schulten, K. VMD: visual molecular dynamics. *Journal of Molecular Graphics* **14**, 33-38 (1996).

169   Phillips, J. C. *et al.* Scalable molecular dynamics with NAMD. *Journal of computational chemistry* **26**, 1781-1802, doi:10.1002/jcc.20289 (2005).

170   Vanommeslaeghe, K. *et al.* CHARMM general force field: A force field for drug-like molecules compatible with the CHARMM all-atom additive biological force fields. *Journal of computational chemistry* **31**, 671-690, doi:https://doi.org/10.1002/jcc.21367 (2010).

171   Darden, T., York, D. & Pedersen, L. Particle mesh Ewald: An N·log(N) method for Ewald sums in large systems. *The Journal of Chemical Physics* **98**, 10089-10092, doi:10.1063/1.464397 (1993).

172   Altschul, S. F., Gish, W., Miller, W., Myers, E. W. & Lipman, D. J. Basic local alignment search tool. *J Mol Biol* **215**, 403-410, doi:10.1016/S0022-2836(05)80360-2 (1990).

173   Harvey, W. T. *et al.* SARS-CoV-2 variants, spike mutations and immune escape. *Nat Rev Microbiol* **19**, 409-424, doi:10.1038/s41579-021-00573-0 (2021).

174   CDC. *SARS-CoV-2 Variant Classifications and Definitions*, <https://www.cdc.gov/coronavirus/2019-ncov/variants/variant-info.html#print> (2021).

175   Berman, H. M. *et al.* The Protein Data Bank. *Nucleic Acids Research* **28**, 235-242 (2000).

176   Altschul, S. F. *et al.* Gapped BLAST and PSI-BLAST: a new generation of protein database search programs. *Nucleic Acids Research* **25**, 3389-3402 (1997).

177   Steinegger, M. *et al.* HH-suite3 for fast remote homology detection and deep protein annotation. *BMC bioinformatics* **20**, 473, doi:10.1186/s12859-019-3019-7 (2019).

178   Gao, M. & Skolnick, J. A novel sequence alignment algorithm based on deep learning of the protein folding code. *Bioinformatics* **37**, 490-496, doi:10.1093/bioinformatics/btaa810 (2020).

179   Gao, M. & Skolnick, J. A General Framework to Learn Tertiary Structure for Protein Sequence Characterization. *Frontiers in Bioinformatics* **1**, doi:10.3389/fbinf.2021.689960 (2021).

180   Deng, Y., Liu, J., Zheng, Q., Yong, W. & Lu, M. Structures and polymorphic interactions of two heptad-repeat regions of the SARS virus S2 protein. *Structure* **14**, 889-899, doi:10.1016/j.str.2006.03.007 (2006).

181   Xia, S. *et al.* Inhibition of SARS-CoV-2 (previously 2019-nCoV) infection by a highly potent pan-coronavirus fusion inhibitor targeting its spike protein that harbors a high capacity to mediate membrane fusion. *Cell Res* **30**, 343-355, doi:10.1038/s41422-020-0305-x (2020).

182   Bosch, B. J. *et al.* Severe acute respiratory syndrome coronavirus (SARS-CoV) infection inhibition using spike protein heptad repeat-derived peptides. *Proceedings of the National Academy of Sciences of the United States of America* **101**, 8455-8460, doi:10.1073/pnas.0400576101 (2004).

183   Liu, S. *et al.* Interaction between heptad repeat 1 and 2 regions in spike protein of SARS-associated coronavirus: implications for virus fusogenic mechanism and identification of fusion inhibitors. *The Lancet* **363**, 938-947, doi:https://doi.org/10.1016/S0140-6736(04)15788-7 (2004).

184   Meekins, D. A. *et al.* Susceptibility of swine cells and domestic pigs to SARS-CoV-2. *Emerg Microbes Infect* **9**, 2278-2288, doi:10.1080/22221751.2020.1831405 (2020).

185   Outlaw, V. K. *et al.* Inhibition of Coronavirus Entry In Vitro and Ex Vivo by a Lipid-Conjugated Peptide Derived from the SARS-CoV-2 Spike Glycoprotein HRC Domain. *mBio* **11**, doi:10.1128/mBio.01935-20 (2020).

186   Zhu, Y., Yu, D., Yan, H., Chong, H. & He, Y. Design of Potent Membrane Fusion Inhibitors against SARS-CoV-2, an Emerging Coronavirus with High Fusogenic Activity. *J Virol* **94**, doi:10.1128/JVI.00635-20 (2020).

187   Zheng, M. *et al.* Stapled Peptides Targeting SARS-CoV-2 Spike Protein HR1 Inhibit the Fusion of Virus to Its Cell Receptor. *J Med Chem* **64**, 17486-17495, doi:10.1021/acs.jmedchem.1c01681 (2021).

188   Yang, K. *et al.* Nanomolar inhibition of SARS-CoV-2 infection by an unmodified peptide targeting the prehairpin intermediate of the spike protein. *Proc Natl Acad Sci U S A* **119**, e2210990119, doi:10.1073/pnas.2210990119 (2022).

189   Scocchi, M. *et al.* Structural aspects and biological properties of the cathelicidin PMAP-36. *FEBS J* **272**, 4398-4406, doi:10.1111/j.1742-4658.2005.04852.x (2005).

190   Volgers, C., Savelkoul, P. H. M. & Stassen, F. R. M. Gram-negative bacterial membrane vesicle release in response to the host-environment: different threats, same trick? *Crit Rev Microbiol* **44**, 258-273, doi:10.1080/1040841X.2017.1353949 (2018).

191   Henzler Wildman, K. A., Lee, D. K. & Ramamoorthy, A. Mechanism of lipid bilayer disruption by the human antimicrobial peptide, LL-37. *Biochemistry* **42**, 6545-6558, doi:10.1021/bi0273563 (2003).

192   Varadi, M. *et al.* AlphaFold Protein Structure Database: massively expanding the structural coverage of protein-sequence space with high-accuracy models. *Nucleic Acids Res* **50**, D439-D444, doi:10.1093/nar/gkab1061 (2022).

193   The PyMOL Molecular Graphics System v. Version 2.0 (Schrödinger, LLC.).

194   Yu, G. Using ggtree to Visualize Data on Tree-Like Structures. *Curr Protoc Bioinformatics* **69**, e96, doi:10.1002/cpbi.96 (2020).

195   Edgar, R. C. MUSCLE: a multiple sequence alignment method with reduced time and space complexity. *BMC Bioinformatics* **5**, 113, doi:10.1186/1471-2105-5-113 (2004).

196   Antinori, A. & Bausch-Jurken, M. The Burden of COVID-19 in the Immunocompromised Patient: Implications for Vaccination and Needs for the Future. *J Infect Dis* **228**, S4-S12, doi:10.1093/infdis/jiad181 (2023).

197   Mari, A. *et al.* Global Genomic Analysis of SARS-CoV-2 RNA Dependent RNA Polymerase Evolution and Antiviral Drug Resistance. *Microorganisms* **9**, doi:10.3390/microorganisms9051094 (2021).

198   Martinot, M. *et al.* Remdesivir failure with SARS-CoV-2 RNA-dependent RNA-polymerase mutation in a B-cell immunodeficient patient with protracted Covid-19. *Clin Infect Dis*, doi:10.1093/cid/ciaa1474 (2020).

199   Frazier, M. N. *et al.* Characterization of SARS2 Nsp15 nuclease activity reveals it's mad about U. *Nucleic Acids Res* **49**, 10136-10149, doi:10.1093/nar/gkab719 (2021).

200   Gao, B. *et al.* Inhibition of anti-viral stress granule formation by coronavirus endoribonuclease nsp15 ensures efficient virus replication. *PLoS Pathog* **17**, e1008690, doi:10.1371/journal.ppat.1008690 (2021).

201   Ulferts, R. & Ziebuhr, J. Nidovirus ribonucleases: Structures and functions in viral replication. *RNA Biol* **8**, 295-304, doi:10.4161/rna.8.2.15196 (2011).

202   Deng, X. *et al.* Coronavirus Endoribonuclease Activity in Porcine Epidemic Diarrhea Virus Suppresses Type I and Type III Interferon Responses. *J Virol* **93**, doi:10.1128/JVI.02000-18 (2019).

203   Ng, Y. L., Salim, C. K. & Chu, J. J. H. Drug repurposing for COVID-19: Approaches, challenges and promising candidates. *Pharmacol Ther* **228**, 107930, doi:10.1016/j.pharmthera.2021.107930 (2021).

204   Eberhardt, J., Santos-Martins, D., Tillack, A. F. & Forli, S. AutoDock Vina 1.2.0: New Docking Methods, Expanded Force Field, and Python Bindings. *J Chem Inf Model* **61**, 3891-3898, doi:10.1021/acs.jcim.1c00203 (2021).

205   Guedes, I. A. *et al.* New machine learning and physics-based scoring functions for drug discovery. *Sci Rep* **11**, 3198, doi:10.1038/s41598-021-82410-1 (2021).

206   Jones, G., Willett, P., Glen, R. C., Leach, A. R. & Taylor, R. Development and validation of a genetic algorithm for flexible docking. *J Mol Biol* **267**, 727-748, doi:10.1006/jmbi.1996.0897 (1997).

207   Zhou, H., Cao, H. & Skolnick, J. FRAGSITE: A Fragment-Based Approach for Virtual Ligand Screening. *J Chem Inf Model* **61**, 2074-2089, doi:10.1021/acs.jcim.0c01160 (2021).

208   Zhou, H. & Skolnick, J. Template-based protein structure modeling using TASSER(VMT.). *Proteins* **80**, 352-361, doi:10.1002/prot.23183 (2012).

209   Bernstein, F. C. *et al.* The Protein Data Bank: a computer-based archival file for macromolecular structures. *J Mol Biol* **112**, 535-542, doi:10.1016/s0022-2836(77)80200-3 (1977).

210   Mysinger, M. M., Carchia, M., Irwin, J. J. & Shoichet, B. K. Directory of useful decoys, enhanced (DUD-E): better ligands and decoys for better benchmarking. *J Med Chem* **55**, 6582-6594, doi:10.1021/jm300687e (2012).

211   Wishart, D. S. *et al.* DrugBank: a comprehensive resource for in silico drug discovery and exploration. *Nucleic Acids Res* **34**, D668-672, doi:10.1093/nar/gkj067 (2006).

212   Corbett, K. S. *et al.* mRNA-1273 protects against SARS-CoV-2 beta infection in nonhuman primates. *Nat Immunol* **22**, 1306-1315, doi:10.1038/s41590-021-01021-0 (2021).

213   Vanderheiden, A. *et al.* CCR2 Signaling Restricts SARS-CoV-2 Infection. *mBio* **12**, e0274921, doi:10.1128/mBio.02749-21 (2021).

214   Sixto-Lopez, Y. & Martinez-Archundia, M. Drug repositioning to target NSP15 protein on SARS-CoV-2 as possible COVID-19 treatment. *J Comput Chem* **42**, 897-907, doi:10.1002/jcc.26512 (2021).

215   Chandra, A., Gurjar, V., Qamar, I. & Singh, N. Identification of potential inhibitors of SARS-COV-2 endoribonuclease (EndoU) from FDA approved drugs: a drug repurposing approach to find therapeutics for COVID-19. *J Biomol Struct Dyn* **39**, 4201-4211, doi:10.1080/07391102.2020.1775127 (2021).

216   Wang, X. *et al.* Combination of antiviral drugs inhibits SARS-CoV-2 polymerase and exonuclease and demonstrates COVID-19 therapeutic potential in viral cell culture. *Commun Biol* **5**, 154, doi:10.1038/s42003-022-03101-9 (2022).

217   Ahmed, M. S. *et al.* FDA approved drugs with antiviral activity against SARS-CoV-2: From structure-based repurposing to host-specific mechanisms. *Biomed Pharmacother* **162**, 114614, doi:10.1016/j.biopha.2023.114614 (2023).

218   Carter-Timofte, M. E. *et al.* Antiviral Potential of the Antimicrobial Drug Atovaquone against SARS-CoV-2 and Emerging Variants of Concern. *ACS Infect Dis* **7**, 3034-3051, doi:10.1021/acsinfecdis.1c00278 (2021).

219   Bakshi, R. P. *et al.* Long-acting injectable atovaquone nanomedicines for malaria prophylaxis. *Nat Commun* **9**, 315, doi:10.1038/s41467-017-02603-z (2018).

220   Osawa, M. *et al.* Efficacy of glecaprevir and pibrentasvir treatment for genotype 1b hepatitis C virus drug resistance-associated variants in humanized mice. *J Gen Virol* **100**, 1123-1131, doi:10.1099/jgv.0.001268 (2019).

221   Ma, C. D. *et al.* Fluoxazolevir inhibits hepatitis C virus infection in humanized chimeric mice by blocking viral membrane fusion. *Nat Microbiol* **5**, 1532-1541, doi:10.1038/s41564-020-0781-2 (2020).

222   Zhou, H., Cao, H. & Skolnick, J. FINDSITE(comb2.0): A New Approach for Virtual Ligand Screening of Proteins and Virtual Target Screening of Biomolecules. *J Chem Inf Model* **58**, 2343-2354, doi:10.1021/acs.jcim.8b00309 (2018).

223   Gaulton, A. *et al.* ChEMBL: a large-scale bioactivity database for drug discovery. *Nucleic Acids Res* **40**, D1100-1107, doi:10.1093/nar/gkr777 (2012).

224   Nixon, G. L. *et al.* Antimalarial pharmacology and therapeutics of atovaquone. *J Antimicrob Chemother* **68**, 977-985, doi:10.1093/jac/dks504 (2013).

225   Jain, M. K. *et al.* Atovaquone for treatment of COVID-19: A prospective randomized, double-blind, placebo-controlled clinical trial. *Front Pharmacol* **13**, 1020123, doi:10.3389/fphar.2022.1020123 (2022).

226   Erasmus, J. H. *et al.* A Nanostructured Lipid Carrier for Delivery of a Replicating Viral RNA Provides Single, Low-Dose Protection against Zika. *Mol Ther* **26**, 2507-2522, doi:10.1016/j.ymthe.2018.07.010 (2018).

227   Brown, A. J. *et al.* Broad spectrum antiviral remdesivir inhibits human endemic and zoonotic deltacoronaviruses with a highly divergent RNA dependent RNA polymerase. *Antiviral Res* **169**, 104541, doi:10.1016/j.antiviral.2019.104541 (2019).

228   Sheahan, T. P. *et al.* Broad-spectrum antiviral GS-5734 inhibits both epidemic and zoonotic coronaviruses. *Sci Transl Med* **9**, doi:10.1126/scitranslmed.aal3653 (2017).

229   Agostini, M. L. *et al.* Coronavirus Susceptibility to the Antiviral Remdesivir (GS-5734) Is Mediated by the Viral Polymerase and the Proofreading Exoribonuclease. *mBio* **9**, doi:10.1128/mBio.00221-18 (2018).

230   Toots, M. *et al.* Quantitative efficacy paradigms of the influenza clinical drug candidate EIDD-2801 in the ferret model. *Transl Res* **218**, 16-28, doi:10.1016/j.trsl.2019.12.002 (2020).

231   Sheahan, T. P. *et al.* An orally bioavailable broad-spectrum antiviral inhibits SARS-CoV-2 in human airway epithelial cell cultures and multiple coronaviruses in mice. *Sci Transl Med* **12**, doi:10.1126/scitranslmed.abb5883 (2020).

232   Hoffman, R. L. *et al.* Discovery of Ketone-Based Covalent Inhibitors of Coronavirus 3CL Proteases for the Potential Therapeutic Treatment of COVID-19. *J Med Chem* **63**, 12725-12747, doi:10.1021/acs.jmedchem.0c01063 (2020).

233   Li, Z. T. *et al.* Why Are CD8 T Cell Epitopes of Human Influenza A Virus Conserved? *J Virol* **93**, doi:10.1128/JVI.01534-18 (2019).

234   Moghadasi, S. A. *et al.* Transmissible SARS-CoV-2 variants with resistance to clinical protease inhibitors. *bioRxiv*, doi:10.1101/2022.08.07.503099 (2022).

235   Focosi, D., Maggi, F., McConnell, S. & Casadevall, A. Very low levels of remdesivir resistance in SARS-COV-2 genomes after 18 months of massive usage during the COVID19 pandemic: A GISAID exploratory analysis. *Antiviral Res* **198**, 105247, doi:10.1016/j.antiviral.2022.105247 (2022).